Resonance Suppression of High Q Particle Accelerometer

by

Zayed Ahmed

B.Sc., Islamic University of Technology, 2015

Thesis Submitted in Partial Fulfillment of the
Requirements for the Degree of
Master of Applied Science

in the
School of Mechatronic Systems Engineering
Faculty of Applied Sciences

SIMON FRASER UNIVERSITY
Spring 2022

Declaration of Committee

Name:	**Zayed Ahmed**
Degree:	**Master of Applied Science**
Thesis title:	**Resonance Suppression of High Q Particle Accelerometer**
Committee:	**Chair:** Krishna Vijayaraghavan Associate Professor, Mechatronic Systems Engineering
	Behraad Bahreyni Supervisor Associate Professor, Mechatronic Systems Engineering
	Mehrdad Moallem Committee Member Professor, Mechatronic Systems Engineering
	Mohammad Narimani Examiner Lecturer, Mechatronic Systems Engineering

Abstract

The noise floor of high-performance accelerometers is conditioned by the vacuum pressure inside the sensor package. However, less than atmospheric pressure introduces a lower level of damping to the sensor's mechanical structure, resulting in a large static displacement at resonance. Consequently, this thesis aims to develop a closed-loop system to suppress the displacement of an underdamped accelerometer developed at Intelligent Sensing Laboratory (ISL) and prevent mechanical and electrical failure. This research proposed two controllers, negative derivative feedback (NDF) and positive position feedback (PPF), which offer high gain exclusively at resonance frequency to establish a closed-loop system. Then, controllers are implemented and tested at various vacuum levels to validate their effectiveness. When NDF was employed in the closed-loop, static displacement of the proof mass was reduced by 85 percent, compared to the highest 63 percent reduction when PPF was used. Another issue addressed in this work is the actuator effort. The ISL accelerometer has a substantial mass, which sets it apart from other accelerometers on the market in terms of performance metrics. However, controlling a high inertia-based system would necessitate higher energy. A novel system architecture based on electrode function switching is also presented to address this issue.

Keywords: High-performance accelerometer, Closed-loop control, Vibration control, Resonance suppression

Dedication

To my mom, Dad and to the Scientific Community

Acknowledgments

I would like to acknowledge and express my sincere gratitude to my senior supervisor Dr. Behraad Behreyni, who made this work possible. His advice, expertise and support carried me through all the stages of my research journey. I also would like to thank my supervisor, Dr. Mehrdad Moallem for his guidance on the controller selection.

I would like to thank each and every member of the IMUT family for creating a hospitable environment. Among them, I would specially thank Abbin, Vincent, Asish, Charles, Vahideh, Misha, Erfan, Emmad for their friendship and unconditional support.

I would like to express my heartfelt gratitude to my project partner Charles Duru for his invaluable assistance in designing circuits and assisting me in establishing the test setup. I would also like to commend Vahideh, Behnam and Araf for taking the time to correct my documents as well as for their moral support in making my journey easier. Lastly, I want to mention my friend Saeed for helping in many technical aspects and better understanding of controller design.

And finally, I would like to thank my parents, Shakil and Naghma Ahmed, as well as my brothers, Zubair and Sian, and finally my wife, Rohena Sharmin, for their unending love and support throughout my life.

Table of Contents

List of Tables

List of Figures

List of Acronyms

ADC	Analog to Digital Converter
DAC	Digital to Analog Converter
EMSDM	Electro-mechanical Sigma Delta Modulator
ENEA	Electrical Noise Equivalent Acceleration
ISL	Intelligent Sensing Laboratory
MEMS	Micro Electromechanical Sensor
MNEA	Mechanical Noise Equivalent Acceleration
NDF	Negative Derivative Feedback
PID	Proportional Integral Derivative
PPF	Positive Position Feedback
Q	Quality Factor
QNEA	Quantization Noise Equivalent Acceleration
TNEA	Total Noise Equivalent Acceleration

Glossary

Proof Mass	It is a lumped mass of a MEMS sensor
Quality factor	It represents the amount of damping level in the sensor
Interdigitated fingers	It is a set of capacitive electrodes that are grouped together
Bandwidth	It is the frequency range in which the sensor operates.
Sensitivity or Scale Factor	It correlates the changes in the output voltage to the input applied acceleration
Resolution	It is the minimal detectable acceleration by the sensor
Dynamic Range	The ratio of the accelerometer range to its white noise level

Chapter 1.
Introduction

The advancement of microfabrication technology sparked the development of Micro electromechanical systems (MEMS) over the last two decades across a variety of industries, including automotive, aerospace, medical, consumer electronics, and space exploration. The rise of various applications drives the market to expand exponentially [1]. After pressure sensors, accelerometers are the most common sensors among existing MEMS devices in terms of application diversity and market volume.

High-resolution accelerometers were first used in space exploration in the early 1960s [2]. Later on, Capteur Acceleroemterique Triaxial Ultra Sensible (CACTUS), an electrostatic accelerometer with a resolution of $10^{-9}\, m/s^2$, was designed for satellite research in 1970 [3]. All of these early devices were macroscopic in size, heavy, and expensive. With the advent of the micromachined technology, Rylance and Angela [4] worked on micromachined piezoresistive MEMS accelerometers in 1979 and achieved an mg resolution with a bandwidth greater than 1kHz. MEMS accelerometers demand soared dramatically after it reserved a spot in the automotive industry for airbag deployment [5]. Furthermore, smart phones have recently opened up a sizeable market for MEMS accelerometers, as the majority of phones now include them. Apart from the growing demand and usage of accelerometers in various fields, applications involving weak signal detection, such as gravitational wave, seismic activity detection, etc., require high-performance accelerometers in terms of sensitivity, bandwidth, dynamic range, and noise floor.

1.1. An Overview of MEMS Accelerometers

MEMS accelerometers sense acceleration by converting mechanical energy to electrical energy. Several transduction mechanisms have been reported in the literature, with the most common techniques being capacitive, piezoelectric,

piezoresistive, resonant, thermal, optical, and magnetic [6], [7]. Each transduction mechanism has advantages and disadvantages. Depending on the type of application, a specific transduction mechanism is employed in the system. Among different sensing element types, capacitive transduction is one of the popular mechanisms for its linearity in output, high degree of robustness, good sensitivity, better DC response, low noise performance, low power dissipation, simple design, and fabrication [5]. Based on capacitance formation and sensing direction, capacitive-sensing-element-type accelerometers can be further classified as vertical and lateral devices. A lateral device detects acceleration in the x or y direction parallel to the substrate by incorporating topologies such as interdigitated finger structures to increase the sensitivity [8]. In contrast, a vertical device captures z-direction acceleration by utilizing the out-of-plane motion of the proof mass, which creates variable capacitance by varying its airgap. [5].

Capacitive-based accelerometers are fabricated using bulk or surface micromachining processes. Compared to surface micromachined devices, bulk micromachined devices offer large proof mass, resulting in high sensitivity and low mechanical noise floor [9]. On the other hand, the surface micromachining fabrication process is simpler, less expensive, and offers good compatibility for monolithic integration with interface circuitry[10].

In terms of operation, a capacitive accelerometer can operate in either open-loop or closed-loop configurations, in addition to a variety of transduction topologies. Open-loop accelerometer generates output in proportion to external acceleration applied. While in closed-loop operation, the proof mass displacement is restricted to its nominal position and acceleration is measured through the actuator [11], [12]. A closed-loop system is employed to compensate for the fabrication imperfection, nonlinearities generated in capacitive sensing elements and to improve the sensor parameters such as bandwidth, sensitivity, dynamic range, noise floor, etc. Thus, a closed loop often yields high-performance accelerometers. Although some researchers in the literature and industry have successfully developed open-loop high-performance accelerometers [4], most of the time, it suffers from poor sensor performance metrics

compared to their closed-loop counterparts. Furthermore, closed-loop systems suffer from system instability and implementation complexity as contrasted to open-loop systems. However, it is clear from the preceding discussion that an accelerometer can be configured in various ways to meet specified performance criteria.

1.2. Motivation and Background

Sonobuoys are sonar systems used for submarine detection or underwater acoustic research [13]. As shown in Figure 1.1, it is a cylindrical tube outfitted with hydrophones that are deployed under water to detect nearby signals. Since hydrophones are omnidirectional sensors, estimating the signal direction requires using an array of sensors. Thus, the system becomes bulky and heavy. For that reason, hydrophone arrays are now being replaced with particle acceleration sensors because of their directional sensing nature and small size [14]. Particle acceleration sensors are ultra-high-performance accelerometers. By deploying a MEMS-based accelerometer, the complexity of implementing a long-towed array of hydrophones is eliminated, and the overall size of the hydrophone-based sonar system is reduced. However, the detection of sonar waves puts some stringent requirements on the accelerometer's performance parameters. For operating underwater conditions in presence of strong signals, the sensor noise floor requires to be in the $ng/\sqrt{(Hz)}$ range. To capture weak echoes, the dynamic range of the sensor should be more than 130dB. Moreover, the accelerometer needs to cover a wide frequency range, typically between 50Hz and 1 kHz, for detecting any underwater movement of turbo machinery or objects. Combination of these requirements poses many new design challenges for accelerometers used in sonar applications. A few accelerometers on the market can meet some but not all requirements. The noise floor is one of the most difficult challenges in meeting its performance criteria. All the MEMS devices are susceptible to Brownian noise besides electronic noise. Usually, the electronic noise is about an order of magnitude less than the Brownian noise floor[15]. To gain control over the Brownian noise floor, researchers started designing high-mass systems that reduce mechanical noise while increasing sensitivity [4]. However, fabrication

technology restricts the device's size because the technology limits the minimum feature size.

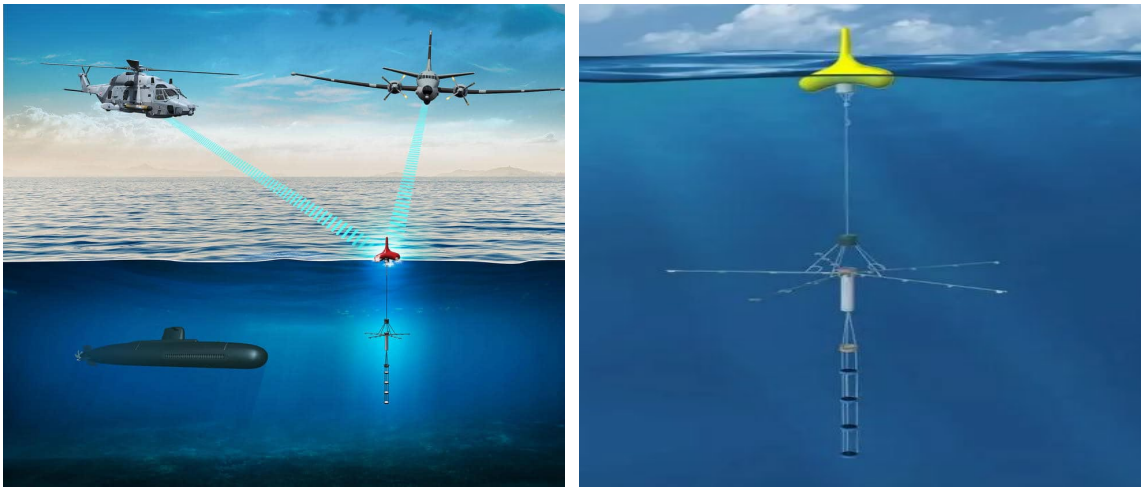

(a) (b)

Figure 1.1 (a) Sonobuoys deployment and (b) sonobuoys (enlarged view)

Another method for a MEMS accelerometer to compensate for mass constraints is to operate under vacuum conditions. Air damping is considered to be the main cause of mechanical noise. Although placing the sensor in the vacuum reduces noise floor, it also increases ringing in open-loop conditions. Another significant issue would be the displacement of the proof-mass at resonance. Less air damping would result in massive displacement of the proof mass, eventually causing the device to fail. Thus, a closed-loop control mechanism can save the device by compensating for its displacement.

In this work, techniques for suppressing the large displacement of the sensor's proof mass have been investigated, developed, and implemented to achieve ultra-high-performance accelerometers.

1.3. Research Objective

High-Performance accelerometers' performance depends on its design, fabrication, transduction method, sensing circuitry, and type of the chosen operation (open loop or closed loop) topology. This work is based on an existing high-

performance MEMS capacitive-based accelerometer that operates in open loop, developed at Simon Fraser University [14]. Any design modification or fabrication of the device is not the subject of this research. Here the focus is on developing a suitable way of controlling the high-performance vacuum packaged high inertia accelerometer based on capacitive sensing topology which is used as particle accelerometer in sonar applications. The research problem of this project can be stated as the following: given the structural limitations and low-noise sensing circuitry, how do we design a system architecture to control the motion of the proof mass to prevent the device from being destroyed at resonance from the large displacement

To achieve the targeted Brownian noise floor in the range of $ng/\sqrt{(Hz)}$, the sensor's quality factor is required to be more than 60. Given the parameter variation due to fabrication imperfection and the presence of weak actuator force in the structure, it is challenging to design a closed-loop system that stabilizes the loop and suppresses the large displacement at resonance. The primary goal of this work is to investigate and successfully implement a way of suppressing the resonance.

To attain the objective a system-level simulation for the whole system is developed to realize the sensor's behaviour. The ideas and results presented in this dissertation can be applied to other type of High Q sensor.

1.4. Thesis Outline

This thesis proposes a novel method for suppressing the accelerometer's high displacement at resonance. An overview of the background, models, a proposed system architecture, and experimental results related to the sensor is presented in this thesis.

The overall background and motivation for this work are presented in **Chapter 1**, followed by the objectives.

Chapter 2 delves into the several types of control topologies for MEMS accelerometers used by other researchers, as well as the fundamentals required to build one.

The targeted accelerometer for implementing the control system is introduced in **Chapter 3**, along with a simulation of the system's open-loop response.

In **Chapter 4**, the electrostatic actuators and the force balancing architecture are discussed in detail. It also describes the control objective and controller's role in generating equivalent voltage commands for the actuators. Further, we introduce a novel system architecture for effective actuator utilization, which lowers the voltage demand for generating the counterbalance force.

The functional characterization of the sensor in open-loop configurations is discussed in **Chapter 5**. It also discusses the setup and outcomes of the measurements in the open loop configuration. The reported results demonstrate that the given accelerometer operates in an open loop as intended.

Chapter 6 discusses the closed-loop implementation, setup for testing and the results in frequency and time domain for the proposed controllers.

The dissertation is concluded in **Chapter 7** by summarizing the work, achievements, and challenges encountered in deploying the closed-loop system to reach the objectives.

Chapter 2.
MEMS Accelerometer Architectures

This chapter presents the working principle of a MEMS accelerometer, physics of sensing, and actuator mechanism. Finally, a review of closed-loop methods that have been used so far is reported.

2.1. Working Principle

A capacitive-type accelerometer translates external acceleration experienced by the system in a particular direction to a change of capacitance caused by inertia displacement. Directional measurement of the sensor makes it attractive for different sensing applications.

A basic type of capacitive accelerometer is depicted in Figure 2.1(a). It comprises of comb drives attached to a proof mass and anchored by a set of fixed beams. When an external acceleration is applied, the proof mass is displaced from its rest condition. This displacement is captured by differential change of capacitance formed by the parallel plate structure, as shown in Figure 2.1(a). Due to external acceleration applied on the system, proof mass movement will also experience a resistive force generated by spring and squeeze film damping force due to the presence of air or gas molecules in the sensor package [16].

With the use of readout circuitry, the change in capacitance of the accelerometer is then translated to voltage. A linear relationship exists between the proof mass displacement and the output voltage. As a result, the acceleration sensed by the system is proportional to the output voltage. This type of arrangement for the operation of the sensor is regarded as an open-loop configuration. In the capacitive-based closed-loop accelerometer, proof mass displacement is opposed by a set of differential electrostatic actuators, and sensing is carried out through the actuator.

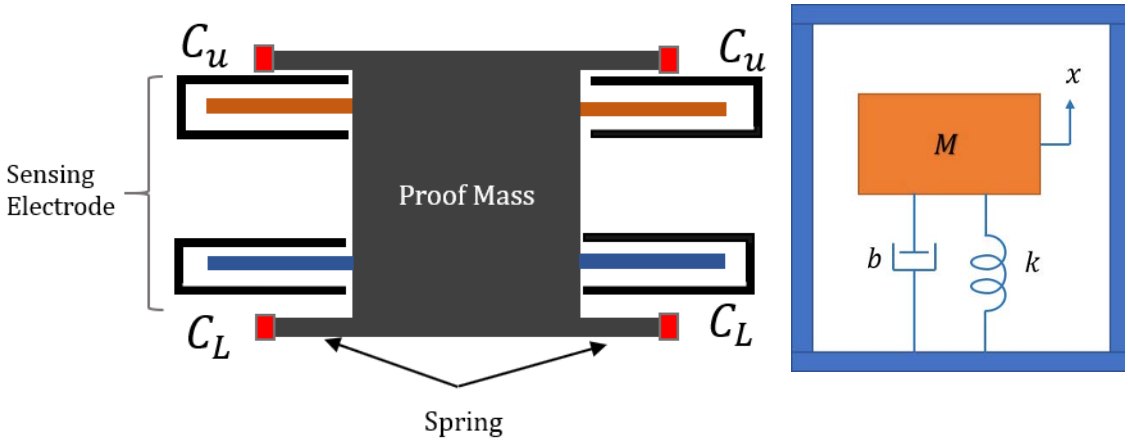

(a) (b)

Figure 2.1 (a) Simplified MEMS accelerometer structure and (b) mechanical lumped parameter schematic of the accelerometer.

From a physical viewpoint, the mechanical side of the sensor can be modelled as a mass, spring, damper system with the lumped parameters. The dynamics of the system can be described by a second-order differential equation. Figure 2.1(b) shows the lumped model of an accelerometer where *M* represents the effective mass of the whole system. Flexible beams attached to the proof mass can be pictured as a spring with the stiffness of *k*. Squeeze film damping of the system originated in the electrodes, and proof mass can be modelled as a dashpot with damping coefficient *b*. Due to the mass inertia, a lag exists between the proof mass and the frame motion. Hence, the relative displacement of the proof mass *x* would be equal to the difference between the absolute displacement of the proof mass and sensor frame. Equation of motion of the lumped system can be written by applying newtons second law of motion

$$M\frac{d^2x}{dt^2} + b\frac{dx}{dt} + kx = ma_{external} = F_{external} \qquad 2.1$$

At the steady-state condition, equation 2.1 becomes

$$kx = ma_{external}$$

$$\frac{x}{a_{external}} = \frac{m}{k} = \frac{1}{\omega_o^2} = Sensitivity \tag{2.2}$$

where $\omega_o = \sqrt{\frac{k}{M}}$ represents the natural frequency of the undamped accelerometer. Practically, this also represents the bandwidth of the system.

Taking Laplace transformation of the equation 2.1, the system transfer function from the input force to output displacement can be written as

$$H_{acc(F\to x)} = \frac{X(s)}{F(s)} = \frac{\frac{1}{M}}{s^2 + \frac{b}{M}s + \frac{k}{M}} = \frac{\frac{1}{M}}{s^2 + \frac{b}{M}s + \omega_o^2} \tag{2.3}$$

Thus, the transfer function from the inertial acceleration to output displacement would be

$$H_{acc(a\to x)} = \frac{X(s)}{a(s)} = \frac{1}{s^2 + \frac{b}{M}s + \omega_o^2} \tag{2.4}$$

2.1.1. Quality Factor

One of the critical dimensionless parameters that aid in understanding the amount of damping present in the system is the quality factor. An oscillatory system is defined as a ratio of energy stored to the energy dissipated in one cycle. A higher-quality factor means less dissipation of the energy and thus a longer oscillation period. For a spring-mass damper system, it can be realized as viscous damping and can be written as

$$Q = \frac{\omega M}{b} = \frac{\sqrt{Mk}}{b} \tag{2.5}$$

where M is the effective mass, k is the spring constant, and b is the damping coefficient.

In terms of the quality factor equation, 2.4 can be written as

$$H_{acc(a\to x)} = \frac{\mathrm{X(s)}}{\mathrm{a(s)}} = \frac{1}{\mathrm{s}^2 + \frac{\omega_o}{\mathrm{Q}}\mathrm{s} + \omega_o^2} = \begin{cases} \frac{\mathrm{M}}{\mathrm{K}} = \frac{1}{\omega_0^2} & \omega \ll \omega_o \\ \mathrm{Q}\frac{\mathrm{M}}{K} & \omega = \omega_o \\ \frac{1}{\omega^2} & \omega \gg \omega_o \end{cases} \qquad 2.6$$

Figure 2.2 shows the frequency response curve for an accelerometer. Based on the quality factor, the operation region for an accelerometer can be divided into three areas: underdamped, overdamped and critically damped. Q >0.5 means the system is underdamped. In this case, less damping contributes to less energy dissipation, resulting in more oscillatory behaviour and a large displacement at resonance that is Q times larger than its static displacement. In high-performance, low noise accelerometers, a higher quality factor leads to a better noise performance, discussed later.

2.2. Noise Source in Accelerometers

MEMS devices are susceptible to a wide range of noise sources, including mechanical and electrical noise. Mechanical noise is caused by the random motion of the surrounding gas or air molecules. This phenomenon can be explained by the Brownian motion of molecules at nonzero absolute temperature. The agitated gas molecules due to a non-zero absolute temperature strike the sensor's mechanical structure, which results in a random unbalanced dynamic force. The spectral density of the force is given by[17]

$$F_{BN} = \sqrt{4K_bTb}\,, \frac{V}{\sqrt{Hz}} \qquad 2.7$$

Where K_b is the Boltzmann constant, $T$is the temperature in Kelvin, and b is the damping coefficient.

This noise can also be regarded as Brownian noise. The quality factor is a good representative of the mechanical noise floor. Higher quality indicates lower mechanical noise in the system. The equivalent acceleration due to the Brownian noise (BNEA) can be written as

$$BNEA = \sqrt{\frac{4K_bT}{MQ}}, \frac{ms^{-2}}{\sqrt{Hz}} \qquad 2.8$$

As can be seen from equation 2.8, Brownian noise can be reduced by increasing the mass and by the quality factor of the sensor

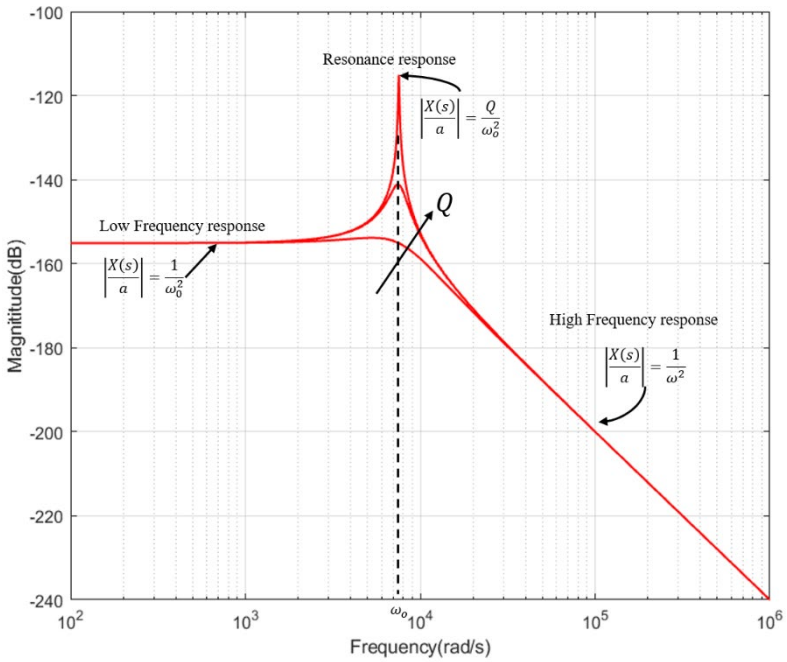

Figure 2.2 Frequency response of an accelerometer.

Another type of noise in MEMS devices is electronic noise because of its inevitable integration with different types of electronic components and other circuitry for the sensor's interface, transduction, and actuation method.

Temperature-induced fluctuation in carrier densities, random production, the annihilation of electron-hole pairs, variable trapping, and release of carriers in conductors are the leading electronic noise generation mechanisms [15]. Furthermore, noises are frequency-dependent, and various types of noise are dominant at different frequency spectrums. For example, flicker noise is dominant at high-frequency, whereas white noise can be seen in low-frequency. Overall, electronic noises are the combination of shot noise, thermal noise, flicker noise, etc., and should be handled carefully while modelling for the analysis.

Quantization noise in the system mainly arouse from the rapid change of input signal in the full-scale range of quantizer [4]. It can be treated as a white noise originating from analog-to-digital (ADC) or a digital-to-analog (DAC) converters. DAC is mainly used in the closed-loop configuration for applying an analog voltage to the electrode. Thus, QNEA noise is present in digital systems regardless of the sensor configuration.

Assuming that noise sources are uncorrelated, the total noise equivalent acceleration (TNEA) of the accelerometer system is the square root of the summation of the squared mechanical noise equivalent acceleration (MNEA), squared electrical noise equivalent acceleration (ENEA), and squared quantization noise equivalent acceleration (QNEA). Total noise equivalent acceleration imposes a restriction on the resolution of the devices.

$$TNEA = \sqrt{MNEA^2 + ENEA^2 + QNEA^2} \tag{2.9}$$

2.3. Displacement to Capacitance Conversion

MEMS capacitive-based accelerometers are parallel plate structures that form capacitors to detect displacement in the nm range via capacitance change. Figure 2.3 shows a typical parallel plate capacitive sensing configuration. A movable electrode with the proof mass forms two capacitive plate structures. At rest, the gap between

the movable electrode and the fixed electrodes is the same and equal to d_0. Capacitances formed between the movable electrode and fixed electrodes are C_{p0} and C_{n0}. If the overlapping area of the electrodes is A, then it can be written as

$$C_{p0} = C_{n0} = \frac{\varepsilon A}{d_0}, where\ \epsilon\ is\ the\ air\ permittvity$$

When an external acceleration causes the proof mass to deflect, one of the fixed nominal capacitances increases while the other decreases.

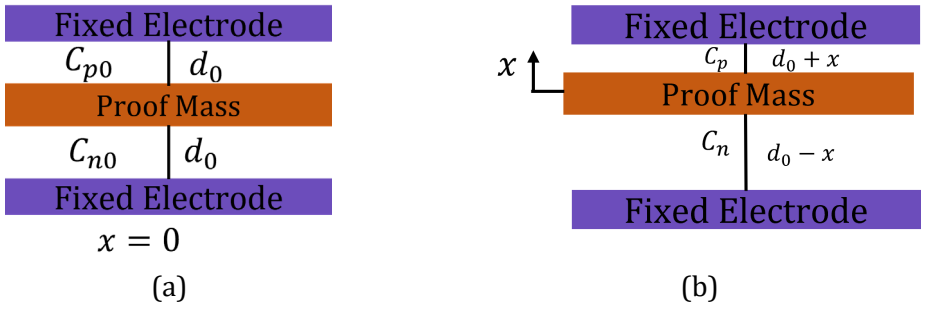

Figure 2.3 Capacitive sensing principle of a micromachined acceleormeter

The capacitance variance can be written as

$$C_p = \frac{\varepsilon A}{d_0 - x} \qquad 2.10$$

$$C_n = \frac{\varepsilon A}{d_0 + x} \qquad 2.11$$

Total change in the capacitance due to the applied acceleration can be expressed as

$$\Delta C = C_p - C_n = \varepsilon A\left(\frac{1}{d_0 - x} + \frac{1}{d_0 + x}\right) = \varepsilon A \frac{2x}{d^2 - x^2} \qquad 2.12$$

Equation 2.12 shows that the change of capacitance is non-linear with respect to the displacement of the proof mass. If the proof mass deflection is small in

comparison to the nominal gap, the differential change in capacitance becomes a linear measure of the proof mass displacement and can be expressed as

$$\Delta C = \varepsilon A \frac{2x}{d^2}, for \ x \ll d_0 \qquad 2.13$$

This assumption may not hold true in an open-loop accelerometer at large acceleration, leading to the non-linear behaviour of the sensing element.

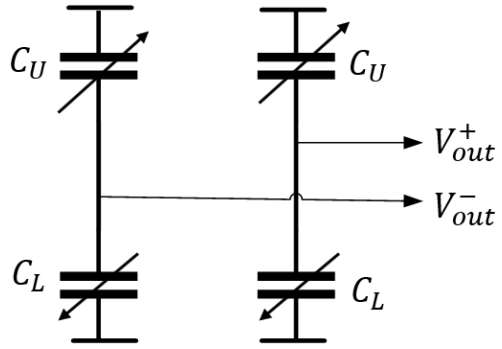

Figure 2.4 Electrical model of the differential sensing element

The comb drive is the most commonly used sensing element in capacitive-based accelerometers. It might be represented as a series of parallel-plate structures. In Chapter 3, the comb drive structure is presented in detail. Figure 2.1(a) shows that a typical accelerometer has four electrodes forming two differential electrodes. The electrical representation of the sensing model can be illustrated as shown in Figure 2.4.

2.4. Capacitive Differential Sensing Interface

As previously stated, the change in capacitance caused by proof mass motion is related to external acceleration. To map the acceleration information in the electrical domain, differential AC carrier signals are applied on the differential electrodes set for modulating the capacitance value to electrical current. Figure 2.4 shows the simplified readout circuitry that includes modulation, demodulation, and signal amplification. The capacitor (C_u,C_L) in the circuit depicts the differential

sensing electrode operation. When an acceleration is applied to the accelerometer, the change in the sensing electrode capacitance on one side would be larger than the other side. For example, due to the applied acceleration, the upper electrode current is large than the lower electrode current, creating an excess current represented by Equation 2.15. This current would flow towards the amplifier at the same phase as the carrier signal. This way, the magnitude of the capacitance difference and direction of applied acceleration will be passed onto the electronics readout

$$v_{ac} = V_0 \cdot sin(\omega t) \tag{2.14}$$

$$\Delta i_{in} = i_u - i_L = (C_u - C_L)\frac{dv_{ac}}{dt} = V_0 \Delta C \omega \cos(\omega t) \tag{2.15}$$

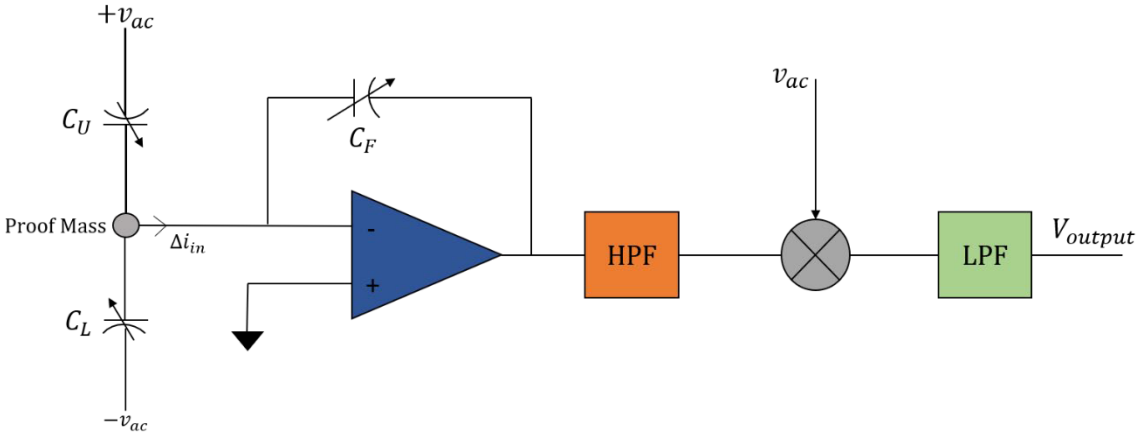

Figure 2.5 Capacitive readout circuitry.

To convert this current to a voltage, a trans-impedance amplifier is used, which gives the benefit of using small capacitance rather than a large gain resistor at the feedback network of the amplifier. The modulated voltage signal is demodulated to the base band range after amplification and then filtered with a low pass filter

2.5. Electrostatic Actuation

Several micro actuation techniques have been investigated and developed over the past years in the MEMS community, depending on the application

requirement. Bell did a comprehensive study on different micro-actuators based on their performance [18]. It consists of mainly four actuators namely thermal, magnetic, piezoelectric, and electrostatic. In this application, capacitive-based micro-actuators are deployed for easy fabrication techniques, low power consumption, and high-speed response time. Figure 2.6 shows a simple parallel plate type configuration.

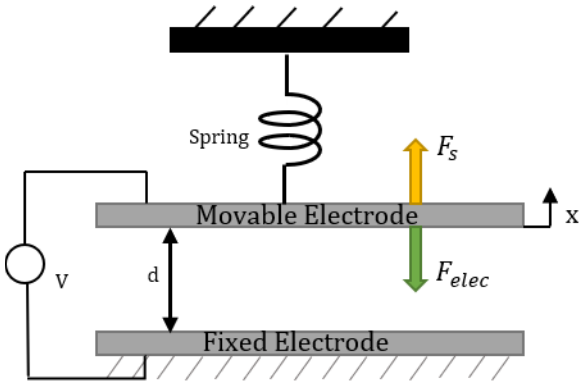

Figure 2.6 An illustration of a single electrode structure

Electrostatic actuators create attractive force when a potential difference is made between two plates, and it is inversely proportional to the square of the distance between plates. In this actuation architecture, a fixed plate is used to counteract the displacement of the movable plate. Because of its nonlinear nature, when the gap between the plates narrows to apply a significant potential difference, a large force is generated. In Figure 2.6, an electrostatic actuator is shown. When a voltage V is applied across the plate, an equal and opposite charge builds on the upper and lower plates, causing an attractive force and a displacement x in the movable plate. The reduced gap changes the capacitance between the plates and stores potential energy due to the work done. If the capacitance between the plates is C, then the energy stored in the system can be expressed as

$$E = \frac{1}{2}CV^2 \qquad 2.16$$

Hence, electrostatic force can be computed as

$$F_{el} = \frac{dE}{dx} = \frac{1}{2}\frac{dC}{dx}V^2 \quad 2.17$$

$$F_{el} = -\frac{1}{2}\frac{\epsilon A}{(d-x)^2} \quad 2.18$$

Equation 2.18 shows that the actuator force is proportional to the overlapping area of the capacitor and inversely proportional to the displacement of the proof mass. The negative sign indicates that it is always an attractive force. Electrostatic actuators are generally implemented either by voltage-controlled, or charge-controlled scheme [19].

2.5.1. Pull-in Voltage

In voltage-controlled actuation mechanism, potential difference is applied to a plate that helps to reduce the gap between the plates. At a small voltage, the electrostatic force is counteracted by the spring force. As the voltage increases, the force becomes larger than mechanical restoring force, and eventually, the movable plate snaps to the fixed end. This phenomenon is called pull-in, and the voltage at which it happens is called pull-in voltage [20]. The stiction of the two electrodes leads to a short circuit. Hence, pull-in poised a restriction on the actuator working limit. For pull voltage V_p applied to the plate at equilibrium, the spring force and electrostatic force acting on the proof mass would be equal and given by

$$\frac{1}{2}\frac{\epsilon A_t}{(d_0-x)^2}V_p^2 = kx \quad 2.19$$

By solving the equation, the displacement stability limit and pull-in voltage can be found as

$$x_{critical} = \frac{d_0}{3} \; ; V_p = \sqrt{\left(\frac{8}{27}\frac{kd_0^3}{\epsilon A_t}\right)} \tag{2.20}$$

According to Equation 2.20, the plate's travel distance is limited to less than one-third of the total gap, resulting in significant sensitivity loss in capacitive microdevices [21].

2.5.2. Spring Softening

Spring softening is the effect of reducing the system's effective spring constant induced by nonlinearities in electrostatic force. As a result, it causes the resonance frequency to decrease and sensitivity to increase. At equilibrium, the spring force on the movable plate is balanced by the electrostatic force, which is expressed by Equation 2.21. The spring softening effect can be seen by rearranging the equation as follows.

$$k_{mech}x = \frac{\epsilon A}{2d_0^2}\frac{1}{\left(1-\frac{x}{d_0}\right)^2}V^2 \tag{2.21}$$

where k_{mech} is the mechanical spring constant, and x is the displacement of the proof mass under the effect of electrostatic force.

After the Taylor series expansion of the quadratic terms, the overall net force can be written as

$$F_{net} = kx - \frac{\epsilon A}{2d_0^2}V^2\left(1+\frac{2x}{d_0}\right) = \left(k - \frac{\epsilon A V^2}{d_0^3}\right)x + \frac{\epsilon A}{2d_0^2}V^2 \tag{2.22}$$

From equation 2.22, it can be seen that the spring constant k decreased by a term that varies based on the applied voltage to the plate.

2.6. Capacitive MEMS control strategies

The mechanical and electronic noise floors must be minimized to achieve high-performance capacitive MEMS accelerometers. Therefore, recent research has concentrated on developing large-mass, low-noise circuitry-based systems to develop higher sensing areas. Higher sense area increases sense capacitance and decreases pick-off circuitry gain, resulting in lower electronic noise and increased sensitivity. Some researchers are also working on a large mass-based accelerometer that reduces the Brownian noise floor while increasing the device's sensitivity. However, it comes with the cost of design and fabrication complexity. As previously discussed, vacuum packaging is another method for reducing mechanical noise floor, contributing to the device's quality factor. Nevertheless, it comes with large displacement at resonance and ringing in the sensor output. Several techniques, including nonlinear spring design, mechanical isolators, and the implementation of the closed system, are used by different researchers to address issues related to high-quality factor-based devices, with the closed-loop system is the most discussed.

2.7. Closed-Loop capacitive architectures for Accelerometer

Vacuum-packaged accelerometers are often operated in a closed loop. The low-pressure level in the cavity requires electrical damping to limit the proof mass displacement at resonance. Furthermore, a closed-loop operation can prevent the electrostatic force's pull-in phenomenon.

There are two main force rebalancing approaches for the MEMS accelerometer interfaces, either analog or digital. Digital interfaces usually utilize ΣΔ architectures, whereas analog interfaces refer to force balancing classical control system techniques.

Electro-mechanical ΣΔ modulators are popular in the MEMS community because of their low noise and high-resolution performance. Such interfaces provide the benefit of force rebalancing and serve as an analog to digital converter of the

inertial signal. Most of the researchers worked on implementing an electro-mechanical sigma-delta modulator of a different order for implementing a feedback system.

The sigma-delta type topology operates by oversampling, noise shaping, and filtering an analog signal. Changes in consecutive signals are encoded as oversampled bit pulses in this architecture. Sampling signals much higher than the Nyquist sampling rate distributes noise power over a wide range of frequencies and hence reduce noise in the desired bandwidth. A feedback system is formed to shape the noise spectrum out of the bandwidth region. Figure 2.7. shows the 1-bit architecture of the sigma-delta type modulator. The difference between feedback and analog reference input is fed through an integrator, followed by a 1-bit quantizer. The quantizer oversampled the signal and shaped the quantization noise out of the interest band. A digital filter is also employed in this architecture to filter out the high-frequency noise and down sample the data rate to a more practical value. Finally, the digital signal is converted back to analog one and fed back to the system.

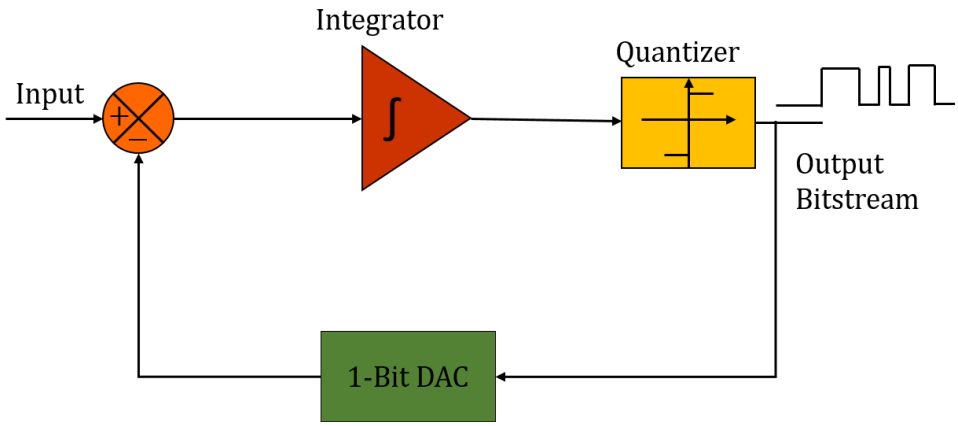

Figure 2.7 Block diagram of a sigma delta modulator

The conventional ΣΔ modulator is different from than electro-mechanical-based ΣΔ topology. The dynamics of force feedback sigma-delta architecture depends on the mechanical sensing element. It can be regarded as a second order system, which is analogous to two cascaded electronic integrators. Mechanically embedded integrators in the system are not directly accessible, making it challenging to design.

A mechanical loop filter along with analog readout circuitry, compensator, quantizer, and a voltage to force converter form a second order electro-mechanical sigma delta modulator (EMSDM), as shown in Figure 2.8. Displacement of the proof mass is converted to an analog voltage signal which is then digitized to pulse stream. As mentioned earlier, a capacitive type of accelerometer works as a parallel plate capacitor. The digital pulses applied to the capacitor plate generate an electrostatic force that balances the proof mass and brings it back to its original location. Digital pulses contain the information of the force required to maintain the proof mass in the neutral position. The stability and performance of the EMSDM depend on the sampling frequency, time delay, and nature of the feedback and sensing electrode. Higher sampling improves the signal-to-noise ratio but demands more power.

Furthermore, the coupling between electronic and quantization noise poses a limitation on SNR improvement. One common way among the community to shape the quantization noise and improve the SNR is to implement higher-order EMSDM at the lower sampling frequency [22]. However, higher-order sigma-delta has stability issues. Hence, it becomes difficult to design and implement in real systems.

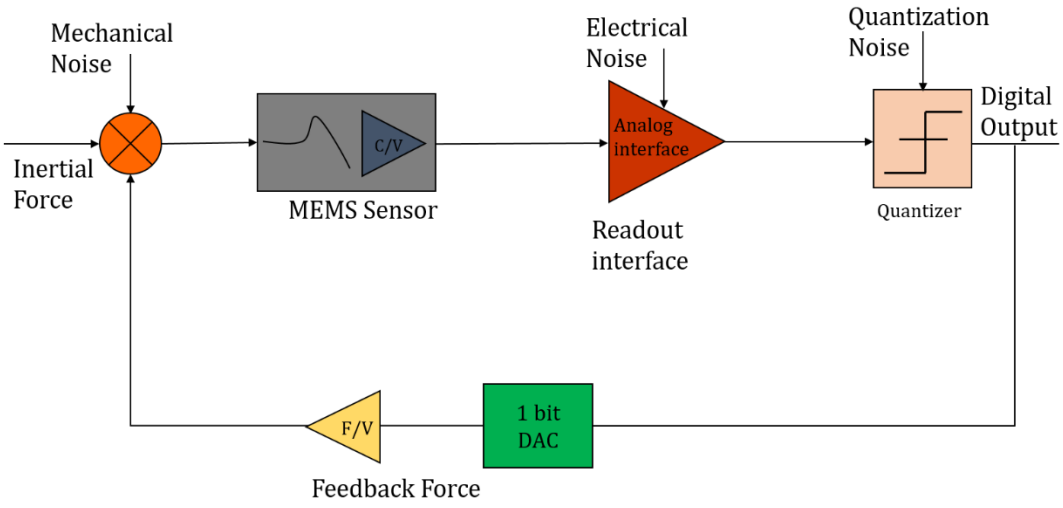

Figure 2.8 Block diagram of an electromechanical sigma-delta architecture for a MEMS accelerometer

In 1990 [23], Henrion first implemented the second-order ΣΔM to control a vacuum-packaged capacitive out-of-plane MEMS accelerometer. A 500-μm thick single-crystalline-silicon spring-mass layer was placed between two identical single crystalline silicon layers to form a mechanical sensing and control element. In this work, 10 $\mu g/\sqrt{Hz}$ noise floor was achieved due to this closed-loop action. Yazdi and Najafi [24] presented a comprehensive noise study of second order ΣΔ capacitive accelerometers to reach a sub-ug resolution. They achieved a noise floor of 0.7 $\mu g/\sqrt{Hz}$ with a bandwidth of 1KHz.

To further improve noise performance at low frequency, a third order ΣΔ with single-bit quantizer was proposed by Smith [25]. A fifth order ΣΔ interface was implemented by Dong on a large proof mass low-quality factor (Q =0.41) based capacitive accelerometer. A linearized scheme was reported to eliminate the nonlinear harmonic distortion of the electrostatic force. The noise floor showed by this accelerometer was 32 $\mu g/\sqrt{Hz}$. Table 2.1 shows similar higher order ΣΔ interfaces for low Q accelerometers found in literature. Chen [26], Boser [22], Zwahlen [27], Almut [28] all focused on developing higher-order single bit ΣΔ interface. Higher oversampling ratio, high-order noise shaping, or multibit feedback are effective methods to improve the noise shaping ability for an electromechanical closed-loop system. However, increasing the sampling frequency may result in interactions between various noise sources and increased power consumption. Furthermore, the implementation of linear multibit force feedback is a challenge for nonlinear actuators. Therefore, most of the mentioned literature is based on low Q accelerometers

Wu [29] developed a simulation model of third order multi-bit force feedback ΣΔ modulator. It is found that a multi-bit quantizer provides better stability for a high-Q MEMS accelerometer, but it is hard to implement due to the nonlinear electrostatic force actuator. Xu [30] reported a ΣΔ interface for a surface micromachined capacitive accelerometer with a quality factor above 40. Sub μg resolution is achieved by implementing the switching capacitor technique, followed by third order ΣΔ ,

resulting in fifth order ΣΔ. Overall noise floor measured in this work was lower than 200 $ng/\sqrt{Hz}$. A recent work published by Chen [31] focused on a fifth order ΣΔ interface design method using a discrete PID loop compensator to improve the performance of a capacitive accelerometer with a claimed quality factor of 200. This work achieved 1 $\mu g/\sqrt{Hz}$ noise floor at 1kHz bandwidth.

According to the preceding discussion, higher-order modulators are attractive for researchers; however, the increased number of poles in the loop filter makes stability more difficult to achieve. Therefore, another critical issue in ΣΔ modulators is design optimization. Choosing parameters such as gain constants, feedback voltage, poles and zero frequencies of a compensator, and so on is a difficult multi-parameter optimization problem [32].

Force rebalancing can also be implemented with an analog signal proportional to the acceleration. Figure 2.9 shows a simplified operation of an analog-type force rebalancing system. The accelerometer's sense electrodes are connected to a pickoff circuitry, representing acceleration measurement, and giving a sense of the proof mass displacement. The sensor's output is then fed through a compensator to ensure loop stability. Finally, the analog voltage is scaled based on the actuator geometry before being applied to the actuation electrodes to generate electrostatic force. The resultant force opposes the proof mass motion and brings it to a nominal position.

Chau [33] presented an interface that utilizes an AC clock source on the position sense electrode to modulate displacement information. It is then buffered, demodulated, and applied back to the actuator. The noise floor achieved in this work was 0.6 $mg/\sqrt{Hz}$ with 4kHz bandwidth. PI compensators were also found in the literature for dampening low Q low mass accelerometers [8]. Sarraf [34] focused on developing a less complex digital implementation of a sliding mode controller with dynamic feedback for increasing the system's flexibility on an accelerometer with a Q of approximately 9. Dynamic feedback allows the controller to adapt to the change in the system due to the fluctuation in the system's operating condition (temperature,

pressure etc. This work also stressed increasing the system's sensitivity by operating the sensor close to the pull-in regime.

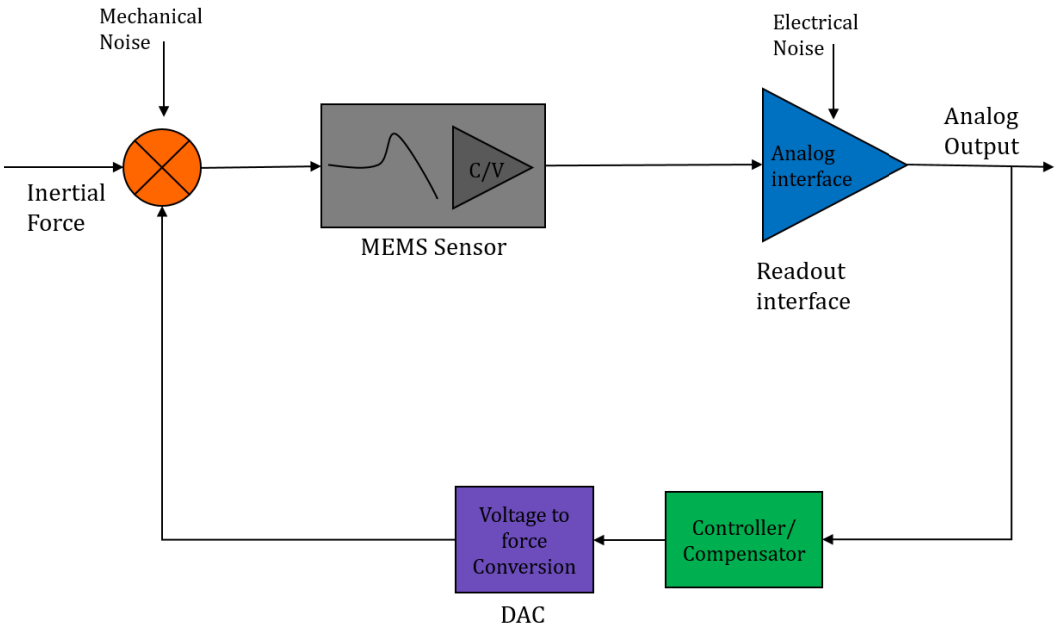

Figure 2.9 Block diagram of an analog control interface for MEMS Accelerometer

Another analog closed-loop interface is presented by Aaltonen [35]. He implemented a PID controller in an analog domain along with a detailed noise analysis of a high-quality factor (Q ~30) based accelerometer. This work demonstrates a good vibration mode damping behaviour of the closed-loop operation. In Yücetaş's work [36], [37], an AC force feedback-based PD compensator is used for applying electrostatic damping to the movable electrode on a high-resolution accelerometer with a Q more than 700. This work employed a charge control interface to generate electrostatic damping and achieved a noise floor of 1 $\mu g/\sqrt{Hz}$ at 400 Hz bandwidth. The electrostatic damping mechanism used in the system becomes active after a 300 Hz frequency. However, the work does not present any results regarding the effective vibration suppression of the high Q resonance peak.

Table 2.1 Summary of reported high Q closed-loop accelerometer

Author	Controller Type	Topology	Quality Factor (Q)	Noise Floor	Bandwidth, FS	Year
Henrion [23]	2^{nd} Order ΣΔM	Digital	Vacuum Packaged	10 $\mu g/\sqrt{Hz}$	-------	1990
Boser [38]	2^{nd} Order ΣΔM	Digital	1	1.6 $mg/\sqrt{Hz}$	50 Hz, ±5g	1995
Najafi [24]	2^{nd} order ΣΔM	Digital	16	1.5 $\mu g/\sqrt{Hz}$	1kHz, ±1.35g	2000
Amini [39]	4^{th} order, CIDF	Digital	0.3	4 $\mu g/\sqrt{Hz}$	500 Hz, ---	2006
J. Wu [29]	3^{rd} order ΣΔM	Digital	1000	4.5 $\mu g/\sqrt{Hz}$	2kHz, 5g	2006
Aaltonen [35]	PID controller	Analog	30	----------	300 Hz	2009
Dong [40]	5^{th} Oder, CIDF	Digital	0.41	32 $\mu g/\sqrt{Hz}$	1 kHz, ±1g	2010
Almut [28], [41]	MASH	Digital	10	47 $\mu g/\sqrt{Hz}$	1 kHz, ±1.5g	2012
Sarraf [42]	Sliding Mode	Digital	9	3.3 $\mu g/\sqrt{Hz}$	4.9KHz, ---	2013
Yücetaş [36], [37], [43]	PD controller	Analog	>700	2 $\mu g/\sqrt{Hz}$	200 Hz, ±1.5g	2013
Chen [26]	6^{th} order EM	Digital	Vacuum Packaged	15 $\mu g/\sqrt{Hz}$	500 Hz, ±6g	2014
Terzioğlu [44]	PI Controller	Analog	3	~10 $\mu g/\sqrt{Hz}$	200 Hz, ±3.5g	2015
Xu[30]	4^{th} order ΣΔM	Digital	40	200 n$g/\sqrt{Hz}$	300 Hz, ±1.2	2015
Ciotirca [45]	D controller	Digital	2000	0.62 $\mu g/\sqrt{Hz}$	4.1 kHz	2017
Chen [31]	PID + 5^{th} order ΣΔM	Hybrid (Analog - PID+ Digital EM)	200	1 $\mu g/\sqrt{Hz}$	1kHz	2019

Ciotirca [45] proposed a low-power analog front-end circuitry design for an underdamped (Q = 2000), three-axis dual-mass accelerometer. This work also utilized a linearized relationship between the proof mass and electrostatic force to implement a simultaneous discrete derivative multi-rate controller for reducing the system's settling time. Although the setting time of the system was considerably reduced, the author did not present any results regarding displacement suppression arising at resonance.

As seen by the above discussion, there are various researches on implementing closed loops to improve accelerometers performance. Still, only a few of them concentrated on high-quality factor based accelerometers. Designing a closed-loop control system for high Q devices is challenging due to the higher-order resonance arising from the sensing element, which is usually sufficiently damped at atmospheric pressure but becomes severely underdamped in a vacuum, resulting in a phase lag approaching 180 degrees [32]. Some of the authors successfully dealt with the instability caused by the underdamped sensor but at the expense of circuit complexity. The literature also shows that most authors worked on low mass-based accelerometers that require less actuator effort. This study dealt with a large mass high Q-based accelerometer using a relatively simple framework for suppressing its displacement at resonance.

Chapter 3.
State of Art ISL Accelerometer: Design and Simulation

Dr. Behraad's research team at SFU's Intelligent Sensing Laboratory (ISL) has been developing cutting-edge, state-of-the-art accelerometers for several years. Compared to other sensors on the market, accelerometers designed in ISL have a higher bandwidth, a wide dynamic range, and a lower noise floor. This chapter discusses the open-loop system's fabrication, design, modelling, and simulation.

3.1. Design Criteria

Fundamental metrics for designing a high-performance accelerometer are bandwidth, sensitivity, resolution, and noise floor. As shown in Figure 3.1, all these performance metrics are interdependent. While designing a device structure, a designer must establish a trade-off between device performance and dimensions to meet the design objectives. For instance, device sensitivity is a function of electrical and mechanical gain factors, as shown in Equation 3.1.

$$S_{a_{in}}^{\Delta C} = S_{\Delta C}^{\Delta V} \cdot S_{\Delta x}^{\Delta C} \cdot S_{a_{in}}^{\Delta x} = \frac{\partial V}{\partial C}\frac{\partial C}{\partial x}\frac{\partial x}{a_{in}} = G\frac{\varepsilon A}{d^2\omega_o^2} \qquad 3.1$$

Where G is the gain of electronic circuitry required for converting capacitance to voltage, d is the gap between the capacitor, and A is the effective actuation area.

In Equation 3.1, displacement to capacitance conversion sets the mechanical gain while the capacitive to voltage conversion ratio determines the electronic gain. To achieve an overall high level of sensitivity, both factors can be maximized. However, increasing the electronic gain would result in higher electronic noise, whereas increasing the mechanical gain would require increasing the device's output capacitance. Additionally, increasing capacitance necessitated modifications to device structural aspects such as increasing the number of fingers, narrowing the gap between the sense capacitance, etc. Again, changing the device dimensions impacts

other performance factors, including bandwidth and noise floor, as shown in Figure. 3.1. Overall, the practicability of optimizing device dimensions is also limited by the availability of fabrication technology. Considering all reasonable factors into account, a high-performance accelerometer was designed, fabricated, and tested. In the following section, the design and fabrication method of the ISL accelerometer is described.

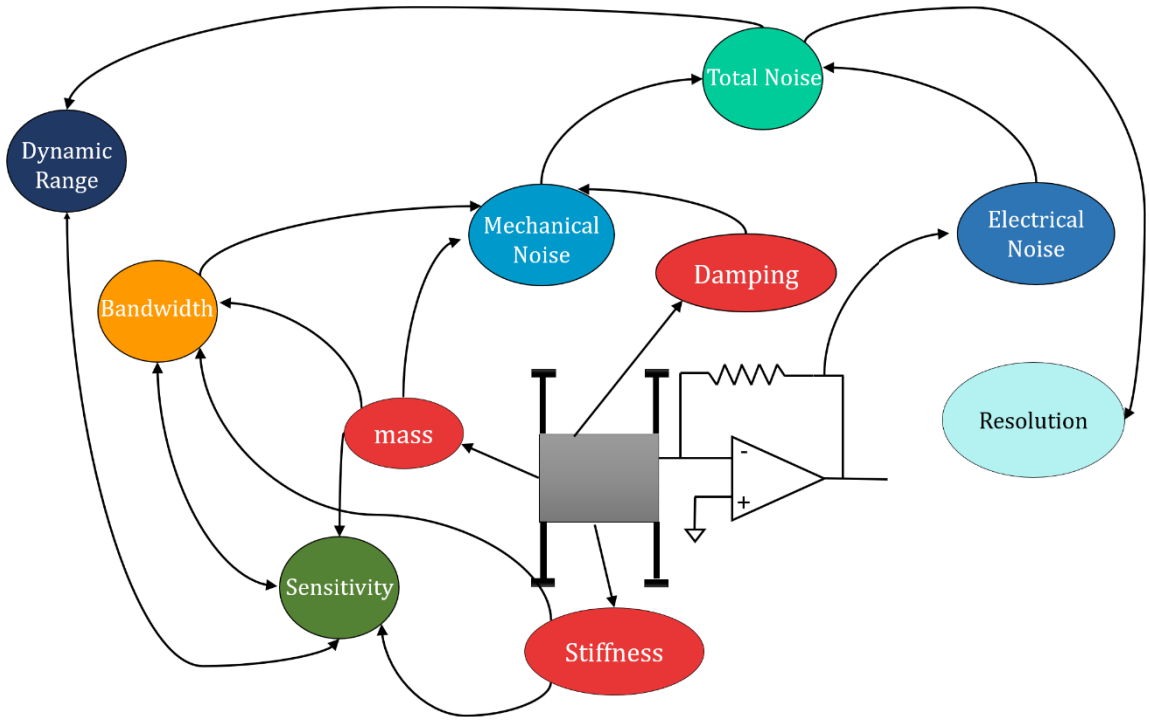

Figure 3.1 Relation between design parameters and performance metrics of a MEMS accelerometer

3.2. In-plane ISL Accelerometer

With the performance parameters and constraints in mind, a state-of-the-art in-plane accelerometer is designed for the Sonobuoy application. This accelerometer comprises four transverse capacitive comb drive configurations attached to a 100μm thick bulky proof mass, four clamped-guided suspension beams attached to the substrate, and one pair of horizontal electrodes, as shown in Figure 3.2. Each Comb drive comprises 69 movable fingers coupled with the proof mass. Furthermore, every movable finger, hinged to the accelerometer frame, is encompassed by two fixed

fingers, each with the gaps $d_0$and $d_{0,a}$. Thus, a fixed set of electrodes around the comb drive forms a gap varying capacitance sensing mechanism. These comb drives are named as an upper right electrode, upper left electrode, lower right, and lower left, and total capacitance formed by each comb drive can be referred to as respectively $\Delta C_{U,R}, \Delta C_{U,L}$, $\Delta C_{L,R}, \Delta C_{U,L}$. These comb drives are used as a sensor in the system. Another set of electrodes, known as a top (ΔC_T) and bottom electrode (ΔC_B) is positioned horizontally with the proof mass. These electrodes are placed mostly for actuation purposes. When the proof mass and the fingers move upward, the gap in the upper sets of electrodes (UR and UL) increases and decreases the capacitance while the gap in lower sets of electrodes (LR and LL) decreases. Thus, the whole configuration forms a differential sensing mechanism.

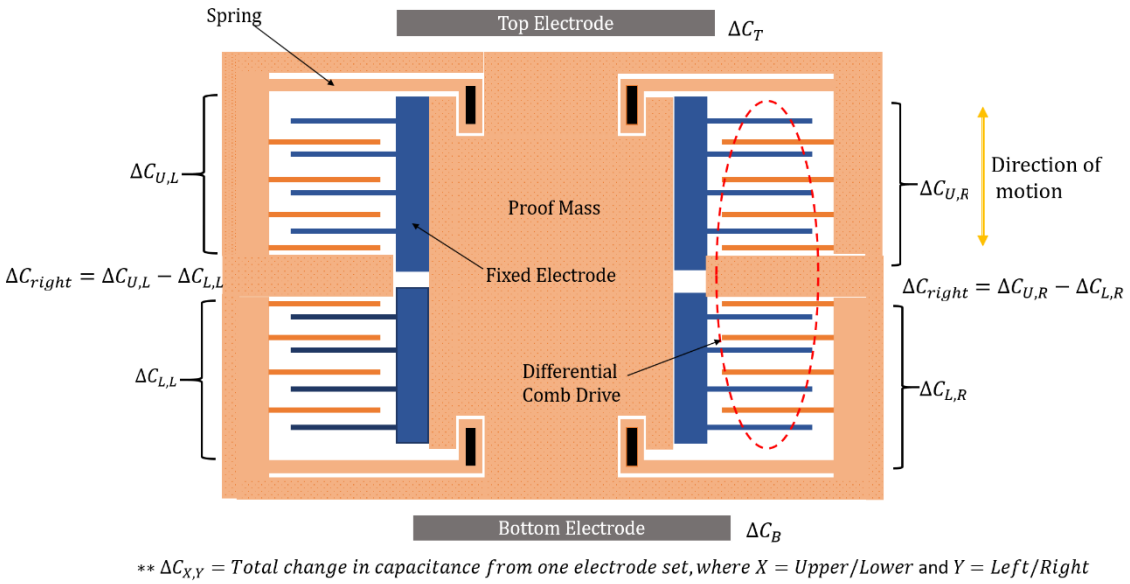

Figure 3.2 Schematic of the ISL MEMS accelerometer

Capacitance in the upper set of electrodes ($C_U = C_{U,L}, +C_{U,R}$; and $C_{U,L} = C_{U,R}$) can be written as

$$C_U = N \times \frac{2\epsilon A}{d_o - x} + (N-1) \times \frac{2\epsilon A}{d_{o,a} + x} \qquad 3.2$$

Where N is the number of capacitors formed in one set of comb drives formed due to the gap, d_o, (N-1) is the number of capacitors formed by anti-gap, d_o, a . A is the overlapping area in each finger pair, ϵ is the permittivity of air, x is the displacement of the proof mass

Similarly, for the bottom electrode

$$C_L = N \times \frac{2\epsilon A}{d_o + x} + N \times \frac{2\epsilon A}{d_{o,a} - x}; where\ (N-1) \approx N \qquad 3.3$$

By taking the derivative of equation 3.2, we get

$$\frac{dC_u}{dx} = N \times \frac{2\epsilon A}{(d_o - x)^2} - N \times \frac{\epsilon A}{(d_{o,a} + x)^2} \qquad 3.4$$

Similarly, from equation 3.3,

$$\frac{dC_L}{dx} = -N \times \frac{2\epsilon A}{(d_o + x)^2} + N \times \frac{\epsilon A}{(d_{o,a} - x)^2} \qquad 3.5$$

Equations (3.4) and (3.5) represents the amount of capacitance change per unit displacement of proof mass due to the external acceleration. This can also be referred to as the sensitivity of the device.

In each unit cell, the capacitance formed by anti-gaps reduces the capacitance of the gap and hence affects the sensitivity, which can be seen in Equations (3.2) -(3.5). If both interval and anti-gap are equal, the net sensitivity for a very small displacement ($x \approx 0$) will be zero. For this reason, the sensing element is designed with large anti-gap separations, which reduces the influence on sensitivity significantly. So, considering the anti-gap is much larger than the nominal gap, the capacitance formed by the anti-gap can be ignored, and net capacitance change can be written as

$$\Delta C = C_u - C_L = \frac{\epsilon A_t}{d_o - x} - \frac{\epsilon A_t}{d_o + x} = \frac{2x\epsilon A_t}{d_o^2 - x^2}; where\ A_t = N \times A. \quad 3.6$$

If the deflection of the proof mass is small compared to its nominal gap, then the differential change of capacitance becomes linear and can be written as

$$\Delta C = \frac{2\epsilon A_t}{d_o^2} x = Kx, \qquad x \ll d_o \quad 3.7$$

Table 3.1 Physical characteristics of the ISL acccelerometer

Parameters	Values
Proof Mass (mg)	8
Thickness (μm)	100
Dimension (Length X Width, μm^2)	6000 × 6000
Natural Frequency (Simulation, Hz)	1330
Natural Frequency (Experimentally, Hz)	1280
Stiffness Coefficient (N/m)	450
One overlap Sensing electrode (μm^3)	720 × 10 ×100
Number of sensing electrode	69 × 4
One Actuation electrode (μm^2)	6000 × 100
Pull In voltage (sensing, V)	26
Pull In voltage (Actuation, V)	76

As shown in Figure 3.4, a device layout is created using the dimensions specified in Table 3.1. This layout is utilized to create a 3D model of the device as well as the mask for fabrication, which will be discussed in the subsequent section. During the design process, it was ensured that different vibration modes did not interact with one another. A modal simulation was performed using the 3D model to confirm the system's dynamic properties.

Simulation results for the first four natural frequencies are shown in Figure 3.3. The first natural frequency is an in-plane mode shape with a frequency of 1.3 kHz, which matches the theoretical prediction. Additionally, other resonance frequencies of the proposed design may be seen far away from the first natural frequency, ensuring that the other modes do not interfere with the signal bandwidth.

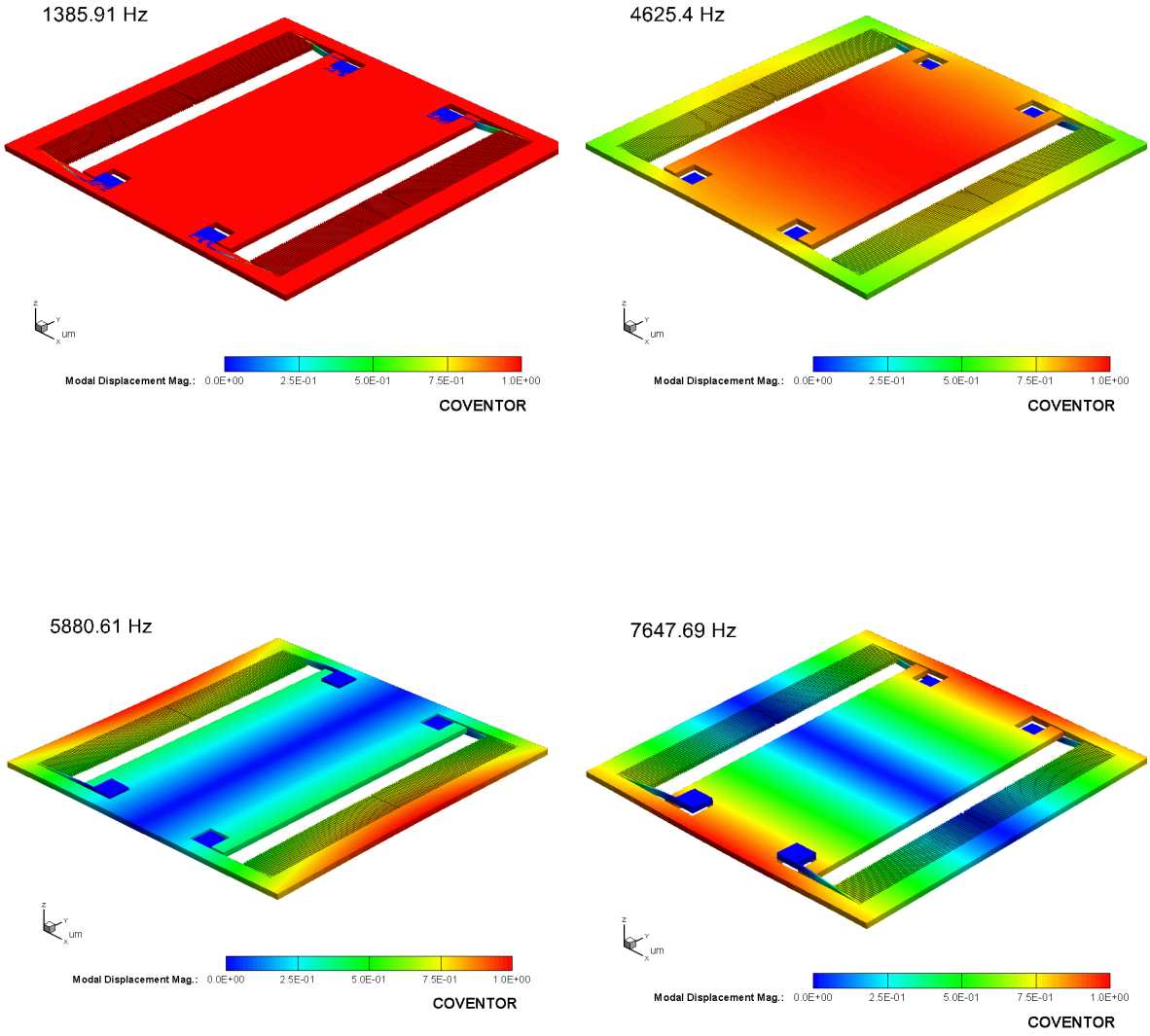

Figure 3.3 Simulated mode shape of the ISL accelerometer

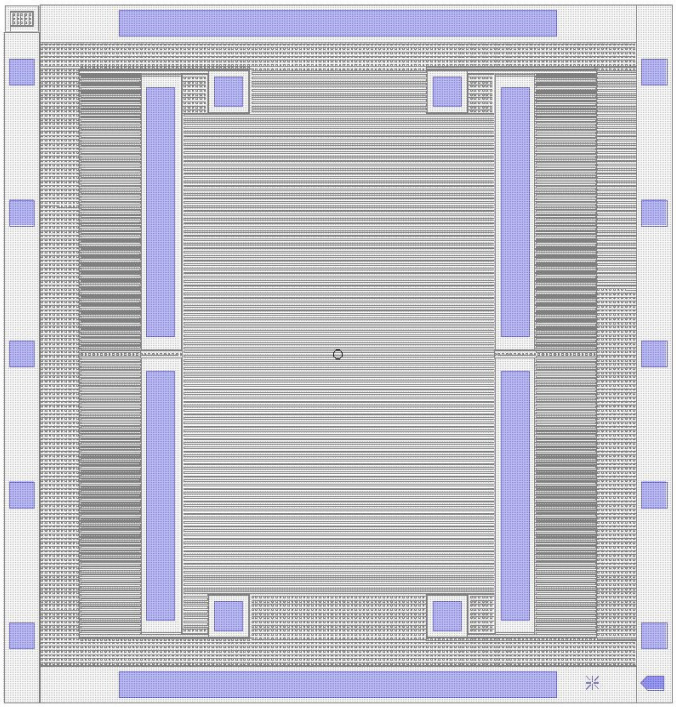

Figure 3.4 Layout of the ISL accelerometer

3.3. Fabrication Process

Micro-Fabrication is a process of creating micro- and nano-scale mechanical structures on a material with the help of micromachining techniques. Fabrication of micro-scale devices requires high precision instruments and optimized process parameters for the operations involved. The whole fabrication process is sensitive to air particles, and hence it has to be carried out in a clean room environment. The proposed accelerometer's fabrication was carried out partly in the clean room facilities of the University of Michigan and partly in 4D LABS at Simon Fraser University

Silicone is a popular material for MEMS devices because of its excellent mechanical properties and options for integrating electrical functionality within the device. The proposed device is fabricated on p-type silicon on an insulator wafer (SOI) using a bulk micromachining process, which is a selective subtractive machining process that usually removes a bulk of material through deposition,

photolithography, and etching processes. The SOI wafer used for the microfabrication process includes a 100 μm thick device layer, a 5μm buried oxide layer (BOX layer), and a 500 μm handle wafer. Figure 3.5 illustrates the fabrication processes of the accelerometer.

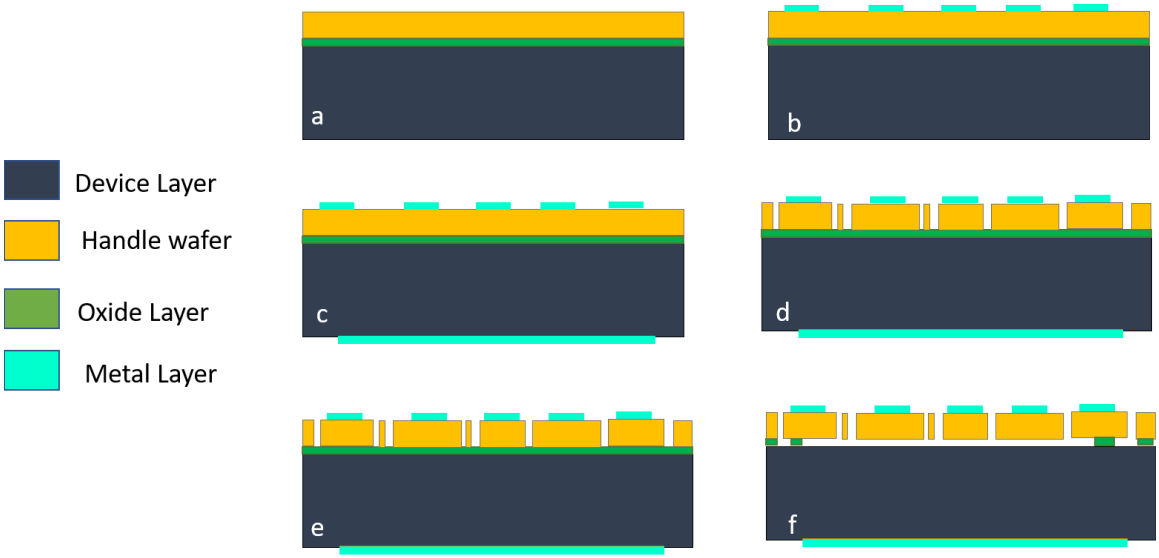

Figure 3.5 Fabrication Process of the ISL accelerometer
(a) starting material is an SOI wafer with 100µm device layer, 5µm BOX layer, and 500µm handle wafer, b) metal deposition using lift-off process on device layer, c) metal deposition on handle wafer using a shadow mask, d) PECVD of $SiO2$ on device layer as the masking layer for DRIE, e) HF etching of the oxide layer and DRIE of the device layer, and f) Release structures using vapor HF.

The first phase in the fabrication process is the lithography, which involves transferring geometric patterns from a mask to a thin layer of light-sensitive polymer, known as a photoresist. In the mentioned device, three masks were used, including two lithography steps and one shadow mask. First, one lithography mask defined metal contact, shown in Figures 3.5(a) and 3.5(b). The physical vapour deposition technique was then used to deposit a 20 nm of Chromium and 200 nm of Gold on the device layer of the SOI wafer. Following that, a lift-off method was used to form the metal contacts on the wafer.

The handle layer of the SOI wafer was then deposited with the 20 nm of Chromium and 200 nm of Gold using a shadow mask. The final lithography mask was used to pattern the device layer using the deep reactive ion etching process, where

deposited SiO_2 and a thick layer of photoresist worked like a mask. The proposed device has 100 μm depth with a 2 μm gap between the sensing fingers. Using DRIE to obtain a high aspect ratio of the device was one of the most challenging fabrication processes. The wafer was then diced using the Stealth Laser Dicing technology. Finally, the device was released by etching the buried oxide layer using vapour HF etching. The released device was then packaged in a leadless chip carrier and wire bonded.

3.4. Packaging Process

To ensure proper operation of the accelerometer and establish an electrical connection, the packaging is an essential and final step before testing. Generally, wafer-level packaging and chip-level packaging are the two main techniques for a MEMS device. In this device, 44-pin Ceramic Leadless Chip Carriers (LCC) were used for packaging. The dimension of the package was 12.04 (±0.25) mm × 12.04 (±0.25) mm × 2.24 (±0.23) mm. The cavity of the package was coated with a layer of gold. The packaging process was performed using SRO-700 Vacuum Packaging System.

The next step in the packaging process was wire-bonding. The electrical connection between the MEMS device and the package is formed by wire-bonding. As a result, the MEMS device can be connected to the electrical circuit. A wedge-ball K&S 4700 wire bonder was used for wire bonding. The whole wire bonding process was also performed in the SFU facility at 4D Labs. The accelerometers were temporarily covered with lids and tapes for characterization and experimental studies following wire bonding. After the devices' functionality is confirmed, the accelerometers will be sealed and encapsulated using a process developed by Yuxi Zhang at Intelligent Sensors Laboratory.

3.5. Open Loop System Simulation

In this section, the proposed Accelerometer is simulated in MATLAB Simulink environment using the models described in the previous chapters. Table 3.1 shows

the different design parameter values used in the simulation and fabrication of the device. In an open-loop system, the mechanical sensing element and the electronic pick-off circuity for capacitance to voltage conversion are the only components.

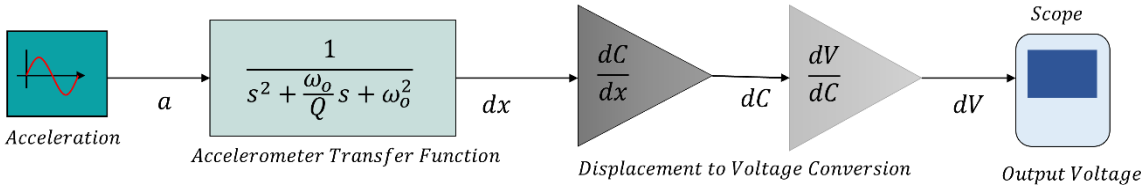

Figure 3.6 Simulink block diagram of the accelerometer

Figure 3.6 shows a Simulink model of the open-loop accelerometer. The detailed modelling of accelerometers is discussed in **Chapter 2**. The quality factor and the system's natural frequency are design parameters for the accelerometer's transfer function. The next block for system modelling is the displacement to capacitance transformation, a nonlinear process. However, it can be assumed linear for the small displacement as discussed above. Recalling from equation 3.7, the sensitivity of the device can be expressed as

$$\frac{dc}{dx} = \frac{2\epsilon A_t}{d_o^2}; for\ x \ll d \qquad 3.8$$

It shows that the device's sensitivity is constant for small displacement and can be calculated from the device parameter. In the simulation, it can be represented as a constant gain factor.

The next step in the open-loop modelling process is the capacitance to voltage conversion. As mentioned in chapter 2, subsection 2.4, this block primarily consists of a trans-impedance amplifier and some signal processing circuitry that can be captured as a constant gain for the simulation. The gain is adjusted to produce a voltage output of 1V for 1g acceleration, which implies the sensitivity of the accelerometer is set to $1\ V/g$.

The system is excited for different input types, including step and sinusoidal, to examine the system's behavior in the time domain. A step input of 1 m/s^2 is applied to the system. Figure 3.7 shows the output response of the system for different Q values. It is apparent that when the system's quality factor rises, the settling time and ringing in the system increases as well. The system takes roughly 10 ms to settle down for Q of 20, but nearly 200 ms for Q of 200.

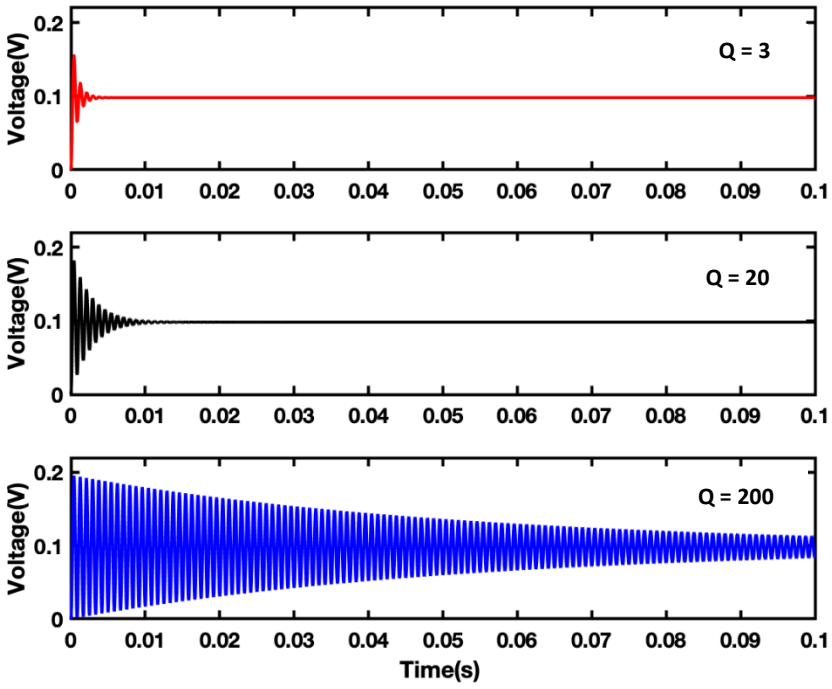

Figure 3.7 Simulated output response of the ISL accelerometer for 1 m/s^2 step input for different Q values

To examine the AC performance of the sensor, a 300 Hz sinusoidal acceleration of 10 ms^{-2} is applied to the system with a Q of 50. Figure 3.9 depicts the system's output response, which shows a 1V output that stands for 0.17 m mechanical displacement. For the same magnitude of acceleration but at the resonance frequency (1200 Hz), the system shows 50V at the output, as illustrated in Figure 3.10. This output voltage corresponds to a displacement of 8.5 μm, which is greater than the sensor element gap.

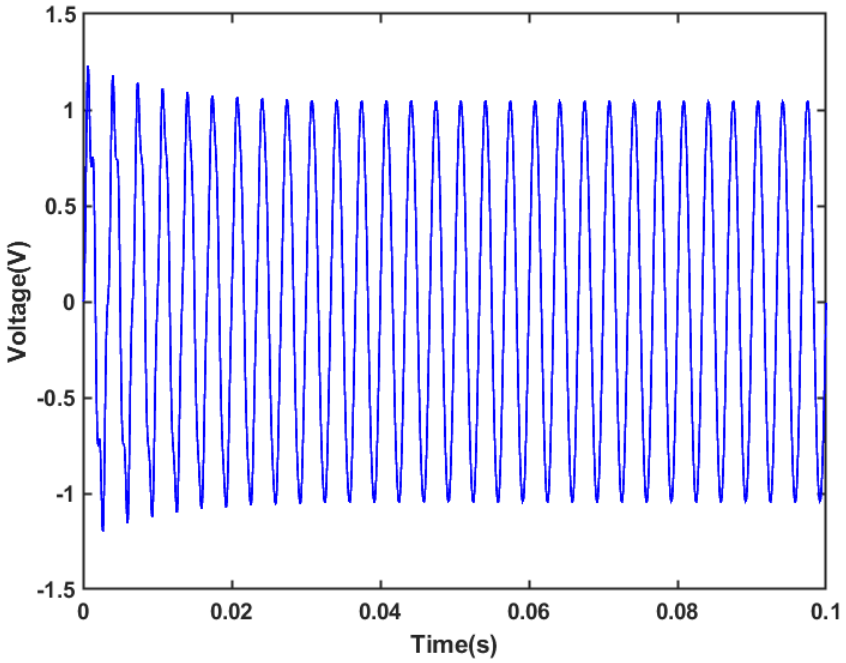

Figure 3.8 Simulated transient response of the ISL accelerometer (Q of 50) for 300 Hz sinusoidal excitation frequency

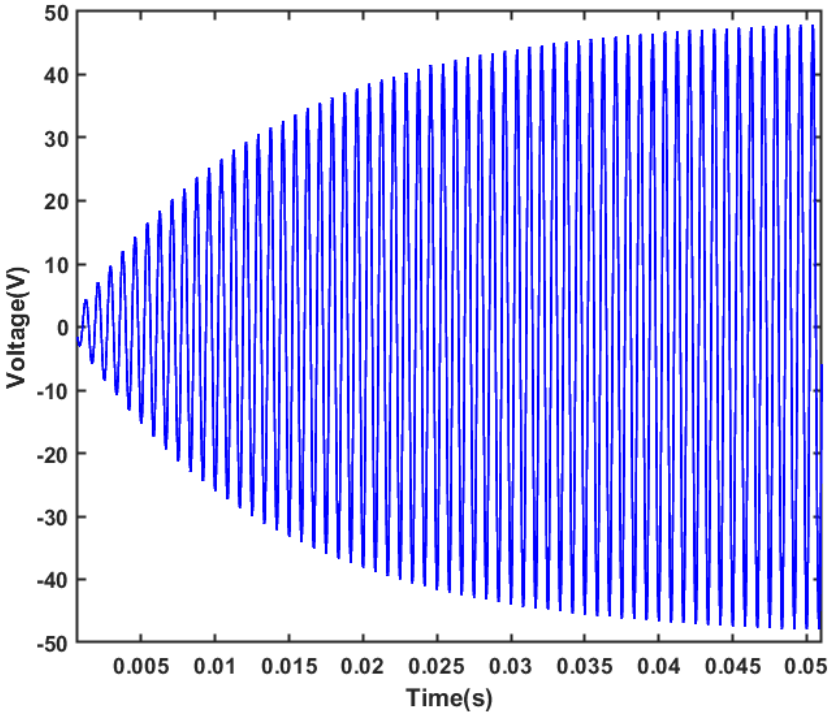

Figure 3.9 Simulated transient response of the ISL accelerometer (Q of 50) for 1200 Hz (at resonance) sinusoidal excitation frequency

From another angle, the system would behave as if it were subjected to a 50g acceleration. This signal amplification depends on the system's quality factor, which is about Q times larger than its static displacement. Thus, a large excitation signal at resonance frequency would cause the system to collapse at resonance.

A bode plot of the proposed sensor is drawn to accurately predict the sensor's behavior across all the frequencies up to its bandwidth. The sensor response is constant up to the point of resonance, as shown in Figure 3.8. and the quality factor increases the output response at resonance. Furthermore, at resonance, the phase change becomes steeper, and the phase margin decrease from infinity (Q= 3) to around 2.7 (Q = 200).

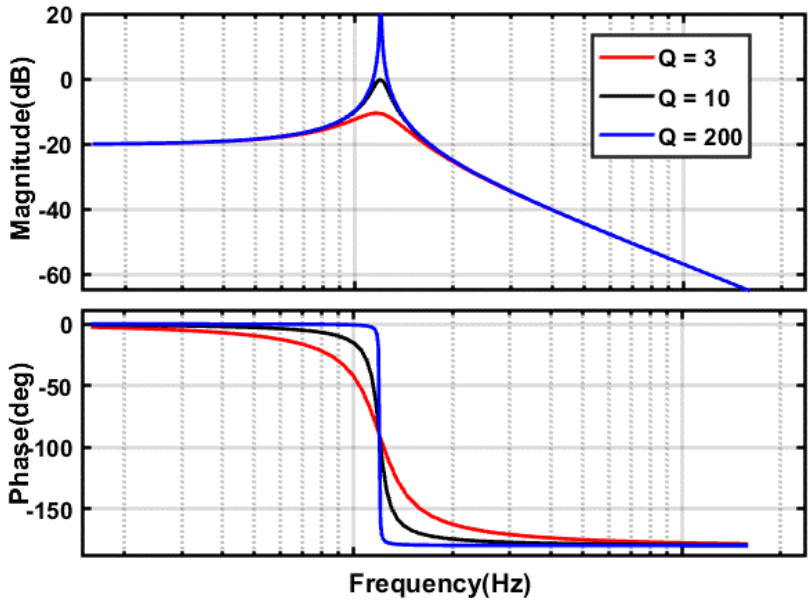

Figure 3.10 Frequency response of the ISL accelerometer at different Q

In conclusion, a higher quality factor brings the system poles closer to the imaginary axis, resulting in more oscillatory behavior and magnitude amplification. Thus, exploiting the sensor in an open loop with high Q becomes challenging. The next chapter discusses the implementation of the closed-loop system to address all these issues.

Chapter 4. Closed-Loop System: Theory and Simulation

This chapter explains the principles and parametric derivation of the required building block equations to introduce the suggested closed-loop architecture design. Moreover, the principle of capacitive actuation and the differential force feedback approach used in the proposed system will also be thoroughly analyzed. Finally, the controller selection process and modifications used in the system are discussed in detail.

4.1. Fundamentals of Force Rebalancing

The basic idea in a closed-loop system is to establish an equal and opposite force to offset the displacement caused by the inertia force. This problem can be categorized as tracking or regulation from the control system design standpoint. In a tracking control problem, measured acceleration tracks the unknown acceleration applied to the system to maintain the reference point. Alternatively, external acceleration can be considered as disturbance in a regulation type control problem and is rejected by applying an electrostatic force in the opposite direction. Regardless of the control problem topology, the goal of a control system is to maintain the proof mass at rest despite an external acceleration. Figure 4.2 shows a block diagram of an active control system where the proof mass displacement information in the form of the sampled output voltage is fed back to the system again to form a closed-loop system. As discussed in chapter 2, the implementation of the closed-loop system can be analog or digital. ADC captures the analog signal in a digital topology and passes it through the digitally implemented controller. The controller weighs the incoming signal based on the actuator geometry and adds compensation for the lagging phase of the mechanical sensing element. A digital control signal from the controller is then fed back to the electrostatic actuator through DAC to generate an opposing feedback force. The most crucial aspect of force rebalancing configuration is to design an appropriate controller for the given actuator. The proposed system utilizes an

electrostatic actuator, which is nonlinear in nature and only produces attractive forces. To address the unidirectional nature of the actuator, a differential actuator arrangement is typically used. Furthermore, linearization of the actuator is required to design a linear compensator.

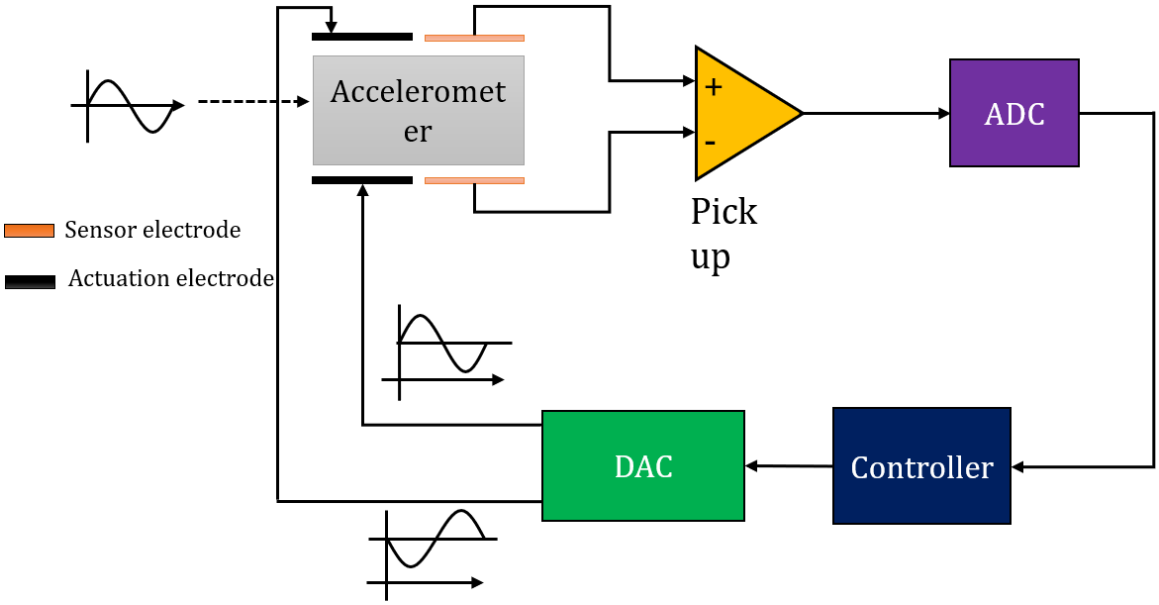

Figure 4.1 Force rebalancing topology of a MEMS accelerometer

4.2. Bidirectional Capacitive Actuator

A common technique to linearize the electrostatic actuator is to apply a DC bias. A fixed bias voltage combined with a differentially applied control signal on the two electrodes can make the actuator bidirectional, allowing it to counteract acceleration from both directions. Figure 4.2 shows such a configuration where proof mass is virtually grounded and a bias V_{Dc} is applied to both electrodes. At this point, the electrostatic force exerted on the proof mass is symmetric, equal, and opposite. Hence, the net force acting on the proof mass is zero in the absence of feedback voltage, implying that offset forces have no impact on proof mass. However, the amount of voltage on each electrode can be adjusted by varying the feedback voltage differentially. This would result in a force imbalance, with a non-zero force acting on the proof mass in a particular direction. Thus, bi-directional linearized electrostatic actuation is achieved.

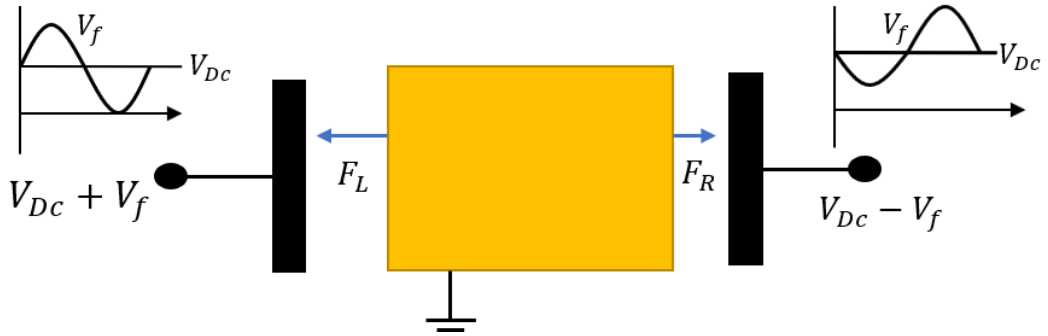

Figure 4.2 An illustration of differential capacitive actuation

Recalling the electrostatic force equation from Chapter 2, we can write

$$F_R = \frac{1}{2}\frac{dC_R}{dx}\left(V_{DC} - V_f\right)^2 \tag{4.1}$$

$$F_L = \frac{1}{2}\frac{dC_L}{dx}\left(V_{DC} + V_f\right)^2 \tag{4.2}$$

Assuming both electrodes have the same sensitivity $\left(\frac{dC_R}{dx} = \frac{dC_L}{dx}\right)$, the net electrostatic force applied on the proof mass is

$$F_{e,net} = F_L - F_R \tag{4.3}$$

$$F_{e,net} = \frac{1}{2}\frac{dC}{dx}\left[\left(V_{DC} + V_f\right)^2 - \left(V_{DC} - V_f\right)^2\right] \tag{4.4}$$

$$F_{e,net} = 2\frac{dC}{dx}V_{DC}V_f \tag{4.5}$$

This net electrostatic force is used to counteract the external force applied by an acceleration input *a*; thus force equilibrium expression can be written as follows

$$F_{a,ext} = F_{e,net} \tag{4.6}$$

$$ma = 2\frac{dC}{dx}V_{DC}V_f \tag{4.7}$$

$$\frac{V_f}{a} = \frac{m}{2\frac{dC}{dx}V_{DC}} = Constant \tag{4.8}$$

Equation 4.8 shows that all the parameters on the right-hand side are constant. It implies that the translation from feedback voltage to feedback acceleration is linear. The constant on the right side can be regarded as an actuator gain.

4.3. Simulation of the Closed-loop System

A system simulation is carried out based on the model constructed so far in Simulink. The closed-loop system model for the MEMS accelerometer is shown in Figure 4.3. During the simulation, a constant gain is entered for the parameters that can be calculated numerically directly from the model of each block. The closed-loop model of the accelerometer consists of four sub-blocks, namely, Accelerometer block, Capacitance to voltage conversion block, Compensator/Controller block and Voltage to force conversion block

- **Accelerometer model** is described in depth in Chapter 2. It is a second order transfer function that acts as an electromechanical low pass filter with two system parameters: quality factor (Q) and natural frequency (ω_n).
- **Capacitance to voltage conversion** is also discussed in Chapter 2, where it can be shown as a gain block. The electronic gains are adjusted to obtain a sensitivity of 1V/g for the system. Finally, in Chapter 3, the open-loop system is simulated using both an accelerometer and a capacitance to voltage block.
- **Voltage to feedback acceleration conversion** is discussed in the preceding section (section 4.1.1). A linearized block model shows that a simple gain can represent the actuator. The top and bottom electrodes are employed in the principal simulations for actuation, as discussed in Chapter 3. Table 3.1 shows the dimension of the electrode set. Using equation 4.8, the gain of the block is calculated.

- **Compensator block** will be discussed in the next section in detail. The compensator's objective is to generate a feedback signal to offset the inertia force and stabilize the system.

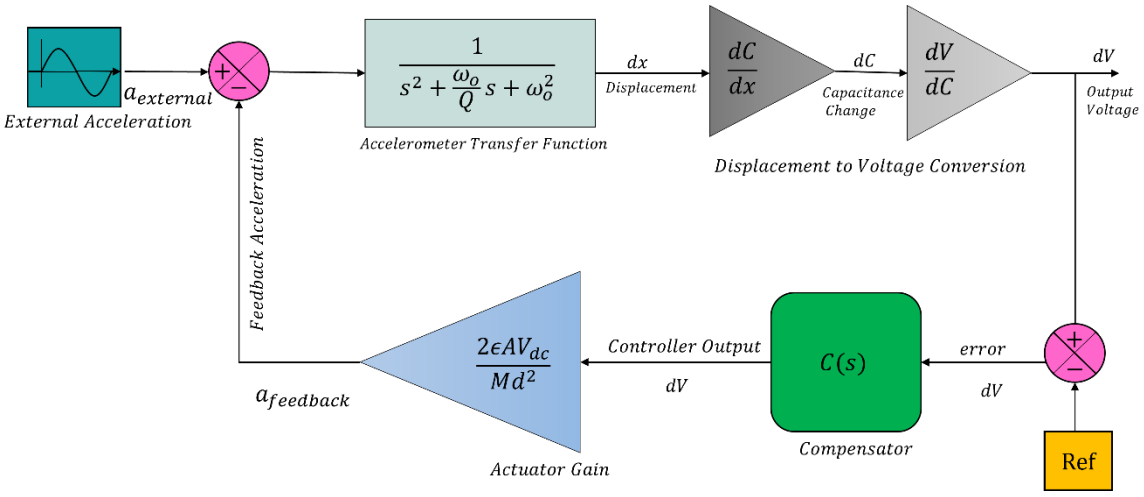

Figure 4.3 Block diagram of the closed-loop system modelled in simulink

This Simulink model will be used for further system development and controller design as will be discussed in the following sections.

4.4. Controller Objective

A controller is required to implement a stable closed-loop system for an underdamped MEMS accelerometer. The requirement for a compensator stem from the need to stabilize the system and suppress the large displacements at resonance. The mechanical sensing element at resonance exhibits a Q-times increase in displacement over its static displacement. Furthermore, around the resonance frequency, the mechanical element begins to lag in proportion to the input acceleration, resulting in a -90-phase shift. As the Quality factor increases, system poles move near the $j\omega$ axis, resulting in narrower -3db bandwidth with a steeper phase change. Hence, controller design becomes challenging. One of the fundamental requirements for the controller is to calculate the amount of voltage that must be applied to the electrode in order to generate an equivalent amount of force that can counteract the external inertial force imposed on the proof mass and compensate for the phase change at resonance. Researchers have used several controllers, including

PID, PI, PD, and sigma-delta modulators in both the analog and digital domains, primarily for restricting proof mass displacement at all frequencies. In this way, the external acceleration is measured through the feedback electrode. On the other hand, our control objective is to add damping exclusively around the resonance frequency.

A simple proportional controller can suppress proof mass displacement. However, increasing the proportional gain can introduce nonlinearity in the sensing element, leading to stability issues. Furthermore, a PI controller is impractical for the given control problem because it introduces infinite gain at DC. Thus, it would cause a steady-state error in tracking AC signals. A lead or lead-lag compensator is another plausible option for implementing a closed-loop system. To begin with, a PD controller is chosen to study the system. The controller can be expressed in the form of equation 4.9

$$C(s) = k_p + k_d s \tag{4.9}$$

where k_p, k_d are the controller constants.

The system of equations can be written as follows to include the controller:

$$m\ddot{x} + (b + k_d)\dot{x} + \left(k + k_p\right)x = ma \tag{4.10}$$

Equation 4.10 shows that the controller adds damping to the equation and alters the system property [36].

A simulation was run to study the system behaviour with the PD controller, as shown in Figure 4.3. Table 4.1 shows the necessary parameter for running the simulation. The ref point of the system is zero, which corresponds to the proof mass at rest. From Equation 4.5, it can be realized that the electrostatic actuator force is a combination of the DC bias voltage and AC feedback voltage, where a bias voltage is kept fixed and is set at 4V. The maximum value of the bias is restricted by practical

implementation and pull-in voltage limit. Furthermore, the feedback voltage is estimated by the controller.

Table 4.1 Simulation Parameters

Parameter	Value
Quality Factor	60
Bias Voltage (V_{DC})	4
Voltage to feedback acceleration gain (Top Electrode)	0.295
Voltage to feedback acceleration gain (Upper Electrodes set)	19

Figure 4.4 compares the system's frequency response with PD controllers and the open-loop configuration. It demonstrates that the PD controller shifted the system's resonance frequency to the right, which is undesirable.

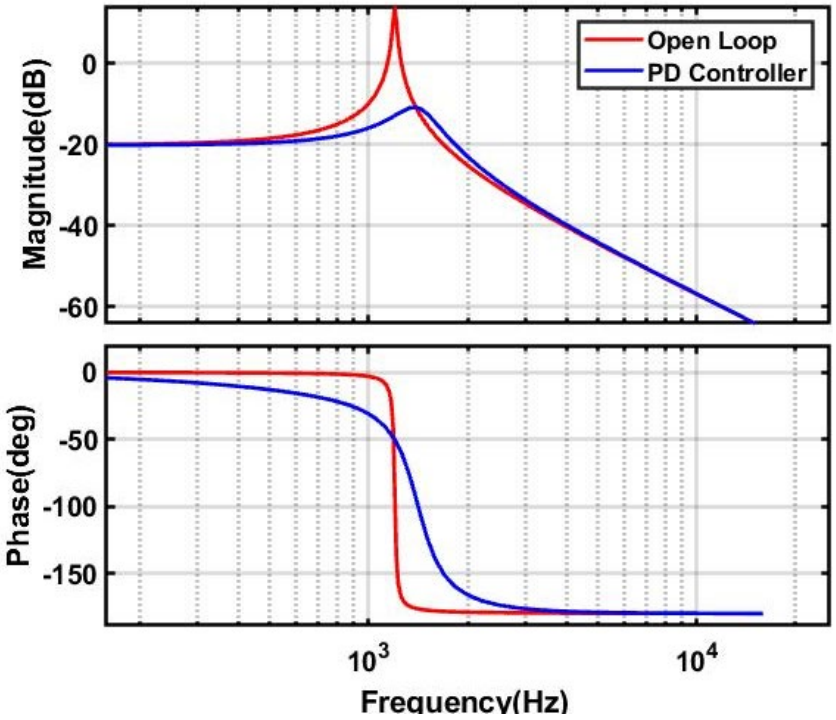

Figure 4.4 Bode plot of the closed-loop system with PD controller

Next, a PID controller was studied. The closed-loop simulation was run under similar conditions, and gains were tuned to achieve a stable system. A step input with a magnitude of 1 m/s^2 is applied in the system. In an open loop, the system would output approximately 0.1V as the accelerometer's sensitivity is set to 1V/g. The system outputs 60mV at the 28V demanded controller voltage cost with a controller

in the loop, as shown in Figure 4.5. Supplying the system with such a large feedback voltage is impractical.

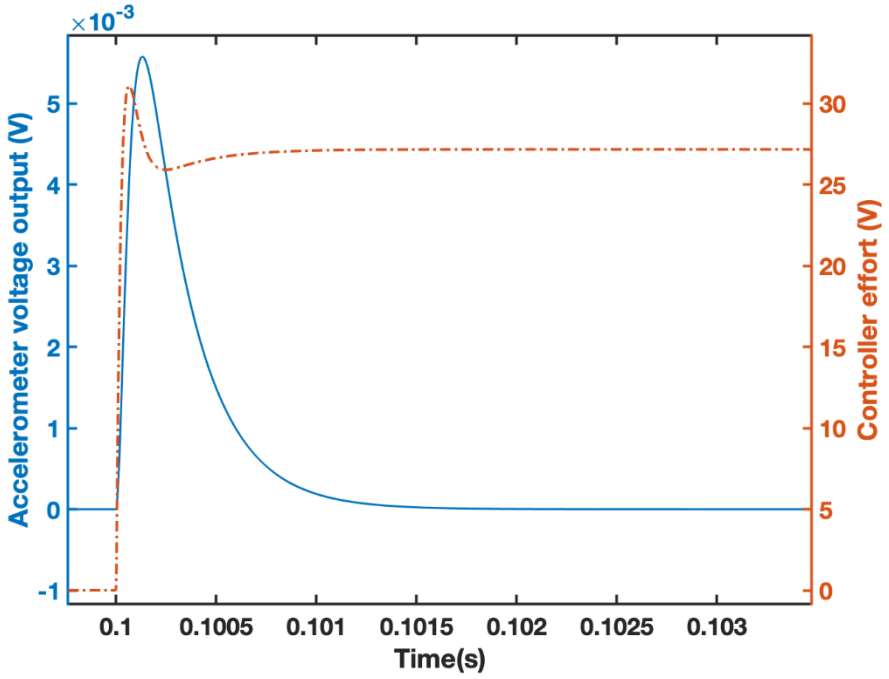

Figure 4.5 Step response of the closed-loop system with the PID controller for 1 m/s^2 step input

Another thing to note is that the controller adds electrostatic damping in other frequencies, introducing excess Brownian noise in the system. Again, this refutes the idea of maintaining a sensor in a vacuum to improve its quality factor and consequently improve performance.

The objective is to design a controller that dampens the resonance while maintaining the same open-loop characteristics up to its bandwidth. To put it another way, the controller transfer function needs to be designed in such a way that it provides extra gain to compensate for the large displacement around the resonance region while producing no output at other frequencies. Furthermore, the controller design must account for the uncertainties in the fabrication as well as the variation in the system's parameters such as quality factor and resonance frequency over time. To accommodate the changes in the system, the controller would either have to be adaptive or robust enough to handle the uncertainties.

Another critical consideration when designing the controller is the unmodeled dynamical system's out-of-band modes. Mechanical systems are continuous systems and governed by partial derivative equations. However, for the simplicity in controller design, the higher-order terms of the system are frequently ignored, resulting in a reduced-order model. Thus, while operating the system in a closed loop, the actuator force may excite the unmodeled dynamics of the mechanical part, causing other modes of vibration to excite and might create instability. This phenomenon is called the spillover effect. This effect should not affect the controller.

Finally, the high effort exerted by the actuator has been a cause of concern throughout the simulation. This is due to the extremely weak actuator placed by the design of the accelerometer. Thus, generating a feedback acceleration using the top and bottom electrodes would necessitate a high amount of voltage. The following section proposes a system architecture to handle this issue.

4.5. Switching Electrodes

Regardless of the type of controller, The accelerometer has a weak actuator (top and bottom electrode) located parallel to the proof mass to apply upward and downward forces as needed. On the other hand, the system's default sensing electrode comprises a large number of interdigital fingers. Operating the device in this configuration ensures maximum sensitivity. Compared to the top and bottom electrodes, sensing electrodes' capacitance is 60 times higher due to the large number of fingers and narrow gaps between the plates. Thus, the force generated by the sensing electrode would be 60 times larger than the designated actuation electrode. Therefore, one possibility is to use sensing electrode sets as actuators. However, this would result in a loss of sensitivity, affecting the device's performance.

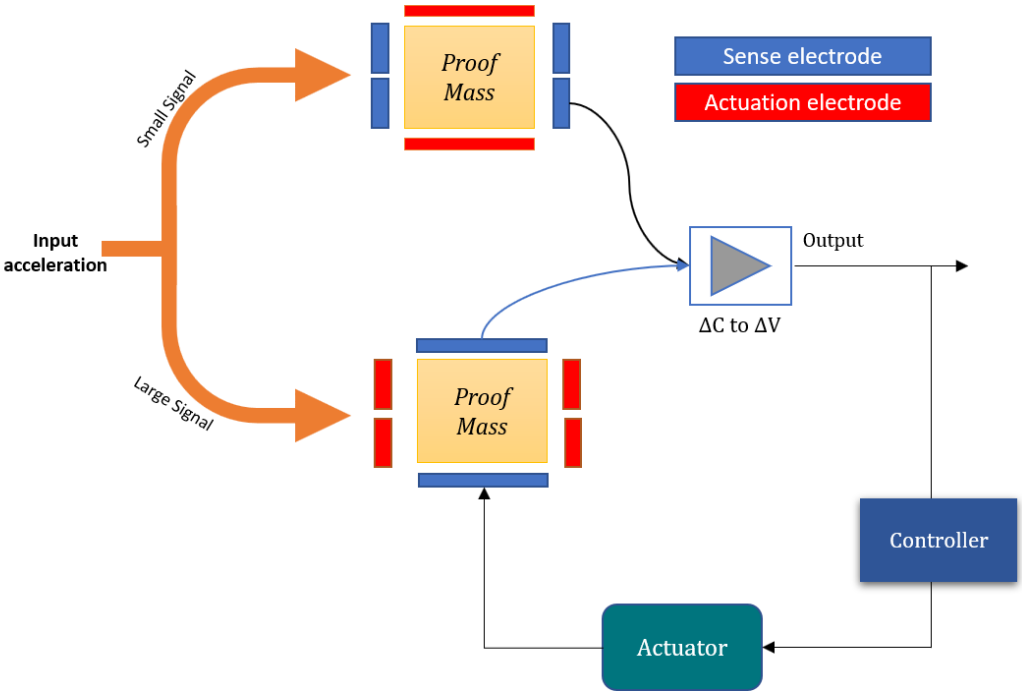

Figure 4.6 Proposed the actuator arrangement for the system

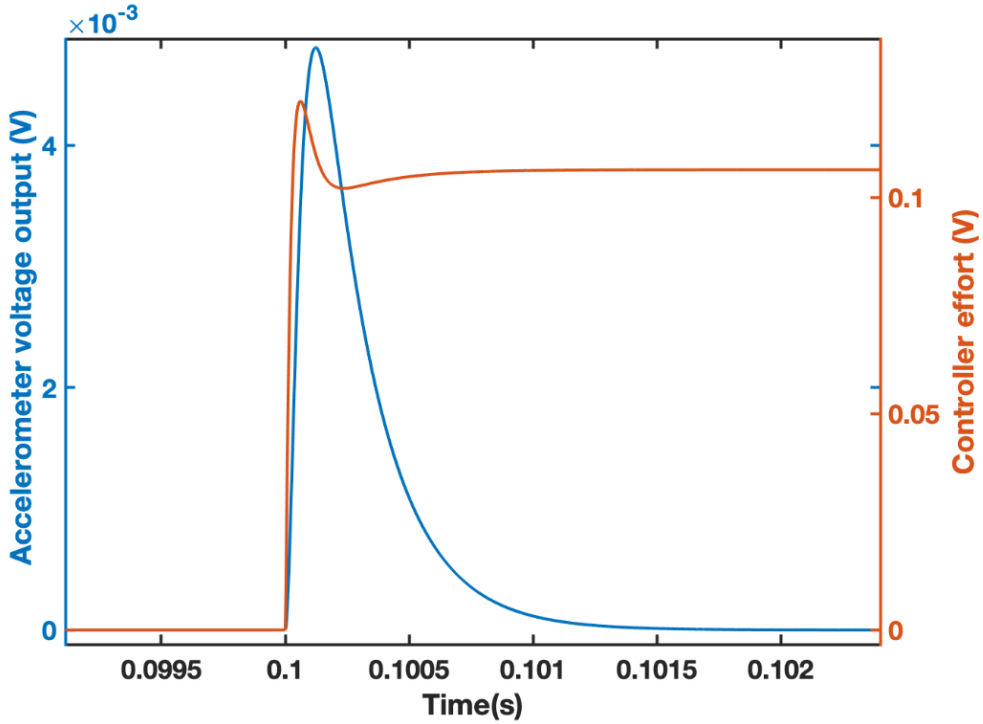

Figure 4.7 Step response of the closed-loop system with the PID controller using the sensing electrode as an actuator for 1 m/s^2 input

Another consideration is that, as previously stated, the controller does not have to operate at all frequencies except the resonance frequency. Thus, one configuration can be made to use the dedicated sensing electrode as an actuator for large signals, while the horizontal electrodes (top and bottom electrodes) can act as sensors. When a weak signal needs to be detected, the sensor can revert to its original configuration. The proposed scheme is illustrated in Figure 4.6. Consequently, switching electrode function in the system can reduce the actuator effort significantly. Figure 4.7 shows the simulation results using a PID controller and sensing electrodes as an actuator. According to the simulation results, the controller voltage drops from 27 V to 0.1V.

4.6. Controller Consideration

Velocity feedback can add a sufficient amount of damping to the system. Recalling from Equation 4.5, the net force from the electrostatic actuator can be expressed as

$$\Delta F = \beta V_f \qquad where\ \beta = \frac{2\epsilon A V_{DC}}{d^2} \tag{4.11}$$

where β is the electrostatic damping coefficient and V_f is the control voltage. Electrostatic damping can increase the overall damping of the system if the control voltage applied to the proof mass is proportional to the proof mass velocity. The system dynamic then can be written as

$$m\ddot{x} + (b + \beta)\dot{x} + kx = ma_{ext} \tag{4.12}$$

However, velocity feedback is impractical due to the differentiator implementation given the system's large bandwidth. Furthermore, control action would be active at all frequencies. Ideally, the damping effect of the controller should be limited to the frequencies around the resonance. This requires a different class of controllers.

A resonant controller, primarily used for vibration suppression in flexible structures, is the most common choice in the literature. Theoretically, it can provide infinite gain at a specific frequency. Thus, it has a better disturbance rejection property and can handle AC signal tracking well. Even the internal model principle prescribes that the controller should include the disturbance model [46], which implies poles of the controller should be near to the $j\omega$ axis at locations corresponding to the disturbance frequency [47].

Various types of resonant controllers are described in the literature, including positive position feedback (PPF) controller and negative derivative (NDF) controller. However, the fundamental concept underlying the resonant controller is to provide a damping effect on a specific vibrational mode by applying feedback force 90° out of phase with respect to the displacement. In the following subsections, both controllers are described with reference to our system implementation.

4.6.1. Positive Position Feedback Controller

In the 1980s, Caughey and Fanson developed a particular form of second order compensator, known as a positive position feedback controller. In this arrangement, the system's output displacement is positively fed back to the plant through the second order compensator. The transfer function of the controller can be given by [48], [49]

$$C(s) = \frac{\eta(s)}{X(s)} = k\frac{\omega^2}{s^2 + \frac{\omega_c}{Q_c}s + \omega_c^2} \tag{4.13}$$

where $\eta(s)$ is the output from the controller, *X(s)* is the input to the controller, k is the controller gain, Q_c is the quality factor of the controller and ω_c is the frequency of the compensator.

The compensator's natural frequency is set to the system's resonance frequency. Hence, the two tunable parameters in the controller design remain the

quality factor and compensator gain. According to Equation 4.13, the controller is a second order low pass filter with a -90° phase shift at resonance. As the accelerometer operates on the same system dynamics as the controller, it also has a -90° phase shift. Thus, the combined phase shift in the loop becomes -180° at the output of the controller block, as shown in Figure 4.8. The cancelling effect is achieved by positively feeding this signal back into the system. PPF effectively reduces spillover at a higher frequency because of its roll-off property after the resonance. However, at low frequencies, the magnitude response increases, affecting sensor performance [50], [51].

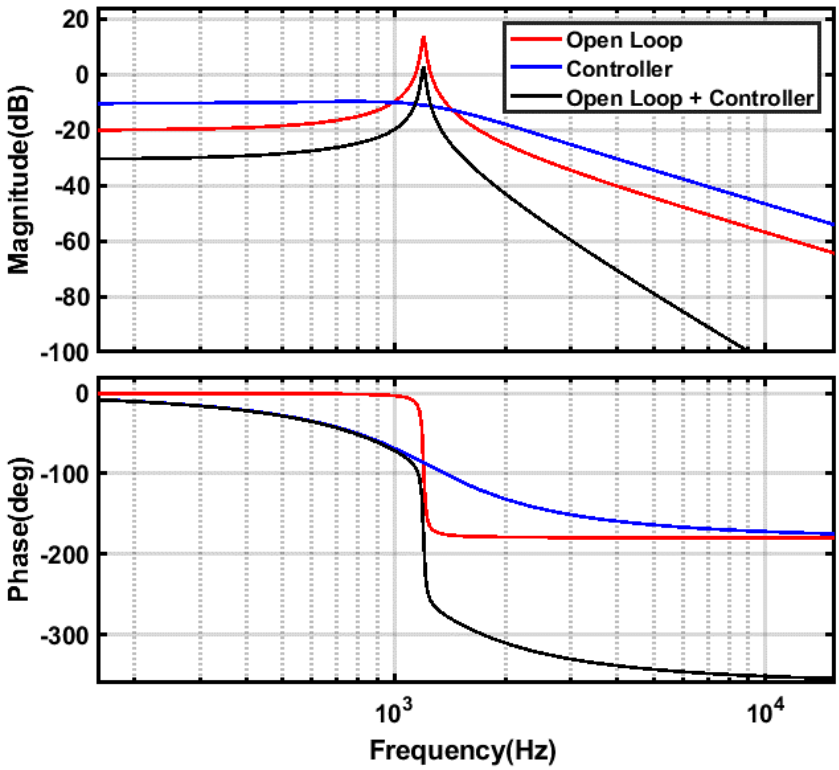

Figure 4.8 Frequency response of the PPF controller and control path

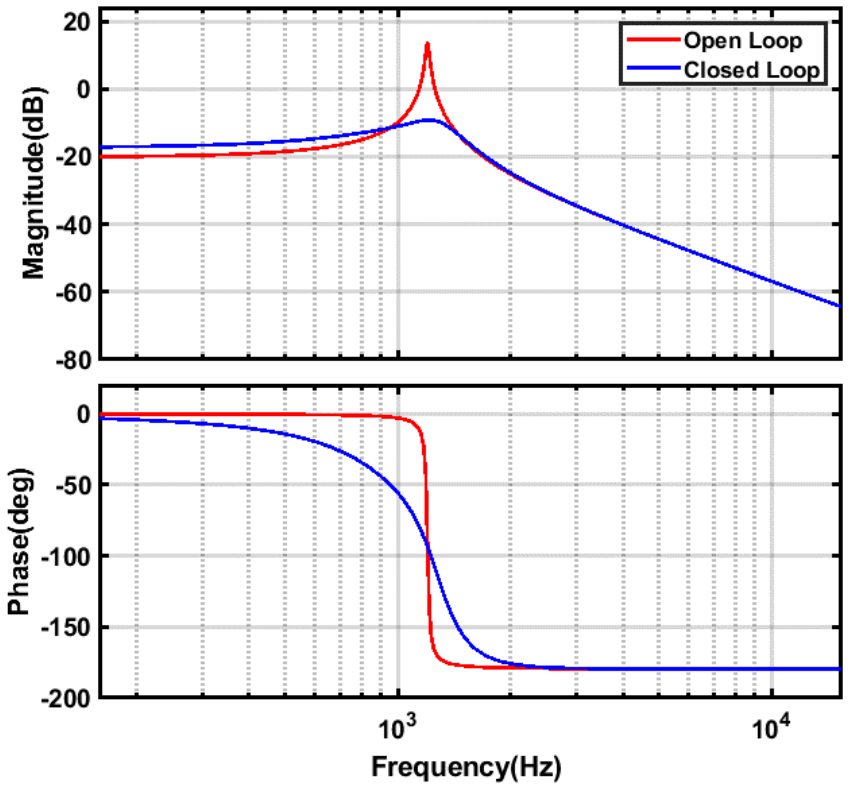

Figure 4.9 Frequency response of the open-loop system vs closed loop system with PPF controller

Figure 4.9 shows the closed-loop response of the ISL accelerometer with the PPF controller. The controller decreases the system's quality factor, which means it suppresses the large displacement but degrades the low-frequency sensitivity a bit.

4.6.2. Negative Derivative Controller

A negative derivative controller is another class of resonant controller where the velocity information of the plant is negatively fed back to the system through a second order compensator [48], [52]. A bandpass filter is used as a compensator in this control logic. The bandpass filter formulation reduces the chances of spillover at high frequencies while also limiting low-frequency response degradation [53], [54]. If the $\dot{\eta}(t)$ is the derivative of the controller output and x is the displacement of the structure, then controller can be implemented using a second order dynamical system as

$$\ddot{\eta}(t) + \frac{Q_c}{\omega_c}\dot{\eta}(t) + \omega_c^2\eta(t) = k\dot{x}\omega_c \tag{4.14}$$

where Q_c and ω_c are the quality factor and frequency of the compensator, respectively, and k is the controller gain.

The transfer function of the NDF can be written from equation 4.14 as

$$C(s) = \frac{\dot{\eta}(s)}{X(s)} = k\frac{\omega_c s}{s^2 + \frac{\omega_c}{Q_c}s + \omega_c^2} \tag{4.15}$$

Figure 4.10 shows that the controller has no phase change at resonance, causing the +90-degree path phase change in the control path. The output of the control block is fed back negatively into the system. Thus, it provides the cancelling effect on that specific frequency. Controller frequency is set to the disturbance frequency, and Q and k is the tuning factor. Theoretically, the Q value can be as high as possible. High Q values of the controller would provide a higher gain. However, from the standpoint of implementation, designing a higher quality factor-based filter would introduce truncation noise into the system. Thus, an optimal value of the quality factor is required to provide enough gain for the vibration suppression while minimizing truncation noise in the system. The only tunable parameter remains in the controller is the gain.

The frequency response of the closed loop system with the NDF controller and the Q of 50 open-loop system are compared in Figure 4.11. The controller quality factor is set to 6 in the simulation, and the frequency is set to the system's natural frequency. The result elucidated that the sharp peak of the open-loop resonance was reduced by 85% in the closed-loop

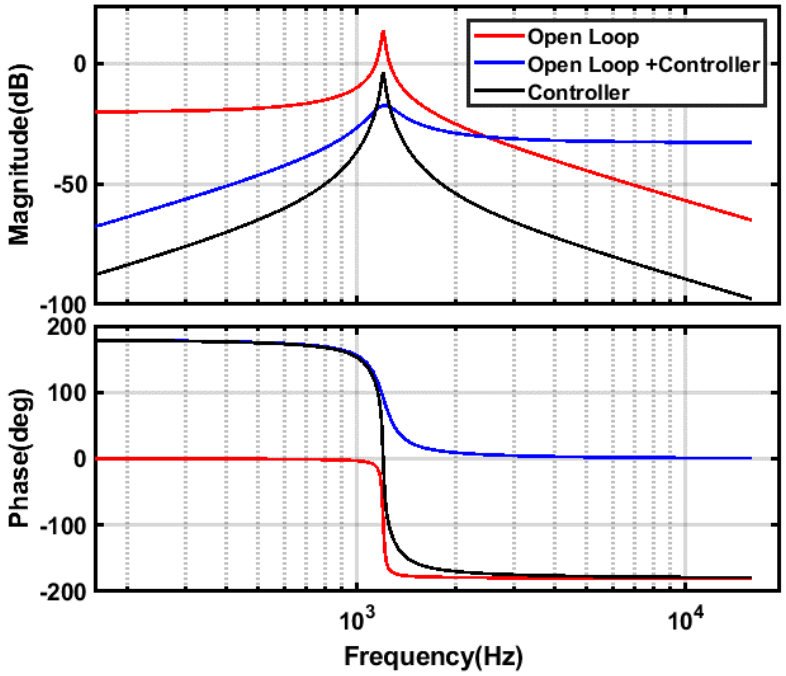

Figure 4.10 Frequency response of the NDF Controller and Control Path

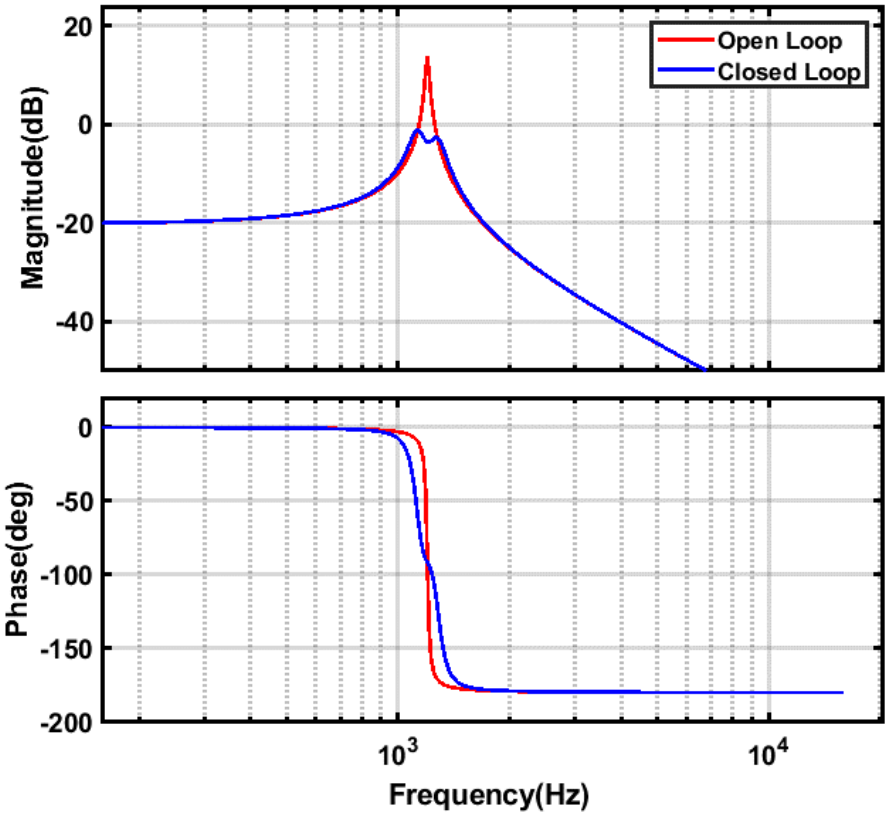

Figure 4.11 Frequency response of the closed loop system with the NDF controller

4.7. Proposed System Architecture

An electrode switching technique based on the signal strength is put in place to solve the actuator effort problem. Furthermore, a resonant type of controller is selected based on the control objective and requirement. However, there is still one more concern: the system's parameter variation. Accelerometers can be regarded as linear parameter varying systems. The system's quality factor can change over time because it is impacted by the vacuum level in the package. As the system degasses, the damping of the system increases.

Similarly, the system's resonance frequency may change as a result of changes in spring lengths or other dimensional parameters caused by temperature variation in the environment. However, the proposed controller is not adaptive; it is robust enough to handle the quality factor variation. Even with that, natural frequency change might cause a problem as the controller exclusively adds extra gain to the natural frequency. If the natural frequency of the system shifts, the controller bandwidth window needs to be changed. The controller is composed of a bandpass filter, and the filter window can be adjusted if the system's resonance frequency is known. Thus, system identification is required to estimate the parameter variation of the system as well as initial parameters for controller design. Adequate tracking of parameter variations makes the designed resonant controller’s feedback dynamic. Therefore, incorporation of a resonant controller with system identification capabilities provides a robust and effective solution for the resonant suppression of an underdamped high Q accelerometer. Figure 4.12 shows the final proposed system architecture. A system identification technique developed by Charles Duruaku, an ISL member, is used for the open-Loop system parameter estimation. Finally, the proposed controller and system architecture will be put into action in the following chapters.

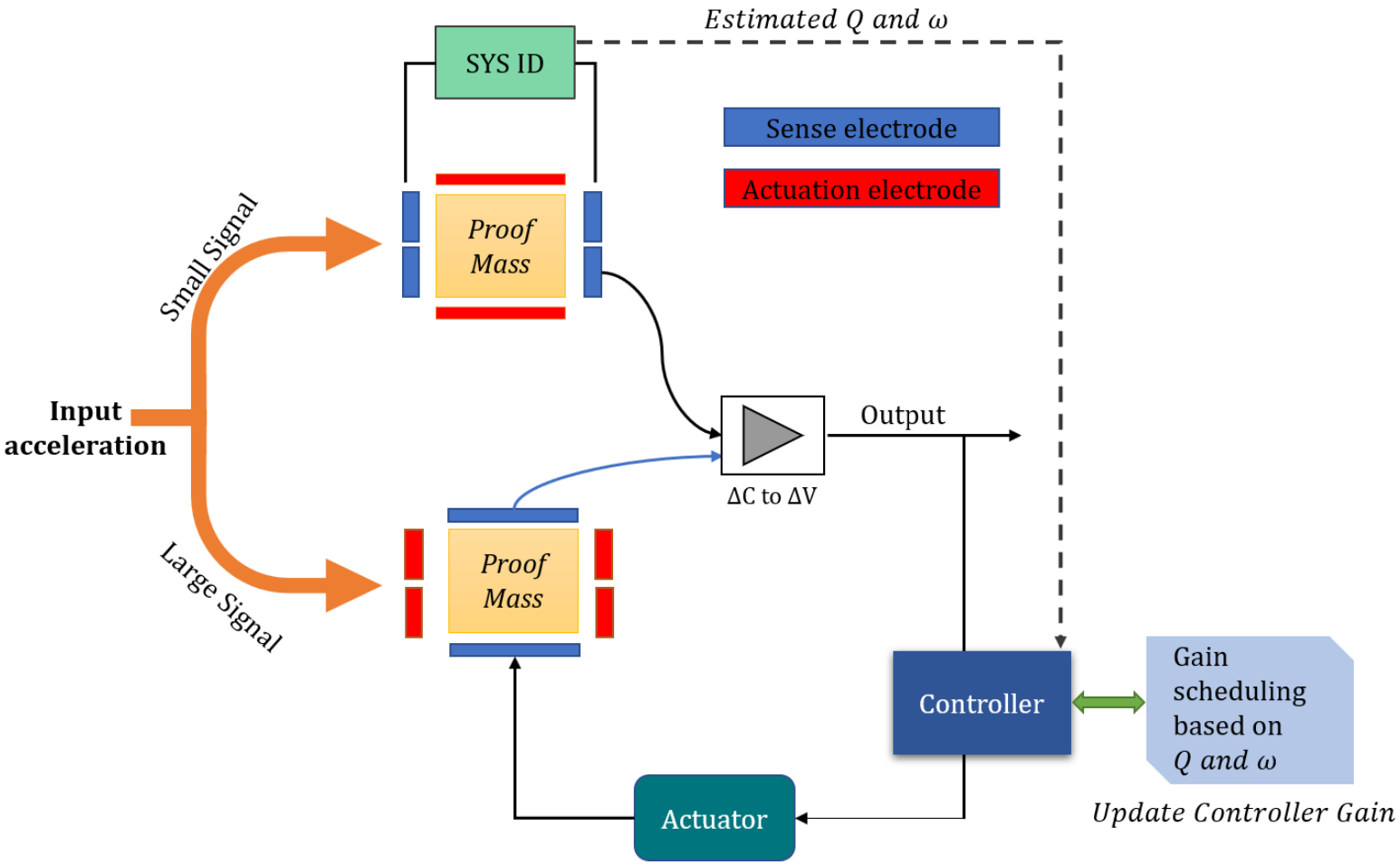

Figure 4.12 Proposed system architecture of the ISL accelerometer

Chapter 5.
Functional Characterization

This chapter discusses the characterization of the accelerometer system in an open-loop configuration. The subsequent sections also analyze experimental considerations, challenges, and test results.

5.1. System Configuration

For adequate performance evaluation and testing, the ISL accelerometer is required to interact with the physical world employing an electronic circuit. This interaction can be either in open-loop or closed-loop configuration. Employed configuration modes are discussed in the following subsections.

5.1.1. Accelerometer Pin Diagram

As previously stated, the accelerometer is packaged in a leadless ceramic chip carrier with 44 pins. Table 5.1 describes the function of the accelerometer pins used for the connection. Pin_3, Pin_5, Pin_21, and Pin_25 are connected with the accelerometer's four anchors, respectively, as shown in Figure 5.1.

Table 5.1 Acceleroemter pacakage Pin function

Pin	Description
Pin_41	Upper Left Electrode
Pin_5	Upper Right Electrode
Pin_27	Lower Left Electrode
Pin_19	Lower Right Electrode
Pin_1	Top electrode
Pin_23	Bottom Electrode
Pin_3,5,21,25	Anchors

Pin_41 and Pin_5 are connected to electrodes on the accelerometer's upper side. Similarly, Pin_27 and Pin_19 are coupled to the lower side electrode. Finally, Pin_1 and Pin_23 connect the top and bottom electrodes, respectively.

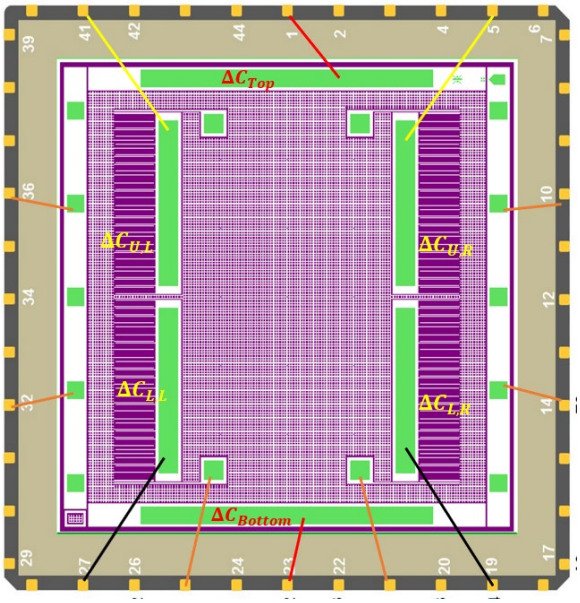

Figure 5.1 Pin diagram of the accelerometer package

5.1.2. Interface Electronics

An interface electronics converts the mechanical displacement of capacitive accelerometers to physical quantities like voltage, current etc. For this purpose, a general-purpose high-resolution, low noise capacitive readout CMOS IC called MS3110 was used in this thesis [55]. The MS3110 IC uses synchronous demodulation to read capacitance change, with the ability to operate in either differential or single-ended mode through an onboard dummy capacitor.

The readout IC contains an internal programmable capacitor array for bridge compensation, a trans-impedance amplifier, a S/H circuit, and a low-pass filter to output a voltage proportional to capacitance change down to as low as 4 $aF/\sqrt{Hz}$. This chip can work either in single-ended operational mode or differential mode with an ability to implement quasi differential operation through onboard dummy capacitance, all with a 5V DC supply with some decoupling components. Although the overall power consumption of the chip is 15mW, it also provides 2.25V DC output for easy ADC integration. This chip can also be programmed to set up capacitance to voltage gain and an operational bandwidth of 8 kHz. Hence, the output sensitivity (V/g) of the accelerometer can be programmed based on the requirement, whereas

capacitance change for an applied acceleration is fixed. Figure 5.2 shows a schematic of an MS3110 circuit.

The voltage output from MS3110 can be represented by equation 5.1

$$Output\ Voltage, V_o = \frac{Gain \times 2.656 \times (C_{T2} - C_{T1})}{C_F} + V_{Ref} \qquad 5.1$$

where V_{Ref} is bias voltage. Based on the datasheet, for the differential operation mode V_{Ref} is 2.25V.

Gain can be set to $2/4$ by programming.

C_T is the compensation capacitance, where $C_1 = 0\ to\ 9.79pF$ and

$C_2 = 0\ to\ 1.197pF$

$C_F$is feedback capacitance, rages from 0 to 19.44 pF

Here, the differential operational mode is utilized for testing purposes with readout gain set to 1V for applied acceleration of 1 g with an operation bandwidth up to 2kHz. A 24-bit delta-sigma ADC (ADS131A04) from Texas instrument is integrated with the MS3110 on PCB to sample the analog signal from MS3110 at a 10 kHz rate.

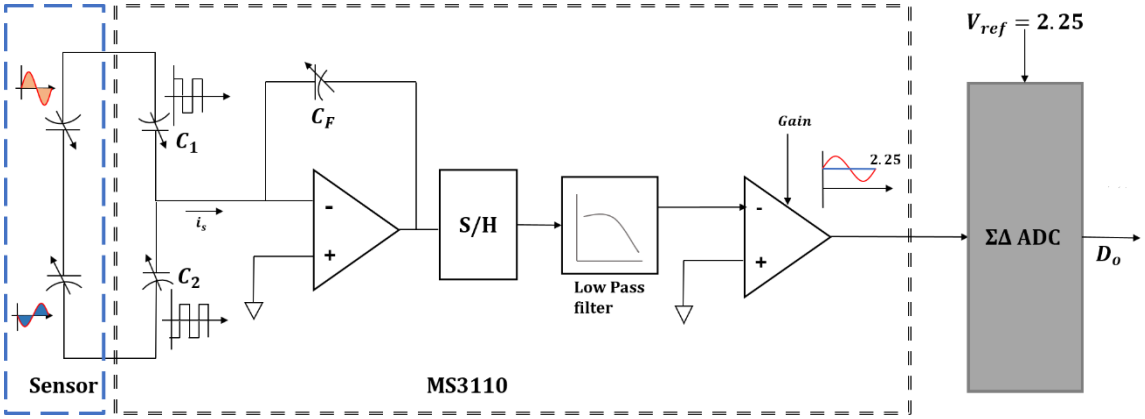

Figure 5.2 Schematic of the MS3110 chip

5.1.3. Characterization Test Setup

For testing purposes, the packaged sensor is mounted on a double layer stacked PCB board together with electronic readout circuitry for capacitance to voltage conversion

Input power supply to the system is 5V. Other essential components in the PCB layout include a 24-bit ΣΔ ADC (ADS131A04) from Texas instrument, 12-bit DAC (MAX532) and a 32-bit microcontroller (PIC32MX250F128B). Serial peripheral interface (SPI) is used as the primary communication protocol between the MCU, the ADC and DAC. Figure 5.3 shows a picture of the fabricated double layer PCB. The PCB was designed and assembled by Charles Duruaku, an Intelligent sensing laboratory team member. This compact PCB is the final prototype for testing open loop and closed-loop operation in the accelerometer. The assembled compact system was then placed in a vacuum chamber for damping level control, as shown in Figure 5.3.

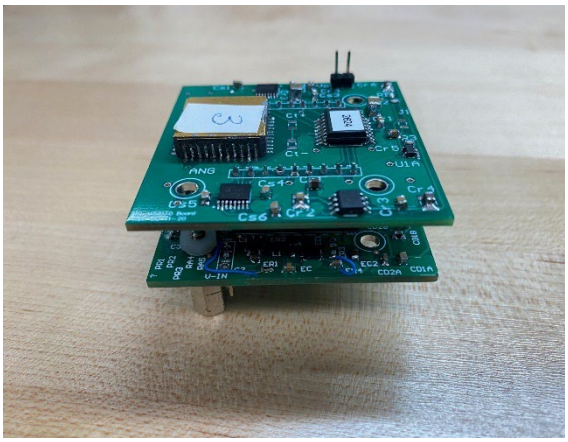

Figure 5.3 Double layer PCB board for testing

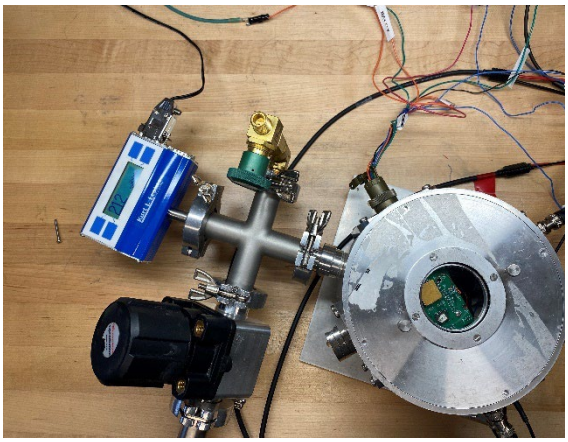

Figure 5.4 Vaccum chamber arrangment

5.2. Open Loop Characterization

The first step in evaluating the performance of the fabricated device is to measure the accelerometer's sensitivity, which is the output voltage change per unit of applied accelerometer at a given temperature measured in V/g. This is done by

assessing the response of the fabricated MEMS device for corresponding DC and AC signals.

5.2.1. DC Sensitivity

The accelerometer was coupled to an RLC meter at 100 kHz to perform the DC sensitivity test. ±1g of acceleration was applied by rotating the setup ±90° in the upward and downward direction. Table 5.5 shows the theoretical and experimental values of the capacitance change due to 1g acceleration.

Figure 5.5 RLC meter test result

Parameters	Theoretical	Experimental
Sensitivity (fF/g)	500	412
Bulk Capacitance (pF)	18.93	22.65

The discrepancies between the theoretical and measured values are mainly because of imperfect fabrication processes such as under etch, over etch, etc. These issues could cause the sensor mechanical parameter change, which ultimately affects the sensor's performance [56]. Another reason could be the effect of unwanted capacitances that exist between the various parts of the electronic component due to their proximity to one another [57].

5.2.2. AC Sensitivity

AC Sensitivity and operational bandwidth of the accelerometer were measured using a setup shown in Figure 5.6. The test setup includes a 2004E mini shaker connected with a Spider 81B vibration controller and a piezoelectric reference accelerometer. This accelerometer is attached to the shaker and delivers feedback to the controller, resulting in a closed-loop system. A proper fixture, designed and fabricated by the ISL team members, is used to mount the test sensor on top of the shaker. The fixture design takes into account the resonance frequency of all the other components that are also far away from the sensor bandwidth region. An AC signal at 200 Hz with a magnitude of 250mg is applied to the test sensor to conduct the test. The analog output from the accelerometer is collected using the data acquisition

system of the Spider 81B. The capacitance to voltage gain was set by the MS3110 chip, which was programmed to 1V/g.

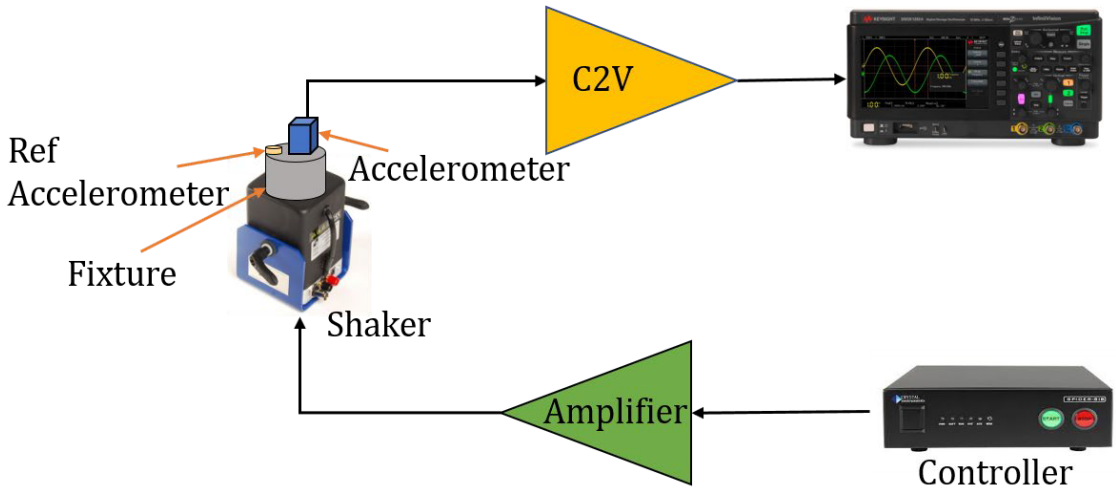

Figure 5.6 Test arrangement for dynamic testing of the sensor

Figure 5.7 Output of the for AC sensitivity of the accelerometer from Vibration controller data acquisition system

The test results are shown in Figure 5.7. Here, Ch 1 refers to the signal from the test accelerometer, which offers a good agreement with theoretically calculated sensitivity. Furthermore, following figure also shows the data for reference accelerometer output and drive signal coming out of the vibration controller.

Subsequently, the sensor's linearity is also recorded by varying the applied acceleration levels within the range of 200 mg to 2g. It is always expected to have a

linear response of a sensor within a specified range. For an accelerometer system, the lower range limit is constrained by the system's noise floor, and the upper limit depends on different factors such as pull-in, sensor material, etc. [14]. Figure 5.8 shows the output response of the sensor for different accelerations.

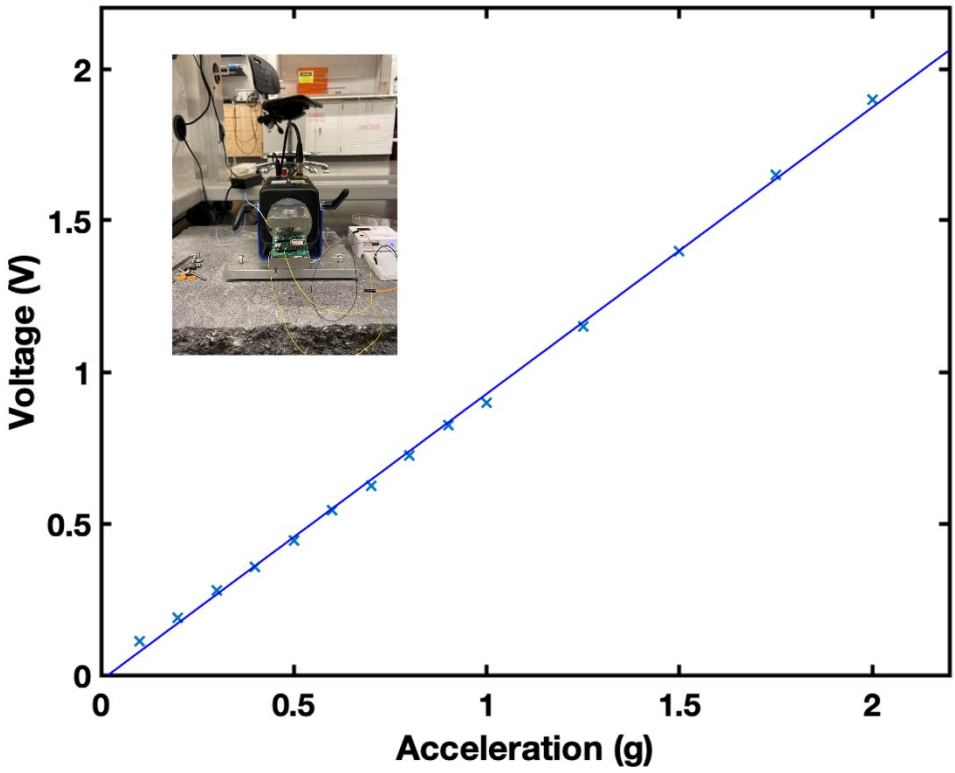

Figure 5.8 Linearity of the Accelerometer

By definition, linearity is expressed in terms of the percentage of nonlinearity and can be expressed using equation 5.2

$$Nonlinearity = \frac{Maximum\ Devation(g)}{Full\ Scale\ Output\ (g)} \times 100\% \qquad 5.2$$

Upon performing the test, the nonlinearity of the sensor was established as 0.1% within the range of applied acceleration.

5.2.3. Frequency Response Characteristics

Different testing arrangements can be adopted to assess the open-loop sensor response for various input types. However, the fundamental premise is to actuate the sensor in order to record the dynamic characterization in different vacuum pressure levels within the desired frequency range. Researchers have previously used electrostatic actuation [58] or mechanical excitation from a shaker for exciting an accelerometer [59]. Further, the desired quality factor is achieved by placing the device in a vacuum environment. Vacuum packaging is used at the production level to achieve a vacuum environment, but employing this introduces additional processing steps [60] and precludes pressure control within the package for testing purposes.

A vacuum chamber is another option for testing under vacuum where different vacuum pressures can be maintained for testing in various quality factors. It is a steel-made chamber along with a vacuum pump and a pressure gauge, as shown in Figure 5.9. In addition, the chamber has feedthrough connectors for connecting the circuit's electrical connection to the outside measurement equipment. However, it is impossible to install the mechanical shaker inside the vacuum chamber within this testing scope due to space constraints.

A resonant speaker [61], whose diaphragm resonates with the medium attached for signal transmission, is used to excite the system mechanically. A mount is fabricated that connects the sensor to the speaker, and a reference accelerometer is coupled beneath the mounting surface to calibrate the acceleration generated by the speaker. A signal generator feeds the appropriate signal through a power amplifier to the speaker. The amount of voltage applied through a signal generator, or the power amplifier gain can be adjusted to control the magnitude of the acceleration generated by the speaker.

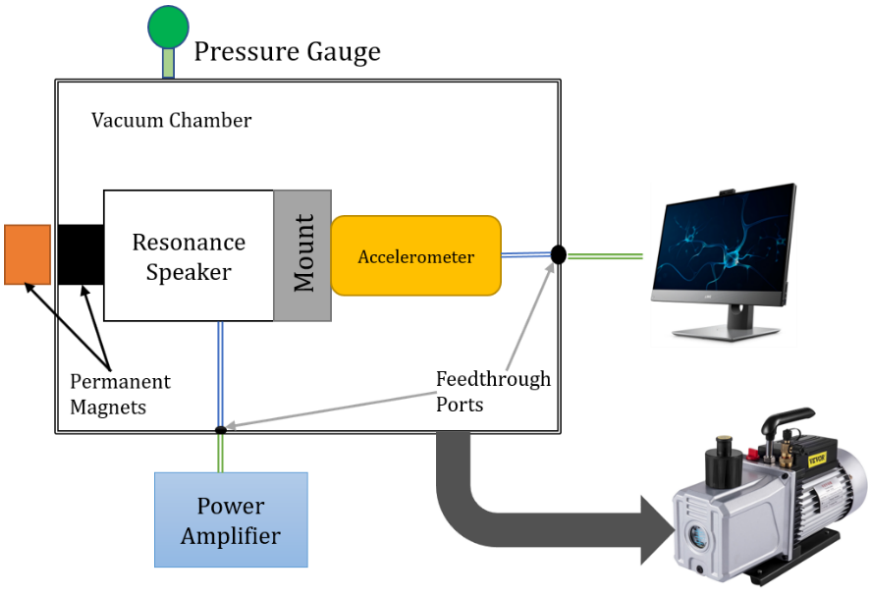

Figure 5.9 Set up for mechanical excitation using resonance speaker

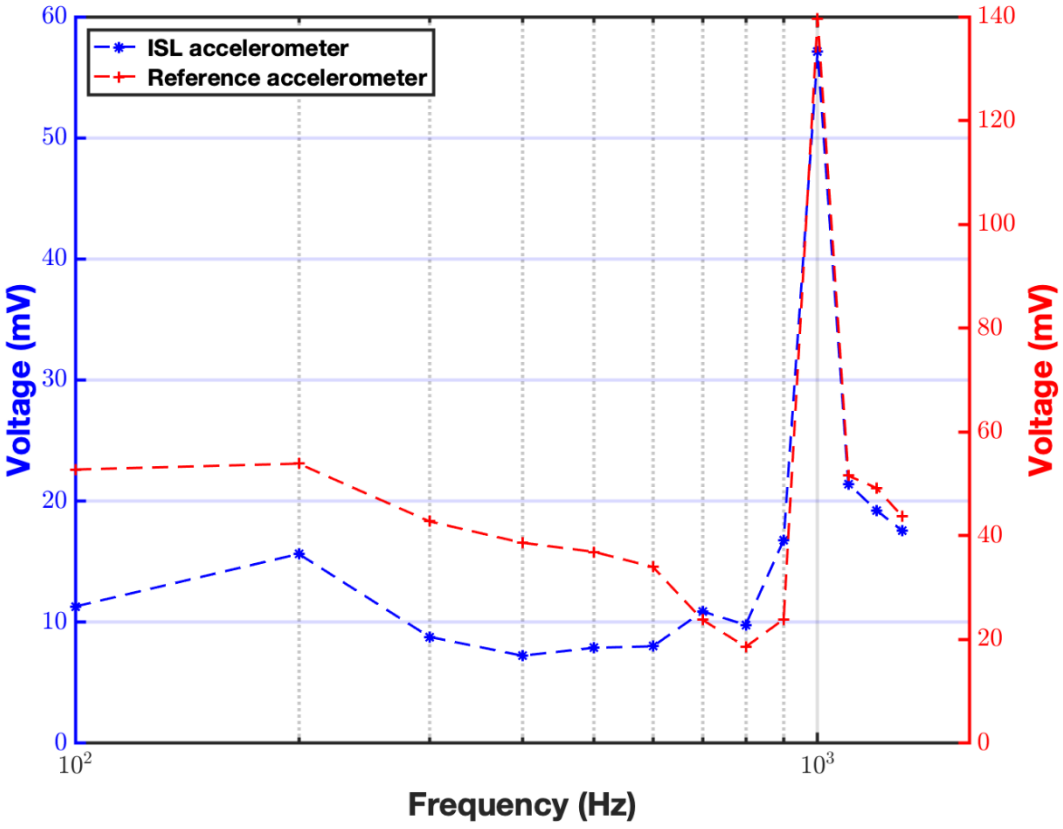

Figure 5.10 Frequency response of ISL accelerometer obtained by a mechanical excitation

Furthermore, speaker's small size allows it to be installed inside the vacuum chamber. The test setup is illustrated in Figure 5.9. The reference accelerometer used in this arrangement has a sensitivity of 150 mV/g. A 15-mV peak-to-peak sinusoidal voltage is applied to the power amplifier, which produced an acceleration of around 100 mg based on the reference accelerometer measurement, as shown in Figure 5.10. The result demonstrates a nearly linear response up to 1000 Hz. The accelerometer resonance frequency is anticipated to be around 1200 Hz by design, while the overall system showed a resonance peak at 1000 Hz. One explanation for this could be that the resonance of the PCB board or mount is dominant and falls within the accelerometer's operational bandwidth. Thus, this testing setup was deemed unsuitable for characterization.

Alternatively, electrostatic actuation was considered to actuate the proof mass. It also has the advantage of eliminating any undesired modal shapes from other mechanical elements attached to the PCB board. Finally, to test the device in open-loop mode, it is placed inside a vacuum chamber, which provides the benefit of controlling the pressure level and consequently testing the sensor for various quality factors. The test setup is depicted in Figure 5.11.

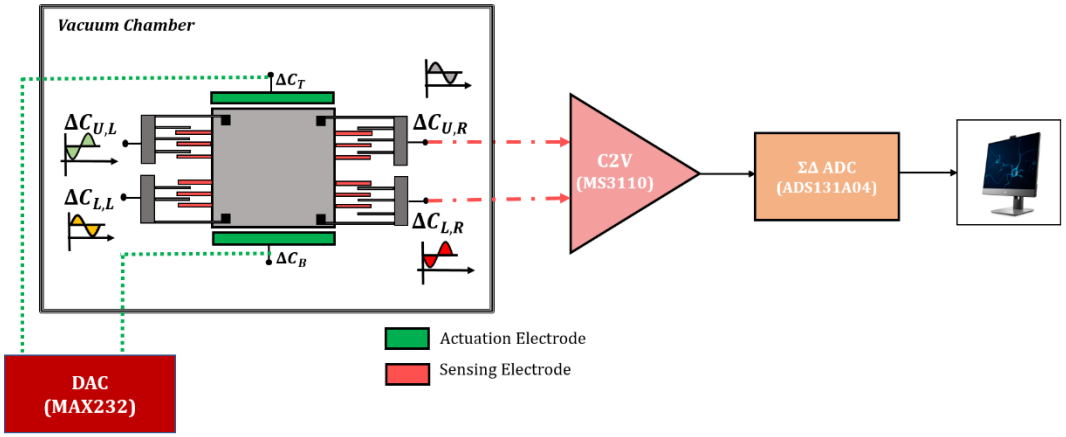

** $\Delta C_{X,Y}$ = *Total change in capacitance from one electrode set, where* X = *Upper/Lower* and Y = *Left/Right*

Figure 5.11 Open Loop testing arrangement by electrostatic actuation

Pin_41 ($\Delta C_{U,L}$) and Pin_27($\Delta C_L, L$) are used to electrostatically excite the proof mass by applying a differential biased AC voltage. A 12-bit two-channel DAC

generates a differential AC signal, causing the proof mass to accelerate linearly along its sensor axis, and the magnitude of the acceleration is estimated by Equation 5.3

$$a_{external} = \frac{2\epsilon A}{md^2} V_{Dc} V_{Ac} \qquad 5.3$$

Pin_5($\Delta C_{U,R}$), Pin_19($\Delta C_{L,R}$) are utilized as a sensor configuration. MS3110 converts the changes in capacitance values in the upper and lower electrodes to a voltage representing the applied external acceleration. The analog signal is eventually converted to a digital signal by the ADC, which then is collected via UART. For electrostatic frequency response testing, the sensor is excited within its operating bandwidth, at resonance and frequencies after resonance, with the same magnitude of electrostatically generated acceleration to capture the system's dynamical behaviour using the setup mentioned above. A 50 mV DC bias is applied to the electrodes ($\Delta C_{U,L}, \Delta C_L, L$) with 200 mV of differential AC signal with frequency varying from 50 Hz to 2000 Hz, and data is recorded through the terminal. Figure 5.12 shows the frequency response at different pressure for the arrangement. As pressure decreases, the amplitude at resonance increases, corresponding to theoretical understanding. Before the resonance frequency, the sensor exhibits a nearly linear response for all other frequencies. The system response drops by 20dB/decade after the resonance, as estimated by the 2nd order system behaviour.

5.2.4. Open Loop Q factor study

A study was conducted for an efficient controller design to ascertain the range of Q factors attainable with the available test environment. This was done by estimating the quality factor from the measured frequency response for various pressure levels. Figure 5.13 shows the extracted values at varying pressure levels; evidently, the plot sequence matches established theories and provides confines for controller design.

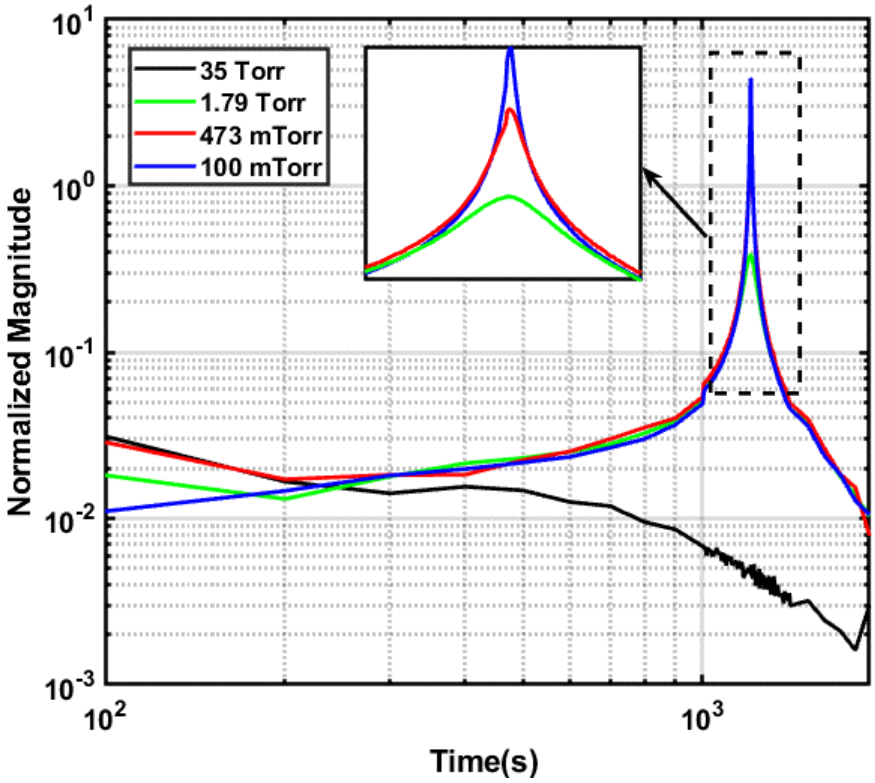

Figure 5.12 Frequency response of the open-loop accelerometer at different pressure levels

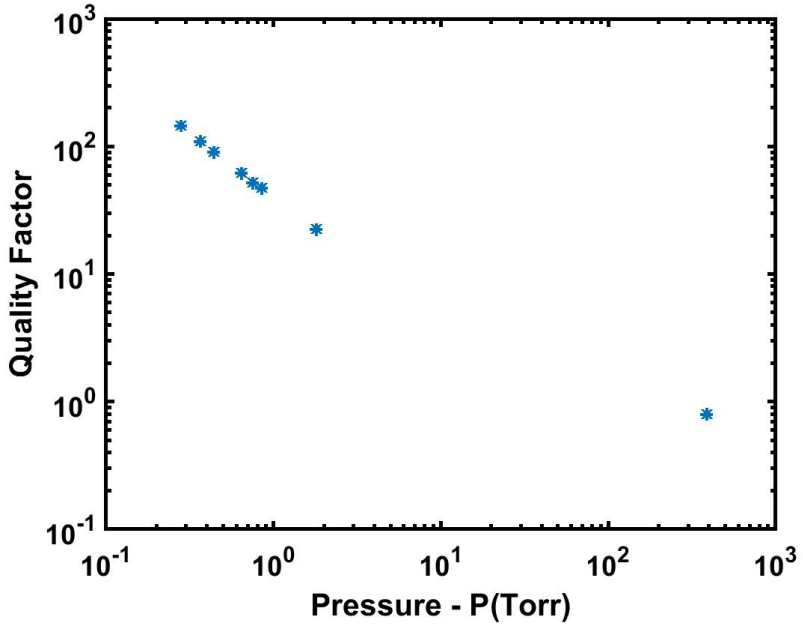

Figure 5.13 Quality factor vs. Pressure curve of the ISL accelerometer

5.2.5. Step Response

The sensor's time-domain response is recorded for a step input using the same setup. Figure 5.14 shows the results of a 7V impulse input applied to excitation ($\Delta C_T, \Delta C_B$) electrode of the sensor. As can be seen, the ringing and peak-to-peak amplitude of the system increases with the decrease in pressure level. Further, the settling time for 540 mTorr pressure level is recorded as 10 ms, while it rises to 15 ms for 141 mTorr pressure level

In conclusion, the data acquired from the system's frequency response and time response suggests that the proof mass displacement increases at resonance for AC signals and the oscillation rises for impulse signal. For that reason, a closed-loop system is required to suppress the resonance.

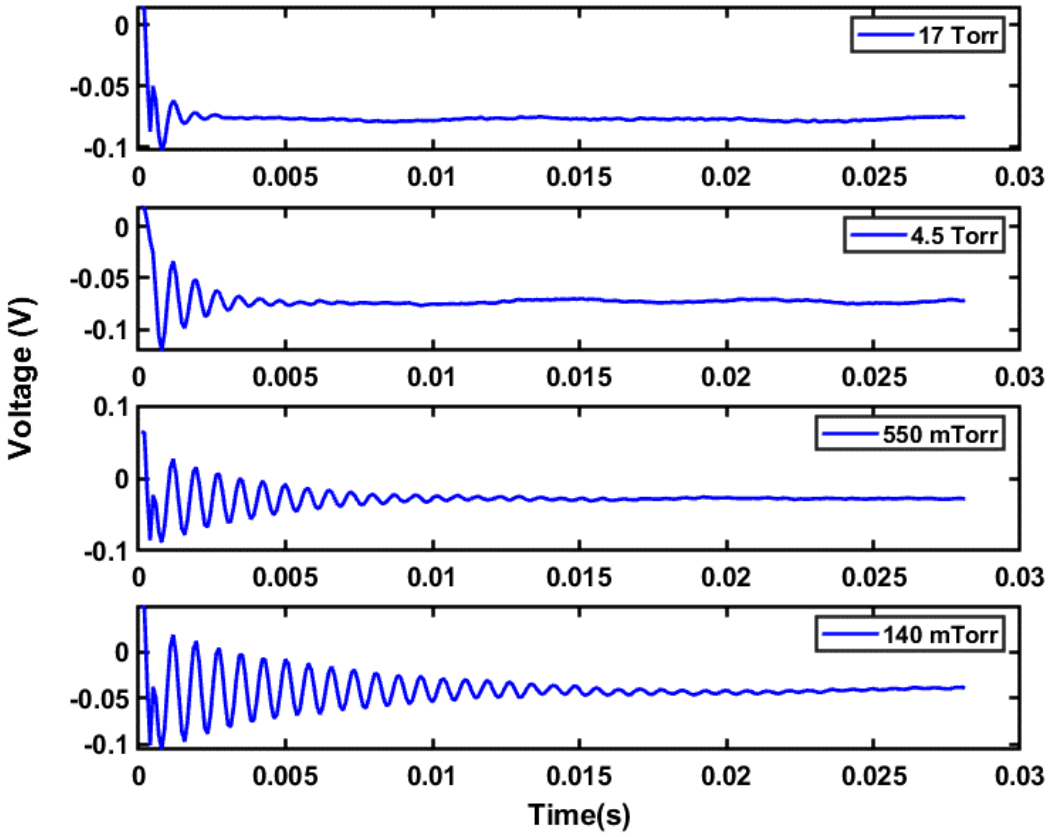

Figure 5.14 Step response of the open-loop system at different pressure levels

Chapter 6. Implementation and Results

In this chapter, discretization and implementation of the controller are presented. Further, it also discusses the closed loop testing arrangement and performance evaluation of the controllers.

6.1. Discretization of the Controller

The transfer function of continuous domain controller needs to be discretized for a digital domain implementation. The controller discussed in chapter 4 requires either a bandpass filter for the NDF controller or a low pass filter for PPF controller implementation in the digital domain. Discretization of both controllers follows the same process. Here, discretization of the negative derivative controller is discussed.

As discussed in Chapter 4, a negative derivative controller requires velocity as an input. Velocity can be computed by taking the derivate of the open-loop signal. For example, if the accelerometer's digital output at a given time instant is *X[n]*, then the time derivative of the signal can be expressed using equation 6.1.

$$V[n] = k_v(X[n] - X[n-1]) \tag{6.1}$$

where k_v is the gain value for finite-difference. It depends on the sampling time of the system. Negative derivative controller equation can be represented in the z domain by equation 6.2 [54]

$$C(z) = \frac{Y(z)}{V(z)} = k_f \frac{c_1(z^2+1)}{z^2 + a_1 z + b_2} = k_f \frac{c_1(1+z^{-2})}{1 + a_1 z^{-1} + b_1 z^{-2}} \tag{6.2}$$

where k_f is the controller gain. a_1, b_1, and c_1 are the filter coefficients.

Converting equation 6.2 to the time domain, it can be rewritten as

$$Y[n] = k_f c_1(V[n] - V[n-2]) - a_1 Y[n-1] - b_1 Y[n-2] \qquad 6.3$$

where *Y[n]* is the controller output in the digital domain.

The controller coefficients in equation 6.3 are determined by the natural frequency and the quality factor of the filter. As mentioned in Chapter 4, the filter frequency is usually tuned to the accelerometer's natural frequency. Hence, in response to the shift in the natural frequency of the accelerometer, the controller coefficient can be recomputed and updated in real-time.

The controller is implemented in fixed-point arithmetic on the PIC32MX250F128B microcontroller. The controller frequency is set to be the same as the ADC sampling frequency, which is 10 KHz. The filter coefficients are calculated using MATLAB IIR filter designer applet. The controller has only one tunable parameter. Therefore, the controller gain is tuned manually. However, an approximation of the gain is obtained from the system simulations in Simulink.

6.2. Test Setup for Closed-loop arrangement

Testing in a closed-loop system is more challenging than testing in an open-loop system. As discussed earlier, the system originally uses a set of four comb electrodes as a sensor and a set of horizontally placed (top and bottom) electrodes as an actuator. Since there is no need for actuation when operating in an open loop, the system is excited using the top and bottom electrodes during testing. On the other hand, testing a system in a closed loop configuration necessitates the use of another electrode to excite the system electrostatically in addition to the actuation electrode. That means the test setup would require three pairs of electrodes for three distinct purposes: sensing, actuation, and excitation. As discussed in Chapter 4, the system's top and bottom electrodes are weak and require a significant amount of actuator effort; therefore, these electrodes were used to actuate the system for testing purposes. However, the idea was to use the top and bottom electrodes as a sensor for large signals during the closed-loop operation. Therefore, the rest of the four comb

electrodes were divided into two differential groups. One differential pair is used for the sensor, while another pair is for actuation. Figure 6.1 showed such an arrangement. A separate DAC configuration applies a differential signal to the top and bottom electrodes to excite the system. During the testing, the whole system is kept under vacuum controlled chamber where the vacuum level is monitored and maintained by a pump and a unidirectional pressure valve.

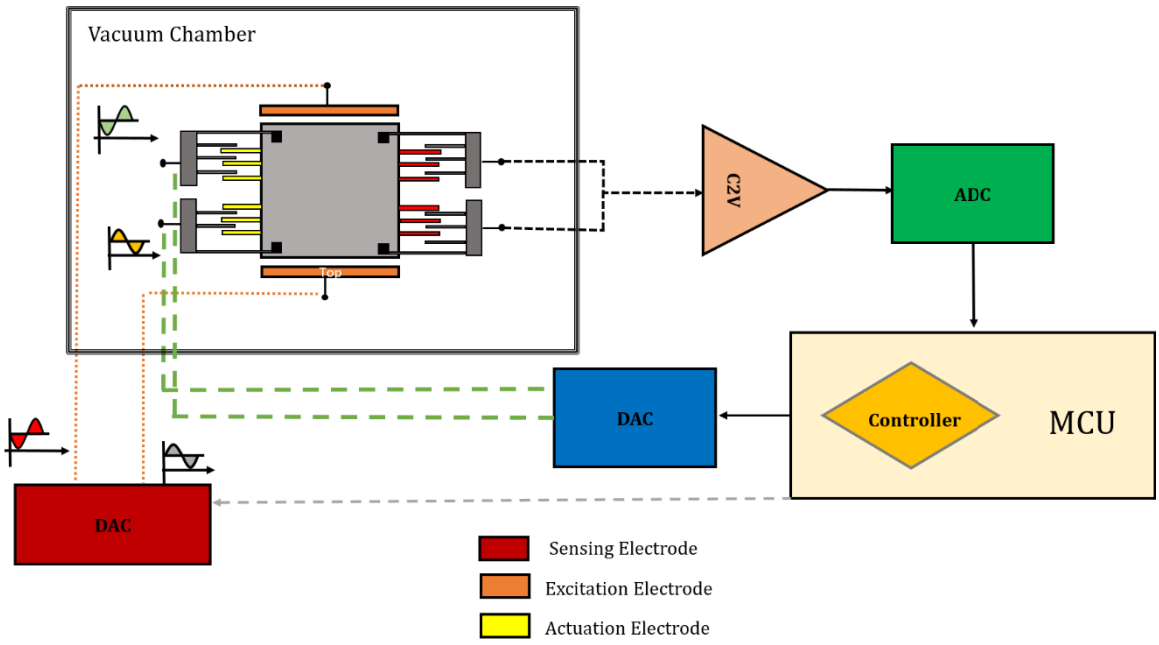

Figure 6.1 Sensor testing set up in the closed-loop configuration by electrostatic actuation

For frequency response analysis, a 200 mV AC signal biased by 50 mV is applied to the excitation electrodes set differentially for generating a sinusoidal disturbance in the system in the closed-loop configuration. The frequency of the excitation signal is swept from 50 Hz to 1500 Hz, and the output response is recorded. During the test, a constant vacuum level is maintained. Test results for various vacuum levels ranging from 80 mTorr to 16 Torr were collected. Similarly, the system's step response is measured by applying a constant 7V DC voltage for a short period of time. The performance of the discussed controller in Chapter 4 is presented in the following sections.

6.3. Positive position feedback controller performance

The test setup discussed in section 6.2 is utilized for testing the controller with different inputs. Figure 6.4 shows the step response of the open-loop (one on the left) and closed-loop system (on the right) with a positive position feedback controller. The reaction of the system is collected for different pressure ranges corresponding to various quality factor values.

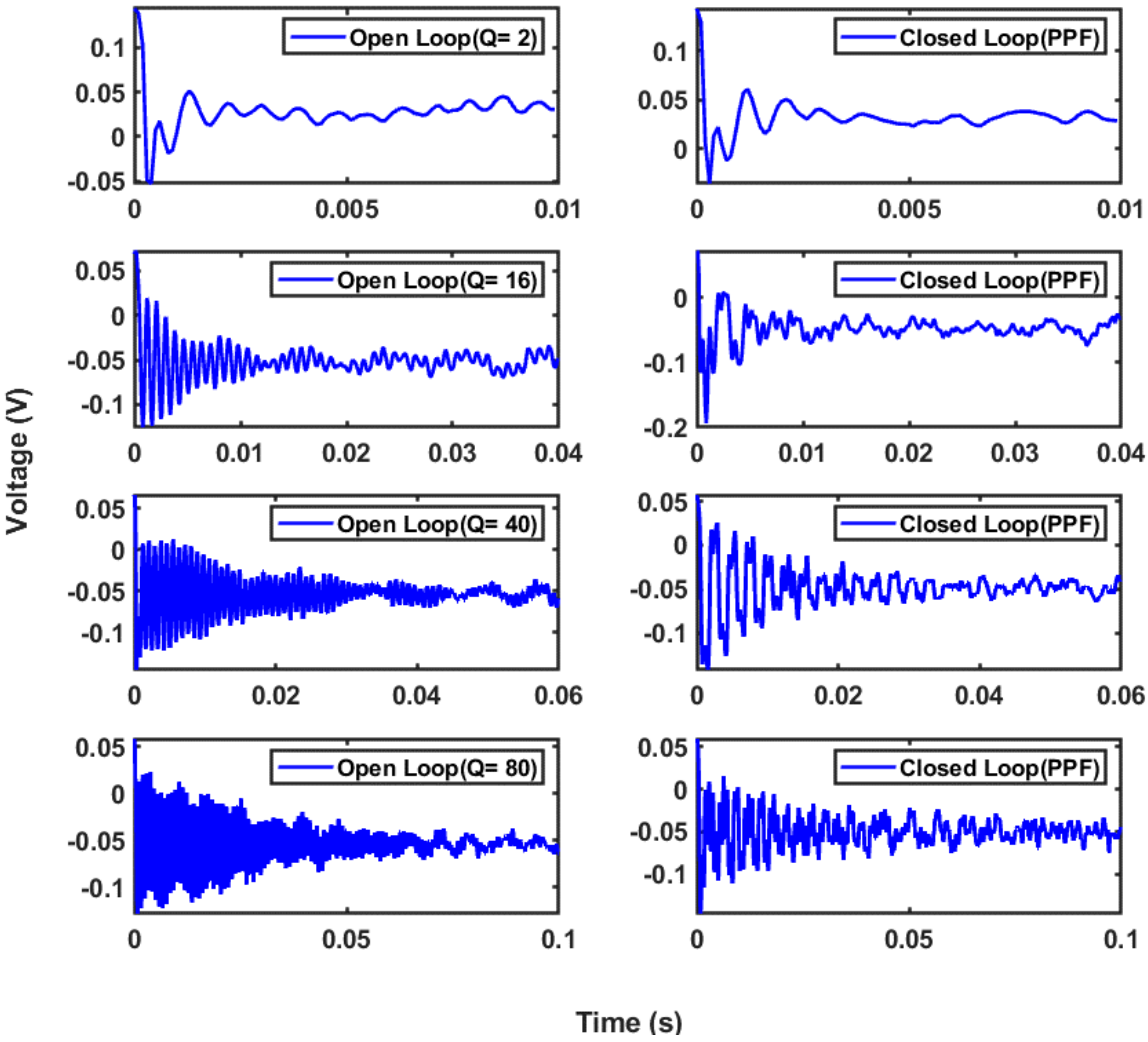

Figure 6.2 Step response of the open-loop system at different Q values(on the left) and closed loop system with PPF controller (on the right)

Following figure clearly shows that as the quality factor increases, the controller manages to reduce ringing and settling in the closed loop configuration. Table 6.1

encapsulates the reduction in quality factor when a PPF controller is used in a closed-loop operation. With the PPF controller, a 49% reduction in quality factor is measured in all the cases, as mentioned in Table 6.1.

Table 6.1 PPF controller performance evaluation at different Q

Open Loop		Closed Loop		% of Reduction
Q	Setting time, $T_s(ms)$	Q	Setting time, T_s (ms)	Q
2	1.6	1.8	1.5	10
16	13.3	10	6.2	54
40	33.5	17.2	14.2	57.5
80	66.7	40.6	33.83	49.3

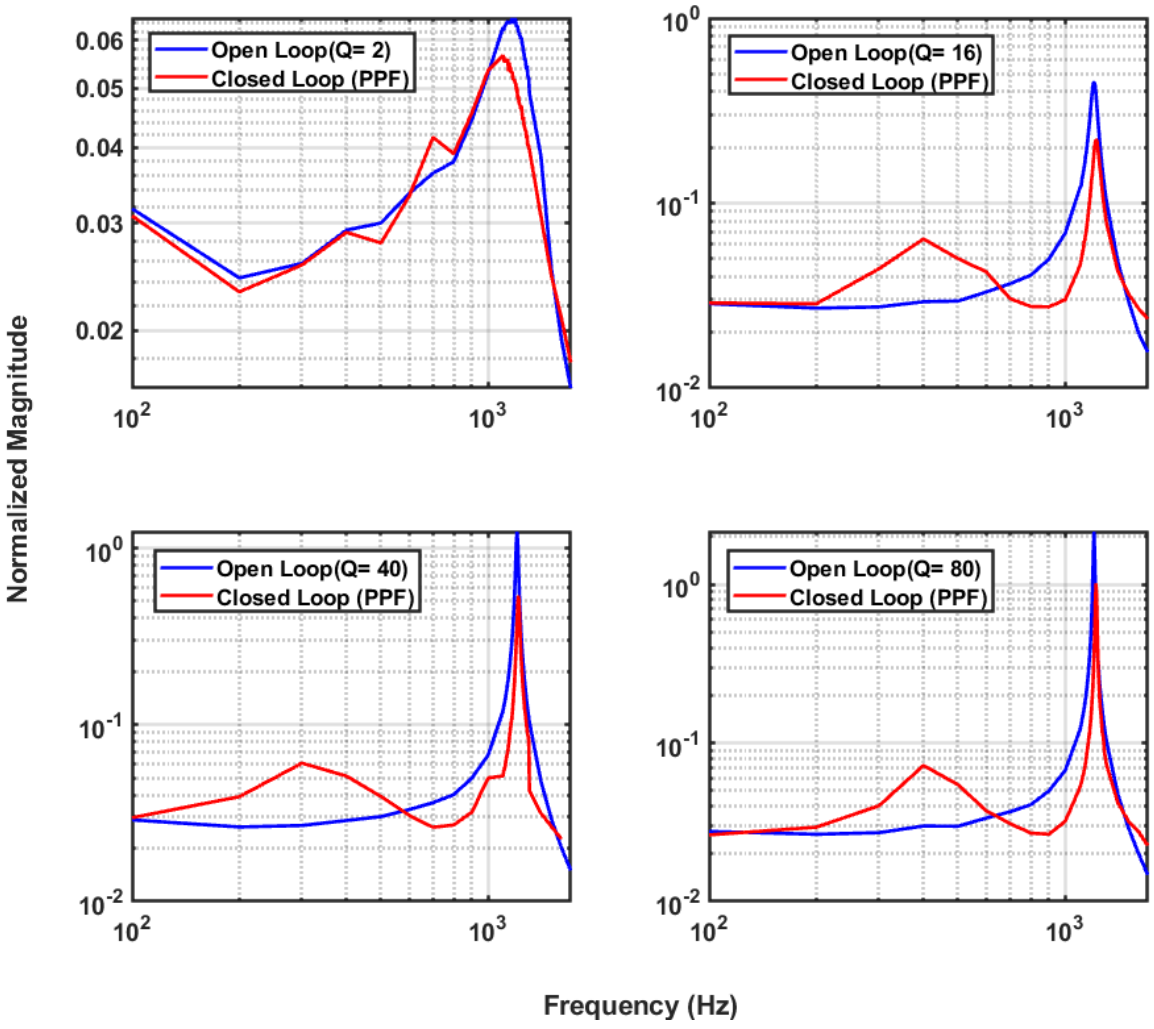

Figure 6.3 Frequency response of the open-loop vs closed loop system with PPF controller at different Q values

A similar conclusion can be drawn if the frequency response of the system is studied. Figure 6.3 depicts this 'frequency for different quality factors. The system's sensitivity increases at lower frequencies in a closed-loop, consistent with the simulation presented in Chapter 4. Furthermore, the reduction in the quality factor remains the same as for the AC response.

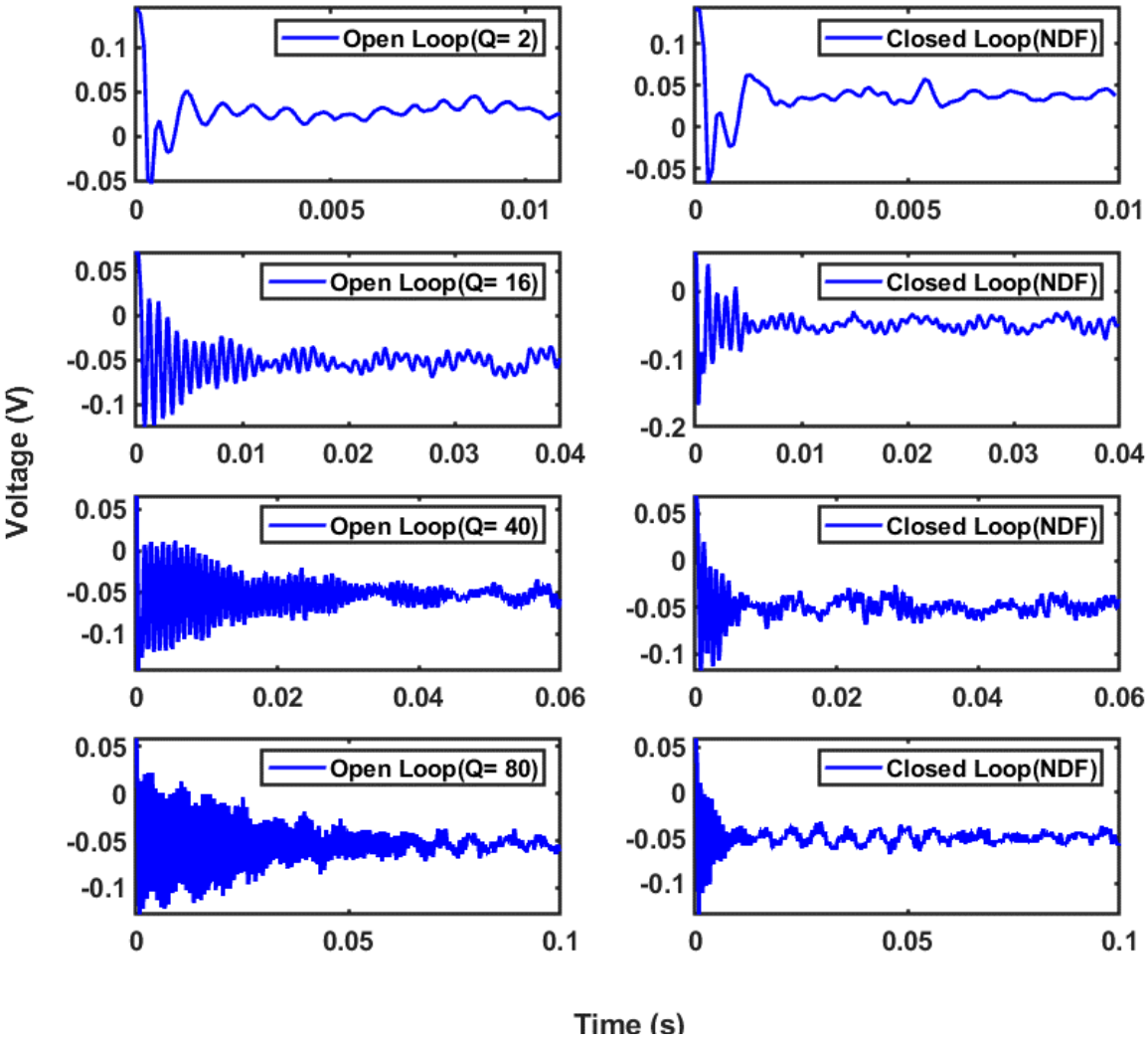

Figure 6.4 Step response of the open-loop system at different Q values(on the left) and closed loop system with NDF controller (on the right)

6.4. Negative Derivative Controller Performance:

Closed-loop testing with the negative derivative controller was carried out with the same input conditions and setup used for the PPF controller. As shown in Figure 6.4,

the system's step response was tested in both open and closed loops using the same amount of external acceleration. Figure 6.4 shows that the controller can handle an open-loop system leveraging high quality factor well. On average, an 85% reduction in the output oscillation and settling time was measured, as shown in Table 6.2. Another conclusion that can be drawn from the results is that in the case of a system with low quality factor (Q=2), as illustrated in Figure 6.4, the controller makes little effort, whereas, for a one with high quality factor (Q = 80), the controller adds extra gain to suppress the displacement of the system. Similar results can be noticed in the system frequency response shown in Figure 6.5.

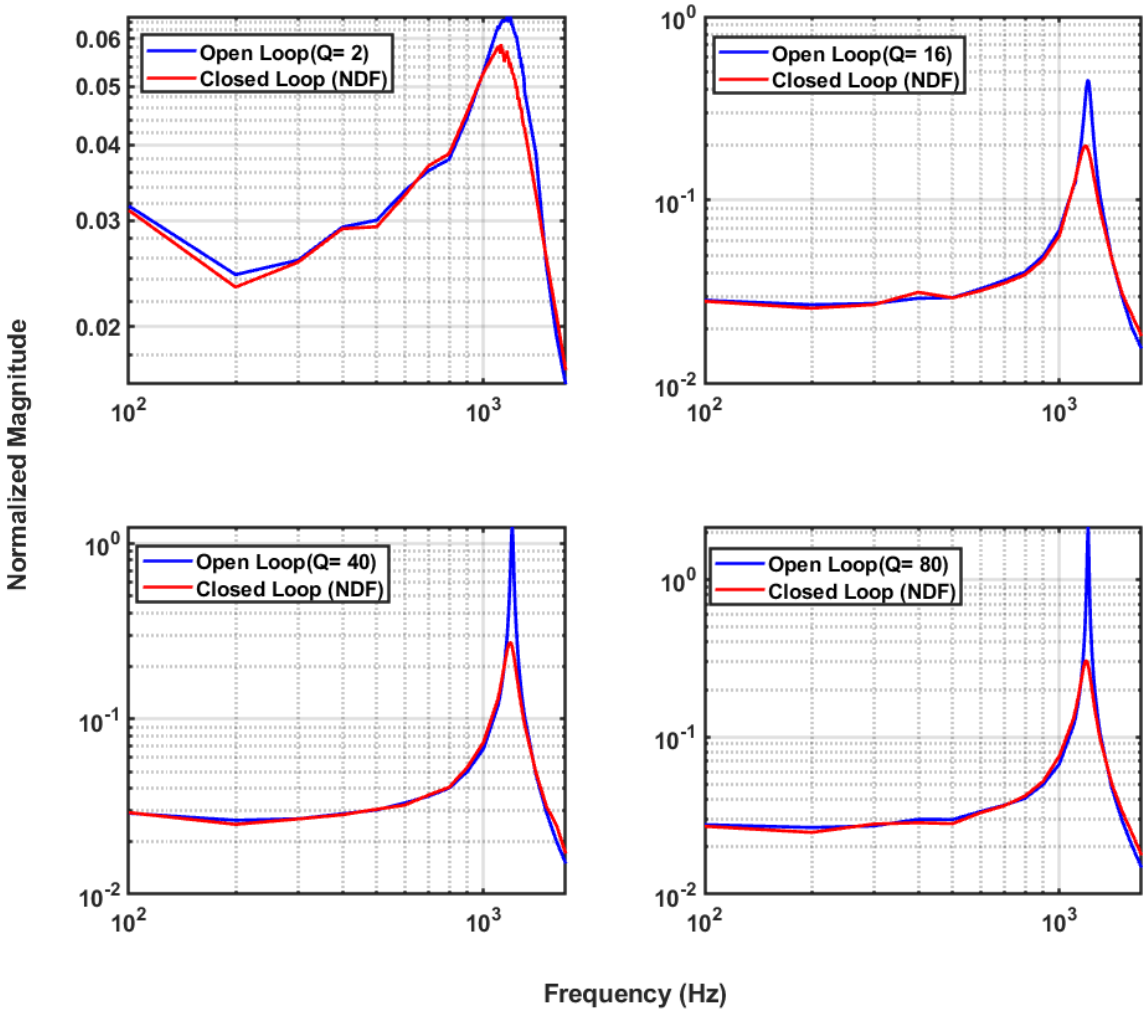

Figure 6.5 Frequency response of the open-loop vs closed loop system with NDF controller at different Q values

The results show that an open-loop system with a quality factor of 80 behaves similarly to a system having a quality factor of 20 in the closed loop because of the additional artificial electrostatic damping introduced. Another thing to note is the system's low-frequency response which remains the same as the open-loop response. This demonstrates an excellent agreement with the simulation results.

Table 6.2 NDF controller performance evaluation at different Q

Open Loop		Closed Loop		% Reduction
Q	Setting time, T_s (ms)	Q	Setting time, T_s (ms)	Q
2	1.6	1.85	1.54	7.5
16	13.3	6.5	5.3	59.3
40	33.5	9	7.5	77.5
80	66.7	11.5	9.58	85.6

6.5. Performance Comparison of The Proposed Controllers

It is clear from the preceding sections that both controllers work well in reducing the system's ringing, which means decreasing the displacement at resonance. However, comparing them would provide more insight into selecting the appropriate controller. Figure 6.6 compares the frequency response of the closed loop system with both controllers to the frequency response of the open-loop system with a Q of 120. It is evident that NDF reduces the system's quality factor by 85 percent without affecting its low-frequency response. In contrast, PPF reduces the quality factor by 50 percent while degrading the system's low-frequency response. A similar response is found for the time domain, as shown in Figure 6.7. The AC response results for both controllers are provided in Appendix A.

The preceding results demonstrate that when NDF is used, the system's ringing is drastically reduced, and the settling time is reduced by a factor of 12. Subsequently, it can be concluded that NDF outperforms PPF by meeting all the controller design objectives.

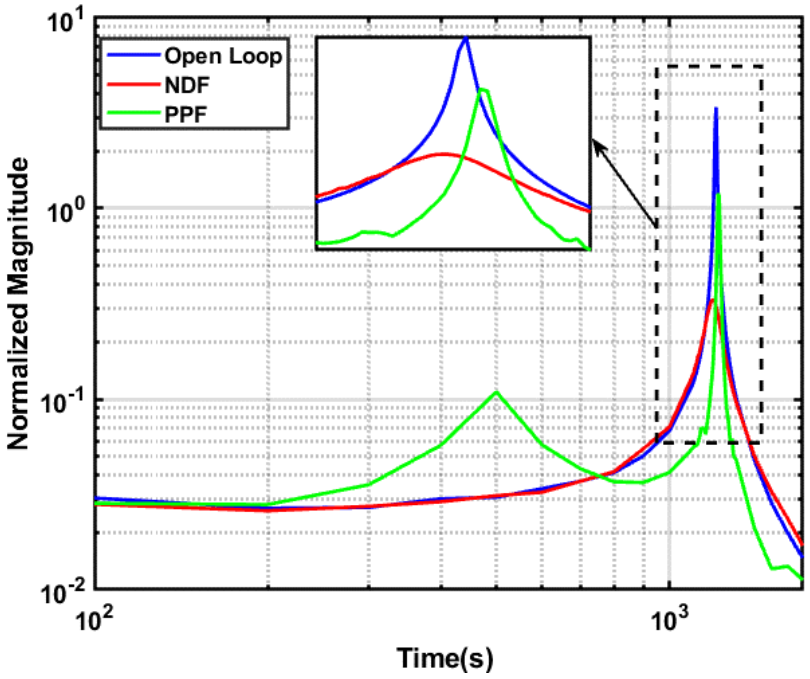

Figure 6.6 Frequency response of the open-loop vs closed loop system for both controllers at Q of 120

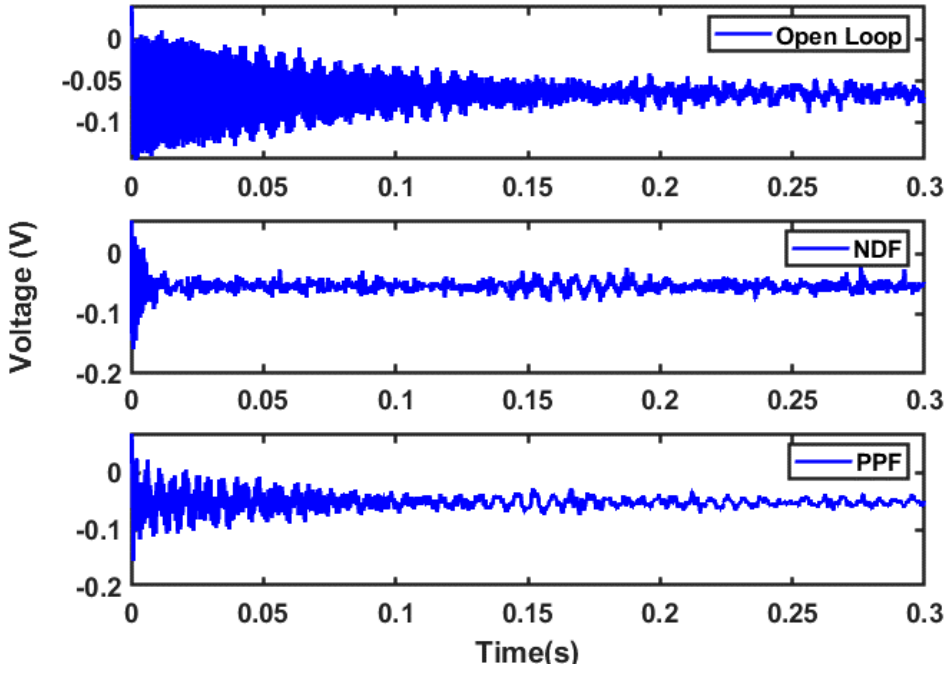

Figure 6.7 Step response of the open-loop and closed-loop system for both controllers at Q of 120

Chapter 7.
Conclusion and Future Works

This thesis presents a closed-loop control system designed for suppressing large displacement at the resonance of an accelerometer with high quality factor. The previous chapters demonstrate a detailed analysis of the design of the proposed algorithms, implementation, and test results. The findings of the research are summarised in this chapter.

7.1. Summary

Increasing market demand for high-performance accelerometers driving researchers to push the boundary of the current technology. Low g accelerometers are gaining popularity for detecting weak signals in military, space, seismology applications, etc. Researchers are developing low noise, highly sensitive accelerometers by increasing the proof mass thickness or decreasing the vacuum level inside the package. Among all the devices documented so far, the open-loop accelerometer presented in this thesis is one of the most sensitive ones because of its bulky mass and the large number of sensing electrodes present in the structure. As discussed in the earlier chapters, the large mass of the system contributes to a low noise floor of the system (around 150 $\mu g/\sqrt{Hz}$). This research attempts to lower the mechanical noise floor of the existing device even further by increasing the vacuum level inside the sensor package. However, a low damping level in the sensor package results in a large proof mass displacement at resonance. The overshoot may saturate proof mass movement or electronic gain circuitry. Thus, this thesis investigates a method of suppressing the displacement by implementing a closed-loop system.

Control methods for underdamped accelerometers investigated in the literature were based on linearizing the sensor response within its bandwidth region, operating the sensor beyond its pull in limit and designing low power consumption circuits. The reported accelerometers are low mass-based accelerometers as opposed

to the ISL accelerometer, which has larger proof mass, giving a significant advantage in terms of noise floor and sensitivity. However, this necessitates stronger actuators to stop the large proof mass in a closed loop, whereas the ISL accelerometer has weak actuators in place.

Thus, the control problem becomes more challenging because of the large actuator effort and highly underdamped sensor behaviour. Researchers attempted to implement artificial damping across all the frequencies in all investigated efforts, while this thesis focuses on damping around the chosen controller bandwidth. This work proposes a solution that uses a sensing electrode as an actuator around the resonance region. The rest of the time, the sensing electrode set works as a sensor. Furthermore, two resonant controllers, PPF and NDF, are identified as potential controllers based on the laid objectives. Both controllers have the property of exclusively providing gain to the system's natural frequency and can be used for dynamic feedback based on the deviation in the natural frequency of the system.

This work also describes an analytic model of the open-loop and closed-loop systems. The simulation results reveal that both controllers can suppress the system's resonance by lowering the overall Q of the system. After developing the controller and system architecture in simulation, the system is implemented in a microcontroller discussed in detail in the previous chapters. Experimental setup preparation and different experimental results are also discussed in detail. Designing the experimental setup for the closed-loop system to collect data was one of the complex tasks. This thesis can serve as a guideline and shortcoming of any high Q accelerometer closed-loop testing. The frequency response and time response data collected from the system accurately reflected the system's predicted performance from simulation. The controller works perfectly well even at very low-pressure levels (about 100 mTorr) and can suppress the system's proof mass displacement.

In conclusion, this thesis presented a novel controller for high Q-based accelerometers that considerably reduces the displacement in resonance and saves it from failure. Furthermore, NDF outperforms PPF for suppressing the displacement

while maintaining the same open-loop response for low frequencies. All claims made were verified through simulation and backed up with experiments.

7.2. Thesis Contribution

The highlights of the thesis contribution can be summarised as follows:

Designing a closed system for a High Q Accelerometer

This work presented two resonant controllers for designing a closed-loop system that effectively suppresses the system's resonance. Furthermore, the proposed controller allows adjusting bandwidth in response to the system's parameter variation.

Proposed a system architecture for effective use of Actuator

This thesis presents an alternative use of the sensing electrodes to compensate for the system's weak actuator. This method of using the sensor electrode as an actuator has never been realized before in the literature.

Implementation and Experimental Verification

The proposed control algorithms are implemented using a microcontroller for testing their effectiveness. The accelerometer prototypes are tested in open-and closed-loop conditions under vacuum. The testing setup was redesigned to test the sensor in a closed loop under vacuum conditions.

7.3. Future Work

Despite the extensive work on developing methods for suppressing the resonance of high Q accelerometers, there are a variety of other challenges and improvements that could be investigated and handled in the future.

MEMS-based Accelerometers are linear parameters varying systems. Environmental factors and structural fatigue alter the sensor's characteristic

parameters over time, changing the resonance frequency and quality factor. Thus, the controller can be made adaptive, allowing it to fine-tune the controller coefficient and update it in response to parameter changes in real-time. Moreover, the sensing element of the sensor is nonlinear for large acceleration. Therefore, a nonlinear controller can be developed to incorporate all the system's nonlinearities, which might increase the system's effectiveness.

A more powerful actuator system can be developed to handle the large-proof mass-based system to reduce the actuator effort. For example, a thermal actuator, rather than a capacitive based actuator, might be able to solve the problem.

Other researchers investigated a possibility of a micro mechanical low pass filter to deal with vibration suppression problems in various MEMS devices. Similar approach can be taken to incorporate a mechanical low pass filter in conjunction with a sensor structure as discussed in the **Appendix B**. This might require a new design of the ISL accelerometer.

.

References

[1] V. Narasimhan, H. Li, and M. Jianmin, "Micromachined high-g accelerometers: a review," *J. Micromechanics Microengineering*, vol. 25, no. 3, p. 033001, Mar. 2015, doi: 10.1088/0960-1317/25/3/033001.

[2] Y. Bai *et al.*, "Research and Development of Electrostatic Accelerometers for Space Science Missions at HUST," *Sensors*, vol. 17, no. 9, p. 1943, Aug. 2017, doi: 10.3390/s17091943.

[3] J. Beaussier, A.-M. Mainguy, A. Olivero, and R. Rolland, "In orbit performance of the Cactus accelerometer (D5B spacecraft)," *Acta Astronaut.*, vol. 4, no. 9–10, pp. 1085–1102, Sep. 1977, doi: 10.1016/0094-5765(77)90008-X.

[4] C. Wang *et al.*, "Micromachined Accelerometers with Sub-μg/√Hz Noise Floor: A Review," *Sensors*, vol. 20, no. 14, p. 4054, Jul. 2020, doi: 10.3390/s20144054.

[5] N. Yazdi, F. Ayazi, and K. Najafi, "Micromachined Inertial Sensors," *Proc. IEEE*, vol. 86, no. 8, p. 20, 1998.

[6] B. Bahreyni, *Fabrication and design of resonant microdevices*. Norwich, NY: W. Andrew Inc, 2008.

[7] S. Beeby, Ed., *MEMS mechanical sensors*. Boston: Artech House, 2004.

[8] Y. TerziOğlu, "A high Performance Closed Loop Analouge Readout circuit for capacitive MEMS Accelerometer," MASc dissertation, 2015, Available : https://open.metu.edu.tr/handle/11511/24886, METU

[9] P. J. French and P. M. Sarro, "Surface versus bulk micromachining: the contest for suitable applications," p. 10.

[10] C. Lu, M. Lemkin, and B. E. Boser, "A monolithic surface micromachined accelerometer with digital output," *IEEE J. Solid-State Circuits*, vol. 30, no. 12, pp. 1367–1373, Dec. 1995, doi: 10.1109/4.482163.

[11] P. Zwahlen *et al.*, "Open-loop and closed-loop high-end accelerometer platforms for high demanding applications," in *2016 IEEE/ION Position, Location and Navigation Symposium (PLANS)*, Savannah, GA, Apr. 2016, pp. 932–937. doi: 10.1109/PLANS.2016.7479790.

[12] B. Borovic, A. Q. Liu, D. Popa, H. Cai, and F. L. Lewis, "Open-loop versus closed-loop control of MEMS devices: choices and issues," *J. Micromechanics Microengineering*, vol. 15, no. 10, pp. 1917–1924, Oct. 2005, doi: 10.1088/0960-1317/15/10/018.

[13] R. A. Holler, "The evolution of the sonobuoy from World War II to the cold war.pdf," 2014, [Online]. Available: https://apps.dtic.mil/sti/citations/ADA597432

[14] F. Edalatfar, “Design and Fabrication of High-Performance Capacitive Micro Accelerometers,” Ph.D. dissertation, 2017, Available: https://summit.sfu.ca/item/18084, Simon Fraser University.

[15] F. Mohd-Yasin, D. J. Nagel, and C. E. Korman, “Noise in MEMS,” *Meas. Sci. Technol.*, vol. 21, no. 1, p. 012001, Nov. 2009, doi: 10.1088/0957-0233/21/1/012001.

[16] A. Sinding *et al.*, “A novel squeezed-film damping model for MEMS comb structures,” in *2017 19th International Conference on Solid-State Sensors, Actuators and Microsystems (TRANSDUCERS)*, Kaohsiung, Jun. 2017, pp. 2095–2098. doi: 10.1109/TRANSDUCERS.2017.7994487.

[17] T. B. Gabrielson, “Mechanical-thermal noise in micromachined acoustic and vibration sensors,” *IEEE Trans. Electron Devices*, vol. 40, no. 5, pp. 903–909, May 1993, doi: 10.1109/16.210197.

[18] D. J. Bell, T. J. Lu, N. A. Fleck, and S. M. Spearing, “MEMS actuators and sensors: observations on their performance and selection for purpose,” *J. Micromechanics Microengineering*, vol. 15, no. 7, pp. S153–S164, Jul. 2005, doi: 10.1088/0960-1317/15/7/022.

[19] J. I. Seeger and B. E. Boser, “Charge control of parallel-plate, electrostatic actuators and the tip-in instability,” *J. Microelectromechanical Syst.*, vol. 12, no. 5, pp. 656–671, Oct. 2003, doi: 10.1109/JMEMS.2003.818455.

[20] S. Pamidighantam, R. Puers, K. Baert, and H. A. C. Tilmans, “Pull-in voltage analysis of electrostatically actuated beam structures with fixed–fixed and fixed–free end conditions,” p. 8.

[21] E. Saucedo-Flores, R. Ruelas, M. Flores, and J. Chiao, “Study of the Pull-In Voltage for MEMS Parallel Plate Capacitor Actuators,” *MRS Proc.*, vol. 782, p. A5.86, 2003, doi: 10.1557/PROC-782-A5.86.

[22] V. P. Petkov and B. E. Boser, “High-order electromechanical Sigma Delta modulation in micromachined inertial sensors,” *IEEE Trans. Circuits Syst. Regul. Pap.*, vol. 53, no. 5, pp. 1016–1022, May 2006, doi: 10.1109/TCSI.2006.869901.

[23] W. Henrion, L. DiSanza, M. Ip, S. Terry, and H. Jerman, “Wide dynamic range direct accelerometer,” in *IEEE 4th Technical Digest on Solid-State Sensor and Actuator Workshop*, Hilton Head Island, SC, USA, 1990, pp. 153–157. doi: 10.1109/SOLSEN.1990.109842.

[24] H. Kulah, J. Chae, N. Yazdi, and K. Najafi, “Noise Analysis and Characterization of a Sigma-Delta Capacitive Microaccelerometer,” *IEEE J. Solid-State Circuits*, vol. 41, no. 2, pp. 352–361, Feb. 2006, doi: 10.1109/JSSC.2005.863148.

[25] T. Smith, O. Nys, M. Chevroulet, Y. DeCoulon, and M. Degrauwe, “A 15 b electromechanical sigma-delta converter for acceleration measurements,” in *Proceedings of IEEE International Solid-State Circuits Conference - ISSCC ’94*, San Francisco, CA, USA, 1994, pp. 160–161. doi: 10.1109/ISSCC.1994.344687.

[26] F. Chen, W. Yuan, H. Chang, I. Zeimpekis, and M. Kraft, “Low noise vacuum MEMS closed-loop accelerometer using sixth-order multi-feedback loops and local resonator sigma delta modulator,” in *2014 IEEE 27th International Conference on Micro Electro Mechanical Systems (MEMS)*, San Francisco, CA, USA, Jan. 2014, pp. 761–764. doi: 10.1109/MEMSYS.2014.6765752.

[27] Y. Dong, P. Zwahlen, A.-M. Nguyen, F. Rudolf, and J.-M. Stauffer, “High performance inertial navigation grade sigma-delta MEMS accelerometer,” in *IEEE/ION Position, Location and Navigation Symposium*, Indian Wells, CA, USA, May 2010, pp. 32–36. doi: 10.1109/PLANS.2010.5507135.

[28] B. Almutairi and M. Kraft, “Multi stage noise shaping sigma–delta modulator (MASH) for capacitive MEMS accelerometers,” *Sens. Actuators Phys.*, vol. 186, pp. 169–177, Oct. 2012, doi: 10.1016/j.sna.2012.05.010.

[29] Jiangfeng Wu and L. R. Carley, “Electromechanical Sigma Delta modulation with high-Q micromechanical accelerometers and pulse density modulated force feedback,” *IEEE Trans. Circuits Syst. Regul. Pap.*, vol. 53, no. 2, pp. 274–287, Feb. 2006, doi: 10.1109/TCSI.2005.857084.

[30] H. Xu, X. Liu, and L. Yin, “A Closed-Loop $\Sigma\Delta $ Interface for a High-Q Micromechanical Capacitive Accelerometer With 200 ng/$\surd $ Hz Input Noise Density.,” *IEEE J. Solid-State Circuits*, vol. 50, no. 9, pp. 2101–2112, Sep. 2015, doi: 10.1109/JSSC.2015.2428278.

[31] D. Chen *et al.*, “A Straightforward Approach for Synthesizing Electromechanical Sigma-Delta MEMS Accelerometers,” *Sensors*, vol. 20, no. 1, p. 91, Dec. 2019, doi: 10.3390/s20010091.

[32] F. Chen, X. Li, and M. Kraft, “Electromechanical Sigma–Delta Modulators ($\Sigma \Delta {\mathrm{ M}}$) Force Feedback Interfaces for Capacitive MEMS Inertial Sensors: A Review,” *IEEE Sens. J.*, vol. 16, no. 17, pp. 6476–6495, Sep. 2016, doi: 10.1109/JSEN.2016.2582198.

[33] K. H.-L. Chau, S. R. Lewis, Y. Zhao, R. T. Howe, S. F. Bart, and R. G. Marcheselli, “An Integrated Force-balanced Capacitive Accelerometer For Low-G Applications,” in *Proceedings of the International Solid-State Sensors and Actuators Conference - TRANSDUCERS ’95*, Stockholm, Sweden, 1995, vol. 1, pp. 593–596. doi: 10.1109/SENSOR.1995.717294.

[34] E. H. Sarrraf, “Design, Modelling, Self-Testing and Self-Calibration of MEMS Accelerometers with Adaptive and Non-Linear Digital Control,” Ph.D. dissertation, 2013. [Online]. Available: https://oatao.univ-toulouse.fr/17939/

[35] L. Aaltonen, P. Rahikkala, M. Saukoski, and K. Halonen, “High-resolution continuous-time interface for micromachined capacitive accelerometer,” *Int. J. Circuit Theory Appl.*, vol. 37, no. 2, pp. 333–349, Mar. 2009, doi: 10.1002/cta.547.

[36] M. Yucetas, A. Kalanti, J. Salomaa, L. Aaltonen, and K. Halonen, “An analog closed-loop SC accelerometer interface for a capacitive high-Q sensor element,” p. 4, 2010.

[37] M. Yucetas, L. Aaltonen, M. Pulkkinen, J. Salomaa, A. Kalanti, and K. Halonen, “A charge balancing accelerometer interface with electrostatic damping,” in *2011 Proceedings of the ESSCIRC (ESSCIRC)*, Helsinki, Finland, Sep. 2011, pp. 291–294. doi: 10.1109/ESSCIRC.2011.6044964.

[38] M. Lemkin and B. E. Boser, “A three-axis micromachined accelerometer with a CMOS position-sense interface and digital offset-trim electronics,” *IEEE J. Solid-State Circuits*, vol. 34, no. 4, pp. 456–468, Apr. 1999, doi: 10.1109/4.753678.

[39] B. Vakili Amini, R. Abdolvand, and F. Ayazi, “A 4.5-mW Closed-Loop $\Delta\Sigma$ Micro-Gravity CMOS SOI Accelerometer,” *IEEE J. Solid-State Circuits*, vol. 41, no. 12, pp. 2983–2991, Dec. 2006, doi: 10.1109/JSSC.2006.884864.

[40] Y. Dong, M. Kraft, C. Gollasch, and W. Redman-White, “A high-performance accelerometer with a fifth-order sigma–delta modulator,” *J. Micromechanics Microengineering*, vol. 15, no. 7, pp. S22–S29, Jul. 2005, doi: 10.1088/0960-1317/15/7/004.

[41] B. Almutauri, “Multi Stage Noise Shaping (MASH) Sigma Delta Modulator for Capacitive MEMS Inertial Sesnors,” Ph.D. dissertation, 2015.

[42] E. H. Sarraf, B. Cousins, E. Cretu, and S. Mirabbasi, “Design and implementation of a novel sliding mode sensing architecture for capacitive MEMS accelerometers,” *J. Micromechanics Microengineering*, vol. 21, no. 11, p. 115033, Nov. 2011, doi: 10.1088/0960-1317/21/11/115033.

[43] M. Yücetaş, “Capacitive Accelerometer interfaces utilising high Q MEMS sensor elements.pdf,” Ph.D. dissertation, Aalto University, 2013.

[44] T. Köse, Y. Terzioğlu, K. Azgın, and T. Akın, “A single mass two-axis capacitive MEMS accelerometer with force rebalance,” in *2015 IEEE International Symposium on Inertial Sensors and Systems (ISISS) Proceedings*, Hapuna Beach, HI, USA, Mar. 2015, pp. 1–4. doi: 10.1109/ISISS.2015.7102371.

[45] C. Lavinia, “System design of low power accelermeter with electrostatic damping control.pdf,” Ph.D. dissertation, INP Toulouse, 2017.

[46] B. A. Francis and W. M. Wonham, “The internal model principle of control theory,” *Automatica*, vol. 12, no. 5, pp. 457–465, Sep. 1976, doi: 10.1016/0005-1098(76)90006-6.

[47] I. Alsogkier and C. Bohn, “Rejection and Compensation of Periodic Disturbance in Control Systems,” p. 11.

[48] H. H. Syed, “Comparative study between positive position feedback and negative derivative feedback for vibration control of a flexible arm featuring

piezoelectric actuator," *Int. J. Adv. Robot. Syst.*, vol. 14, no. 4, p. 172988141771880, Jul. 2017, doi: 10.1177/1729881417718801.

[49] K. H. FloreÃ, "Single and Multiple Positive Position Feedback Control of a Magnetorheological Automotive Suspension," p. 6, 2019.

[50] W. Jung, I. Noh, and D. Kang, "The vibration controller design using positive position feedback control," in *2013 13th International Conference on Control, Automation and Systems (ICCAS 2013)*, Gwangju, Korea (South), Oct. 2013, pp. 1721–1724. doi: 10.1109/ICCAS.2013.6704213.

[51] Q. Mao and S. Pietrzko, *Control of Noise and Structural Vibration*. London: Springer London, 2013. doi: 10.1007/978-1-4471-5091-6.

[52] F. Cola, F. Resta, and F. Ripamonti, "A negative derivative feedback design algorithm," *Smart Mater. Struct.*, vol. 23, no. 8, p. 085008, Aug. 2014, doi: 10.1088/0964-1726/23/8/085008.

[53] G. Cazzulani, F. Resta, F. Ripamonti, and R. Zanzi, "Negative derivative feedback for vibration control of flexible structures," *Smart Mater. Struct.*, vol. 21, no. 7, p. 075024, Jul. 2012, doi: 10.1088/0964-1726/21/7/075024.

[54] N. Debattisti, M. L. Bacci, and S. Cinquemani, "A selective negative derivative feedback algorithm to improve stability for inertial actuators," in *Active and Passive Smart Structures and Integrated Systems IX*, Online Only, United States, Apr. 2020, p. 102. doi: 10.1117/12.2558540.

[55] H. J. Yu *et al.*, "The Research on MEMS Micro Capacitance Sensor Detection Based on MS3110," *Key Eng. Mater.*, vol. 645–646, pp. 528–532, May 2015, doi: 10.4028/www.scientific.net/KEM.645-646.528.

[56] K. Riaz, M. U. Mian, and S. A. Bazaz, "Fabrication Imperfection Analysis of Robust Decoupled 3-DoF Non-Resonant MEMS Gyroscope," vol. 4, no. 8, p. 9, 2013.

[57] X. Dong, S. Yang, J. Zhu, Y. En, and Q. Huang, "Method of Measuring the Mismatch of Parasitic Capacitance in MEMS Accelerometer Based on Regulating Electrostatic Stiffness," *Micromachines*, vol. 9, no. 3, p. 128, Mar. 2018, doi: 10.3390/mi9030128.

[58] F. Edalafar *et al.*, "A Wideband, Low-Noise Accelerometer for Sonar Wave Detection," *IEEE Sens. J.*, vol. 18, no. 2, pp. 508–516, Jan. 2018, doi: 10.1109/JSEN.2017.2774705.

[59] A. Albarbar, A. Badri, J. K. Sinha, and A. Starr, "Performance evaluation of MEMS accelerometers," *Measurement*, vol. 42, no. 5, pp. 790–795, Jun. 2009, doi: 10.1016/j.measurement.2008.12.002.

[60] D. R. Sparks, S. Massoud-Ansari, and N. Najafi, "Chip-level vacuum packaging of micromachines using nanogetters," *IEEE Trans. Adv. Packag.*, vol. 26, no. 3, pp. 277–282, Aug. 2003, doi: 10.1109/TADVP.2003.817964.

[61] T. Tanabe, H. Yano, and H. Iwata, “Properties of proprioceptive sensation with a vibration speaker-type non-grounded haptic interface,” in *2016 IEEE Haptics Symposium (HAPTICS)*, Philadelphia, PA, USA, Apr. 2016, pp. 21–26. doi: 10.1109/HAPTICS.2016.7463150.

[62] B. Bottenfield, A. G. Bond, M. S. Kranz, R. N. Dean, and M. L. Adams, “Variations in Micromachined Isolator Geometries for Sensor Performance in Harsh Environments,” *IEEE Trans. Compon. Packag. Manuf. Technol.*, vol. 10, no. 4, pp. 659–668, Apr. 2020, doi: 10.1109/TCPMT.2019.2947191.

[63] K.-L. Chen and Y.-J. Lai, "Mechanical Low Pass Filter for Motion Sensors", "2017", "https://www.freepatentsonline.com/y2017/0089943.html".

Appendix A AC Response of the System

To assess the controller's performance, the AC response of the ISL accelerometer in a closed-loop configuration is collected for various frequencies of the applied acceleration signal.

A 200 Hz sinusoidal acceleration is applied to the system. Figure A.1 compares the time response of open loop and closed loop with the NDF controller. The system shows an identical open-loop and closed-loop responses, indicating that the controller doesn't exert any force at low frequencies.

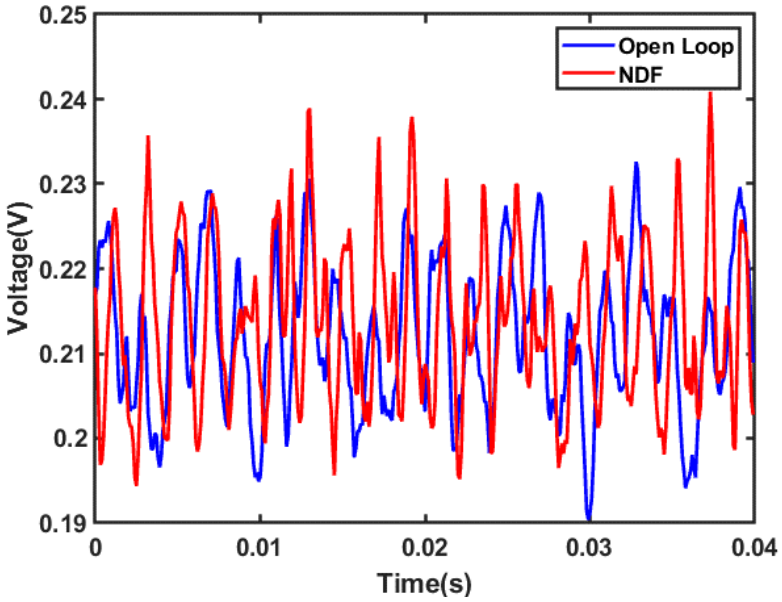

Figure A.1 AC response at 85 mTorr for 200 Hz excitation signal

On the contrary, with the PPF controller in the closed loop, for the same excitation signal an interference is observed.

When the system is excited at resonance, NDF controller shows a good reduction of the open loop signal as shown in Figure A.3 as compared to PPF controller, shown in the Figure A.4

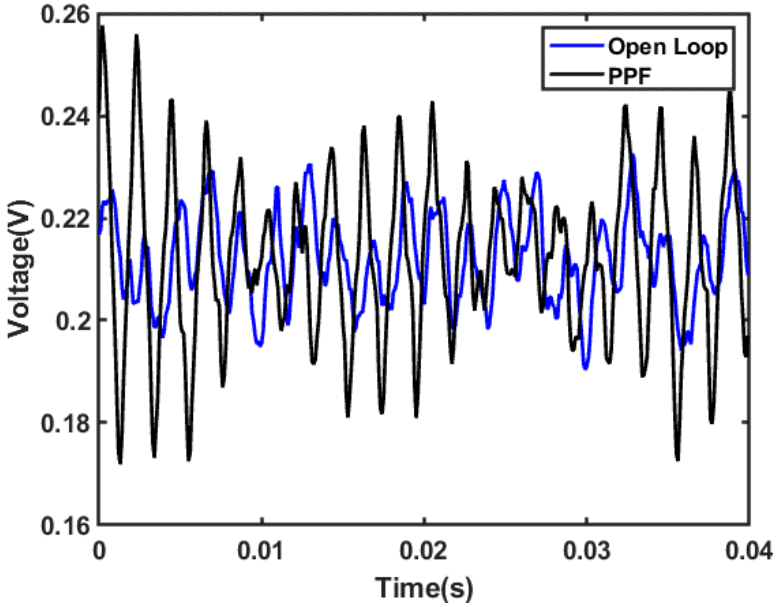

Figure A.2 AC response at 85mTor for 200 Hz exicitation signal

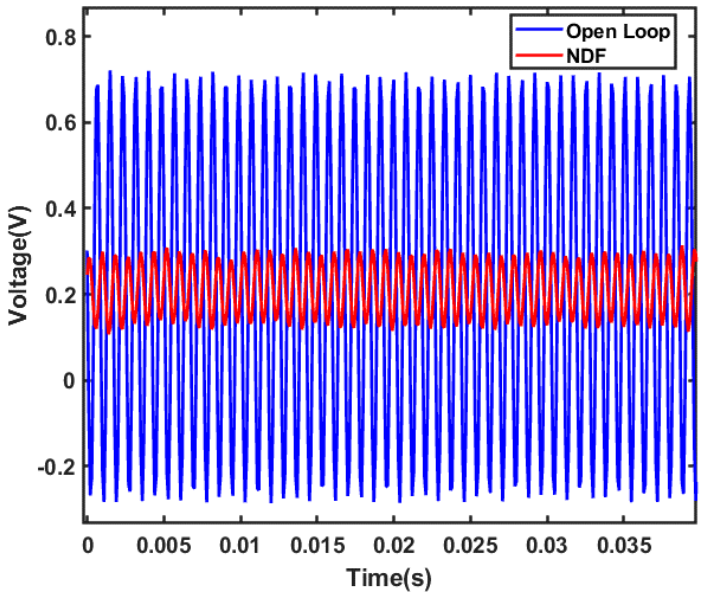

Figure A.3 AC response at 85 mTor for 1200 Hz exicitation signal

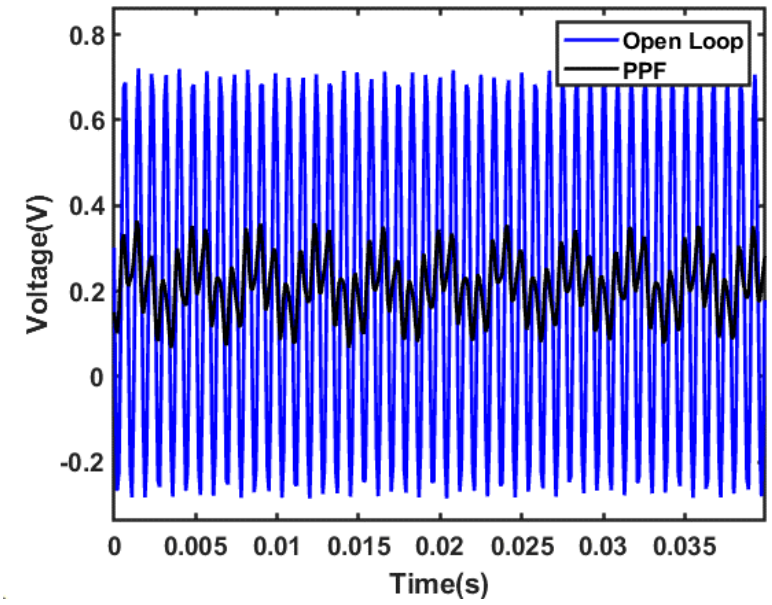

Figure A.4 AC response at 85 mTor for 1200 Hz exicitation signal

Appendix B Passive Vibration Suppression Methods

Vibration suppression is a common concept in various macro structures. However, the idea is relatively new in the micro devices and a researcher will encounter with lots of challenges while dealing with the problem in the micro world. In this thesis, we have discussed an active way of supressing the resonance by adding electrostatic damping to the structure. However, throughout the journey, we have come up with many other ideas, the most notable of which are nonlinear energy sink, mechanical low pass filter design, and replacing electrostatic actuators with thermal actuator. One of the top ideas for passively suppressing resonance was implementation of mechanical low pass filter either inside of the substrate or outside of the package.

The concept of mechanical low pass filter is based on vibration isolation. It is relatively new concept and difficult to implement in microsystems. The main idea is to dampen the structure's resonance by placing a filter's cut-off before the resonance frequency of the structure. For example, a 2^{nd} order filter will have a -40 dB/decade roll off rate after it's cut off. Placing the filter along with mechanical structure in series would generate combined nullifying effect in the structure Thus, a vibration suppression effect on mechanical structure can be obtained as shown in the Figure B.1.

A mechanical filter can be implemented in the system either with the microstructure or can be placed outside of the sensor package. Researchers devised various methods for incorporating a mechanical filter into the system for various purposes. Figure B.2 shows a proposal in which a structure formed outside of the sensor package provides a roll off rate of -40dB/decade after its cut-off frequency [62]. Similarly, Apple Inc. owns a patent on a mechanical low pass filter used in motion sensors where the filter is placed inside the structure [63].

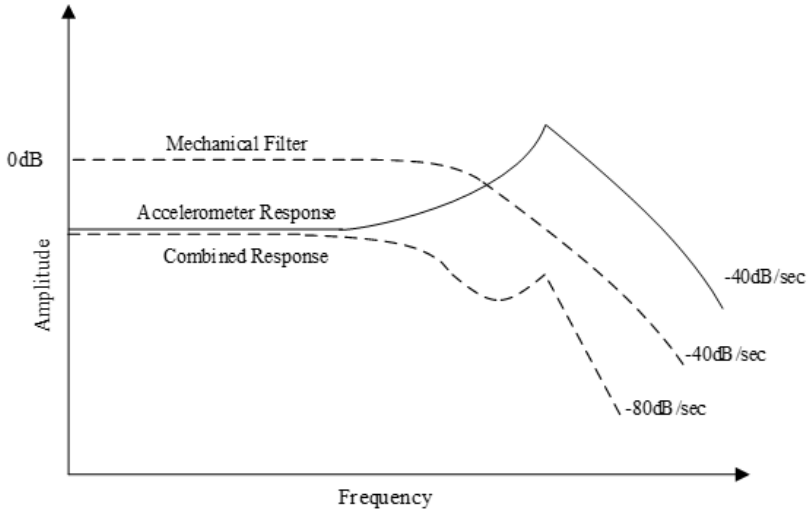

Figure B.1 Frequency response of the mechanical low pass filter and combined system.

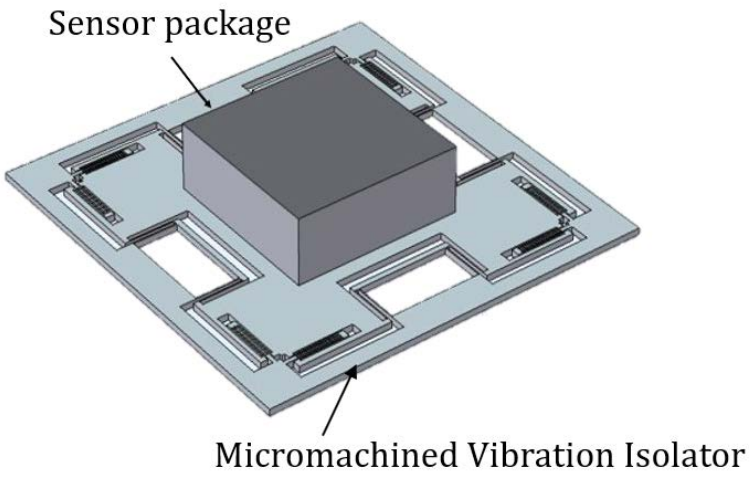

Figure B.2 Vbiration islator design for vibration supression in the sensor

Figure B.3 The proposed mechanical low pass filter for

In this work, we planned to integrate a material layer as a 2nd order mechanical low pass filter beneath device. Figure B.3 shows the arrangement for it. The research question now is to find such a material that provides sufficient damping effect after it's cut off frequency. Placing a simple material layer beneath the surface addresses the complexity of designing a microstructure alongside the device.

To begin, the initial modeling was done using the lumped parameter method, and from there, with some approximation, spring constant, damping of the material and material mass required was estimated. Following a material search, PDMS was chosen, despite the fact that its damping value is inadequate. FEM simulation also revealed the need for more damping in the material. Thus, PDMS implementation must be revised and reinvestigated, most likely to obtain different material that can do the job.

In conclusion, the investigation into the implementation of the material layer is still in its early stages. There are issues that must be addressed while investigating this aspect of the research. It is essential to explore methods of increasing the damping values of the material as well as a method of incorporating it into the PCB board. This research showed an idea of passively suppressing the resonance in the MEMS acceleration sensors.